UNIVERSIDADE ESTADUAL DE CAMPINAS
FACULDADE DE ENGENHARIA MECÂNICA

Arthur Guilherme Mereles

Prediction of fluid-induced instabilities in rotors on hydrodynamic bearings using center manifold reduction

Predição de instabilidades fluido-induzidas em rotores com mancais hidrodinâmicos usando redução pela variedade central

Campinas

2024

Arthur Guilherme Mereles

Prediction of fluid-induced instabilities in rotors on hydrodynamic bearings using center manifold reduction

Predição de instabilidades fluido-induzidas em rotores com mancais hidrodinâmicos usando redução pela variedade central

Thesis presented to the School of Mechanical Engineering of the University of Campinas in partial fulfillment of the requirements for the degree of Doctor in Mechanical Engineering, in the area of Solid Mechanics and Mechanical Design.

Tese apresentada à Faculdade de Engenharia Mecânica da Universidade Estadual de Campinas como parte dos requisitos exigidos para obtenção do título de Doutor em Engenharia Mecânica, na Área de Mecânica dos Sólidos e Projeto Mecânico.

Orientadora: Profa. Dra. Katia Lucchesi Cavalca Dedini.
Co-orientador: Prof. Dr. Diogo Stuani Alves.

ESTE TRABALHO CORRESPONDE À VERSÃO FINAL DA TESE DEFENDIDA PELO ALUNO ARTHUR GUILHERME MERELES, E ORIENTADA PELA PROFA. DRA. KATIA LUCCHESI CAVALCA DEDINI.

Campinas

2024

Ficha catalográfica
Universidade Estadual de Campinas (UNICAMP)
Biblioteca da Área de Engenharia e Arquitetura
Rose Meire da Silva - CRB 8/5974

M541p

Mereles, Arthur Guilherme, 1997-
Prediction of fluid-induced instabilities in rotors on hydrodynamic bearings using center manifold reduction / Arthur Guilherme Mereles. – Campinas, SP : [s.n.], 2024.

Orientador: Katia Lucchesi Cavalca Dedini.
Coorientador: Diogo Stuani Alves.
Tese (doutorado) – Universidade Estadual de Campinas (UNICAMP), Faculdade de Engenharia Mecânica.

1. Dinâmica de rotores. 2. Mancais. 3. Bifurcação de Hopf. 4. Fluidodinâmica computacional. I. Dedini, Katia Lucchesi Cavalca, 1963-. II. Alves, Diogo Stuani, 1986-. III. Universidade Estadual de Campinas (UNICAMP). Faculdade de Engenharia Mecânica. IV. Título.

Informações Complementares

Título em outro idioma: Predição de instabilidades fluido-induzidas em rotores com mancais hidrodinâmicos usando redução pela variedade central
Palavras-chave em inglês:
Rotordynamics
Bearings
Hopf bifurcation
Computational fluid dynamics
Área de concentração: Mecânica dos Sólidos e Projeto Mecânico
Titulação: Doutor em Engenharia Mecânica
Banca examinadora:
Katia Lucchesi Cavalca Dedini [Orientador]
Ilmar Ferreira Santos
Hans Ingo Weber
Carlos Alberto Bavastri
Athanasios Chasalevris
Data de defesa: 12-07-2024
Programa de Pós-Graduação: Engenharia Mecânica

Identificação e informações acadêmicas do(a) aluno(a)
- ORCID do autor: https://orcid.org/0000-0002-1921-7934
- Currículo Lattes do autor: https://lattes.cnpq.br/7275080884849491

UNIVERSIDADE ESTADUAL DE CAMPINAS
FACULDADE DE ENGENHARIA MECÂNICA

TESE DE DOUTORADO ACADÊMICO

Prediction of fluid-induced instabilities in rotors on hydrodynamic bearings using center manifold reduction

Predição de instabilidades fluido-induzidas em rotores com mancais hidrodinâmicos usando redução pela variedade central

Autor: Arthur Guilherme Mereles

Orientador: Profa. Dra. Katia Lucchesi Kavalca Dedini
Co-orientador: Prof. Dr. Diogo Stuani Alves

A Banca Examinadora composta pelos membros abaixo aprovou esta Tese:

Profa. Dra. Katia Lucchesi Cavalca Dedini

Prof. Dr. Ilmar Ferreira Santos

Prof. Dr. Athanasios Chasalevris

Prof. Dr. Hans Ingo Weber

Prof. Dr. Carlos Alberto Bavastri

A Ata de Defesa com as respectivas assinaturas dos membros encontra-se no SIGA/Sistema de Fluxo de Dissertação/Tese e na Secretaria do Programa da Unidade.

Campinas, 12 de Julho de 2024

Acknowledgments

I would like to express my heartfelt gratitude to all those who directly or indirectly contributed to the completion of this work. In special, I would like to thank my parents Evelio and Ivone, without whom any of this would have been possible. I am also profoundly grateful to my partner, Victoria, for her love and support, without whom everything would have been harder.

I also would like to thank my advisor Prof. Katia and co-advisor Prof. Diogo for the opportunity, the knowledge passed and, the guidance that allowed this Phd thesis to come to form.

Last but not least, I wish to extend my thanks to all my colleagues at LAMAR for the company and help in many situations during the development of this thesis.

This study was financed in part by The Brazilian National Council for Scientific and Technological Development (CNPq), grant #140275/2021-5

Resumo

Máquinas rotativas consistem, em geral, de partes girantes, como eixos, discos e pás; e mancais, que possibilitam que estes últimos girem livremente. Dentre os diferentes tipos de mancais, os mancais hidrodinâmicos ou de filme de fluido são muito usados em um grande número de máquinas. Mancais do tipo cilíndricos, ou *journal*, são o tipo mais simples de mancais hidrodinâmicos. Estes utilizam uma fina camada de lubrificante, frequentemente óleo, e conseguem suportar altas cargas, além de apresentar baixo atrito. No entanto, apesar de suas diversas vantagens, rotores com mancais hidrodinâmicos apresentam fenômenos particulares devido a interação entre fluido e eixo que giram. Estes fenômenos podem ser classificados em dois tipos: *oil-whirl* e *oil-whip*. No *oil-whirl*, um componente sub-síncrono de aproximadamente 0.5 vezes a velocidade de rotação surge no espectro da resposta. Alternativamente, o *oil-whip* apresenta uma frequência não síncrona, que é relacionada com a frequência natural do rotor, e seu surgimento apresenta condição de alto risco muito grande para o sistema rotativo, pois pode ocasionar danos consideráveis neste. Devido a natureza dos mancais cilíndricos, estes inevitavelmente se encontram em condição de *oil-whip*, a medida que uma rotação limite seja ultrapassada. Apesar disso, podem ocorrer situações em que a ocorrência do *oil-whirl* anteceda o fenômeno mais crítico de *oil-whip*, o que representa um comportamento seguro para a máquina.

Grande parte do projeto de rotores é feito por meio de análises lineares. No entanto, a detecção to tipo de instabilidade não pode ser feita utilizando os métodos tradicionais da teoria linear. O fenômeno da instabilidade fluido-induzida pode ser observado através das lentes da teoria de bifurcação como correspondendo a uma bifurcação de Hopf. Esta, por sua vez, pode ser super-crítica ou sub-crítica. O primeiro caso corresponde ao *oil-whirl*, havendo a criação de ciclos limites estáveis após o do limiar de instabilidade, enquanto que o segundo ao *oil-whip*, onde ciclos limites instáveis emergem. Desse modo, é possível detectar se um sistema rotativo vai apresentar *oil-whirl* ou *oil-whip* sabendo o tipo de bifurcação presente. Este trabalho apresenta uma abordagem para prever o tipo de bifurcação de Hopf de sistemas rotativos por meio do método da redução pela variedade central (CMR da sigla em inglês). A base do método consiste em obter a variedade central to sistema e estudar se este apresenta *oil-whirl* ou *oil-whip*. A principal contribuição deste trabalho é a utilização do método da parametrização de variedades ou superfícies invariantes para obter a variedade central, que possibilita a aplicação em sistemas rotativos de altas dimensões e estende grandemente a aplicação do CMR na obtenção de ciclos limites que surgem de bifurcações de Hopf, que, em abordagens anteriores, estavam limitadas apenas para regiões próximas do ponto de bifurcação. Além de estudos numéricos, este trabalho apresenta experimentos onde alguns parâmetros do sistema são alterados e o tipo de instabilidade é aferido e comparado com previsões teóricas.

Palavras Chaves: Dinâmica de rotores; mancais hidrodinâmicos; instabilidade fluido-induzida; bifurcação de Hopf; redução pela variedade central.

Abstract

Rotating machines generally consist of rotating parts, containing the shaft, disks and blades, and bearings, which allow the latter to rotate freely. Among the different types of bearings, hydrodynamic or fluid-film bearings find very common use in a wide range of machines. Plain or cylindrical journal bearings are the simplest type of fluid-film bearings. Using a small amount of lubricant, usually oil, these bearings can withstand a large load while also providing low friction. However, despite their many advantages, rotors supported by fluid-film bearings are known to present particular phenomena due to the interaction between the rotating fluid and shaft. These phenomena can be classified into two distinct types: oil-whirl and oil-whip. In oil-whirl, a subsynchronous component approximately 0.5 times the rotor speed, becomes evident in the response spectrum. Conversely, oil-whip presents a nonsynchronous frequency in the spectrum, correlated with the rotor's first critical speed, posing a severe threat to the rotor system as it can result in significant damage. Owing to the nature of plain bearings, they inevitably exhibit oil-whip once a certain threshold speed is exceeded. However, there are instances where oil-whirl may manifest before the more hazardous oil-whip, representing a safer operational behavior for the machine.

The design of rotors is mostly performed through linear analysis. The detection of the type of instability, however, cannot be done through traditional linear theory. The phenomenon of fluid-induced instability can be seen through the lens of bifurcation theory as corresponding to a Hopf bifurcation, which can be either super- or sub-critical. Here, the former case corresponds to oil-whirl, as there is the creation of stable limit cycles after the onset speed of instability, while the latter to oil-whip, in which unstable cycles are created. Hence, detecting the type of Hopf bifurcation, tells whether one experiences oil-whirl or oil-whip. This work presents an approach to predict Hopf bifurcations by means of the Center Manifold Reduction (CMR) method in rotor systems. The basis of the approach is to obtain the center manifold of the bifurcating system and study it to learn whether the system will present oil-whirl or oil-whip. The main contribution of this work lies in the use of the parameterization method for invariant manifolds to obtain the center manifold of the system, which allows the application to high-dimensional rotors and greatly extends the applicability of the CMR to estimate limit cycles arising from the Hopf bifurcation, that were, in previous approaches, limited to only a small range around the bifurcating point. In addition to numerical studies, this work presents experiments in which some parameters of the rotor are changed and the type of instability assessed and compared with the theoretical predictions.

Keywords: Rotordynamics; fluid-film bearings; fluid-induced instability; Hopf bifurcation; center manifold reduction.

List of Figures

List of Tables

Summary

1 INTRODUCTION

Rotating machines play a fundamental role in several industrial processes, as well as being important parts in the power generation. The basic components of a rotating machine are: the rotor, which consists of the shaft, discs and blades; the bearing, which supports the rotor and allows it to rotate freely; and the support structure, which fixes the bearing to the ground. The difficulty in studying these types of machines lies in the complex interaction that exists between these various components.

Among all parts of the machine, the bearing is arguably one of the most important components, as it is responsible for supporting the rotor and allowing it to rotate freely around its axis of rotation. Without bearings, the rotor would not be able to rotate stably and safely, which could cause damage to the machine or even lead to failure. In addition to supporting radial and axial loads, the bearing is responsible for reducing the friction between the rotor and stator, which minimizes the wear of the components and increases the efficiency of the machine, as it allows it to operate at higher rotations.

The choice of the type of bearing to be used in a rotating machine depends on several factors, such as the operating speed, the load to be supported and the environmental conditions. One of the most commonly used types of bearings is the hydrodynamic or journal bearing. This type uses a fluid film, usually oil, to support the load of the rotor and allow it to rotate freely. The rotation of the shaft over the fluid film creates a pressure gradient that supports it. One of the main advantages of hydrodynamic bearings is their ability to support higher loads and provide less friction compared to other types of bearings, which makes them ideal for high-load and high-speed applications.

Hydrodynamic bearings played a pivotal role in the early 1900s by revolutionizing the field of mechanical engineering and enabling the development of various industries. During this era, the expansion of heavy machinery and industrial processes was rapidly underway, and the demand for reliable and efficient bearing solutions was paramount. Fluid-film bearings provided a groundbreaking solution by replacing traditional plain bearings and babbitt bearings with a self-lubricating, low-friction design. This innovation allowed the development of higher-speed and heavier machinery, such as turbines, engines, and generators, which were essential for powering the industrial revolution. By separating the shaft and bearing surfaces by a thin film of lubricating fluid, fluid-film bearings significantly reduced friction, wear, and heat generation, ultimately improving the reliability and lifespan of industrial equipment. Their importance in the early 1900s marked a significant step in the advancement of mechanical engineering and the rapid growth of many industries.

The simplest type of journal bearing consists of a cylindrical shaft rotating within a cylindrical sleeve, known as plain journal bearings. However, one significant concern

in these bearings is the presence of fluid instabilities. These can lead to undesirable vibrations and, in extreme cases, catastrophic failure of the bearing or machine. In order to counteract this, different bearing geometries have been proposed, such as elliptical bore, pressure dam, and tilting pad bearings, which make the bearing less prone to instabilities and increase the efficiency of the machine (VANCE et al., 2010). Despite the issues pointed out above, plain journal bearings still find use in several applications mainly due to their simplicity, ease of manufacture, and low cost.

The discovery of fluid instabilities has puzzled researchers for many years since it was first identified around the 1920s (NEWKIRK, 1924). Since then, it was established that there exist two kinds of phenomena, namely oil-whirl and oil-whip (MUSZYNSKA, 1988). In the first kind, a subsynchronous component, approximately 0.5× the rotor speed, appears in the spectrum of the response. Despite oil-whirl being classified as an unstable regime, sometimes it is possible to operate during its occurrence (as the experiments performed in this work showed). On the other hand, oil-whip displays a non-synchronous frequency in the spectrum, related to the first critical speed of the rotor, and it is a very dangerous phenomenon that can cause great damage to the rotor system. It is important to mention that, *in plain journal bearings, oil-whirl is always followed by oil-whip*. This is simply a feature of this type of bearing. However, depending on the bearing parameters and the rotor system, *there can be cases in which oil-whip can suddenly appear*. It is preferable to encounter oil-whirl before oil-whip because it serves as an early warning signal for the machine to be stopped.

This work is mainly concerned with the oil-whirl/whip phenomena, specifically in what circumstances the rotor might display oil-whip directly, without the warning signs of oil-whirl. An important fact about this endeavor is that fluid instability is a purely nonlinear phenomenon, and cannot be predicted by means of the linearized dynamic coefficients approach (LUND, 1987). In this manner, the kind of instability is detected using the concept of center manifolds (TROGER; STEINDL, 1991). The main advantage of this approach is its applicability to high-dimensional dynamical systems, which allows a practical application in real rotating machines with many degrees of freedom (DOFs).

1.1 Objectives and original contributions

This work is focused on the study of fluid-induced instabilities that arise in rotors with hydrodynamic bearings. An approach to predict Hopf bifurcations by means of the Center Manifold Reduction (CMR) method in rotor systems is introduced. The main original contribution lies in the application of the parameterization method for invariant manifolds (HARO et al., 2016) to obtain the center manifold of the system. The parameterization method provides a powerful approach to obtain invariant manifolds of

dynamical systems and greatly improves the range of validity of the CMR method. In addition to this, the work also presents an original method to obtain quasi-periodic solutions of rotors with unbalance and fluid-instability based on an extended CMR approach. Some other objectives and contributions are:

- A clarification of the fluid-induced instabilities in light of the knowledge of nonlinear vibrations and bifurcation theory;
- The presentation of an analytical method that can predict bifurcations in rotor systems in a fast and accurate way. This is an advantage to purely numerical approaches such as continuation methods and finite difference techniques;
- Experimental observations on the effect of disk position and bearing clearance in the occurrence of oil-whirl and oil-whip;

1.2 Manuscript outline

The rest of this thesis is divided as:

- In Chapter 2 a review of the current literature on the most important topics related to this work is performed;
- The theory developed is reported in Chapter 3;
- Chapter 4 describes the test rig used to perform the experiments;
- The results of this work are reported in two chapters: the numerical study in Chapter 5, and the experimental in Chapter 6;
- The manuscript ends with some conclusions in Chapter 7.

2 LITERATURE REVIEW

2.1 Fluid-induced instabilities: oil-whirl and oil-whip

Despite the several advantages brought by the use of journal bearings, its operation came with an inherent problem, namely the fluid-induced instability. The discovery of such a phenomenon in the early 1900s attracted a lot of attention from researchers and designers. One of the first accounts of this phenomenon was reported by Newkirk (1924). Later, Newkirk and Taylor (1925) identified the phenomenon as due to the oil flow, and termed the name oil-whip, where whipping was defined as a high amplitude whirling outside a major critical speed. They also provided more accounts of the phenomenon, studying the influence of several parameters including misalignment, radial clearance, bearing length, and oil supply. In addition, they hypothesized an explanation of the mechanisms at play, i. e., that the oil flow comes into resonance with the rotor at about twice the critical speed (Figure 2.1). Kimball (1925) suggested that frictional effects between the oil and the rotating shaft are the main cause of oil-whip. This was a nonintuitive hypothesis as friction is generally seen as providing damping, which has a stabilizing effect. Smith (1933) deduced the equations of motion considering a flexible shaft and a symmetric and unsymmetric bearing. He concluded that the cross-coupled bearing coefficients were the major feature leading to the loss of stability. The explanation of the oil flow and frictional effects supplied a better understanding of the phenomenon of fluid instability, but it still did not cover the fact that oil-whip emerges at about twice

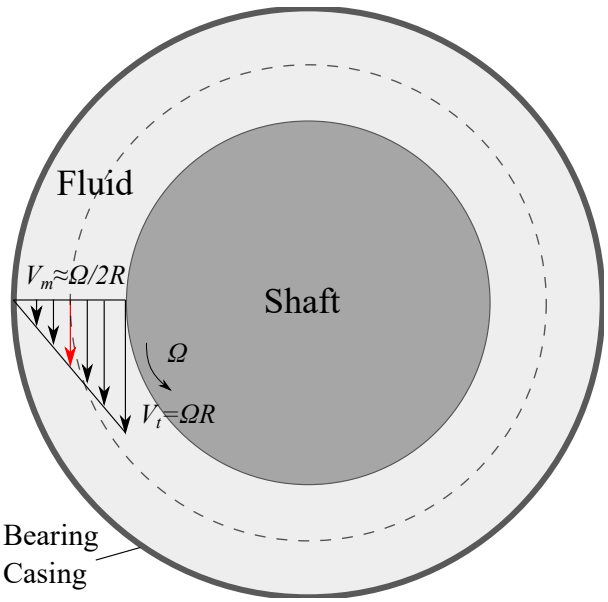

Figure 2.1: Newkirk explanation of oil-whip: as the shaft rotates, the fluid starts to display a velocity field. At around the midspan of the radial clearance, the fluid will have a velocity of approximately $V_m \approx \Omega/2R$. Hence, when the speed reaches twice the critical speed, the fluid speed will match the natural frequency of the rotor, causing oil-whip.

the critical speeds but it maintains for higher speeds as well.

Robertson (1933) provided some theoretical calculations that suggested the shaft with fluid-film bearings was unstable at all speeds. However, his analysis considered the negative pressure region of the hydrodynamic pressure distribution. By neglecting such region, Poritsky (1953) was able to show the existence of a radial component that stabilizes the system up until around twice the first critical speed. Nonetheless, these theoretical results were not in agreement with later experiments done by Newkirk and Lewis (1956) and Newkirk (1956) that reported cases in which oil-whip does not develop prior to five or six times the first critical speed. In addition, Pinkus (1956) reported a hysteresis effect, where a heavy and light rotor showed different onset of instability, and a transient region before the rotor enters into full oil-whip. Later, Hori (1959) summarized the experimental results and developed a theoretical approach explaining them.

Despite a good understanding of the causes and effects of fluid instability phenomenon, there still was no clear distinction between oil-whip and oil-whirl, and many researchers did not consider the latter case to be an unstable regime. Muszynska (1986, 1988, 2005) performed extensive numerical and experimental work on the fluid instability phenomenon. She defined that oil-whirl consists of a subharmonic vibration in which the rotor vibrates at around 0.5× the shaft speed, and the rotor presents a shape related to its rigid body mode. Oil-whip was defined as a non-synchronous vibration, where the rotor vibrates at a constant frequency that is close to the first critical speed of the system. In this regime, the rotor presents a shape related to the first flexible mode. Both oil-whirl and oil-whip are independent of the amount of unbalance in the rotor system, which makes them a self-excited vibration, an inherent nonlinear phenomenon where there exists a transfer of energy within the vibrating system (NAYFEH; BALACHANDRAN, 1995).

Since the 80s, researchers had already a good grasp on the causes and mechanisms related to fluid instability. The research that followed clarified some aspects of oil-whirl/whip. Tonnesen and Lund (1978) studied the occurrence of fluid instability in a light and heavy rotor. They showed that adding damping to the supports stabilized the system. Chauvin Jr. (2003) experimentally studied the effects of oil and bearing temperature, as well as the occurrence of fluid instability at low eccentricities. El-Shafei et al. (2004) performed experiments in a flexible rotor on two plain bearings. They showed the effects of unbalance levels, fluid pressures and coupling misalignments on the oil-whirl/whip. de Castro et al. (2008) studied the effects of unbalance in a rotor with journal bearings using the infinitely short bearing assumptions, validating its results with experiments. Fan et al. (2011) performed experiments to study the dynamics of a rotor subjected to oil-whip and annular rubbing, and proposed a method based on the Hilbert transform to predict these phenomena from a rotor start-up response. Safizadeh and

Golmohammadi (2020) proposed a technique to detect oil-whirl/whip using multi-sensor data fusion.

2.1.1 When does oil-whirl or oil-whip occur?

The occurrence of either oil-whirl or oil-whip, in plain bearings, mainly depends on the position of the shaft on the locus at the unstable speed. To illustrate this, Figure 2.2 shows the hydrodynamic forces in the auxiliary frame rotating with the shaft whirl as a function of the dimensionless eccentricity $\varepsilon = e/c_r$, being c_r the radial clearance. As the journal gets closer to the bearing's center (eccentricity decreases) the tangential component of the oil-film force, which is destabilizing, gets stronger than the radial component, which is stabilizing. Oil-whip is triggered when the tangential component reaches sufficient strength to displace the shaft significantly from its equilibrium position, as illustrated in Fig. 2.3a. Conversely, when this tangential force is comparatively weaker, oil-whirl ensues. In the case of oil-whirl, the amplitude of the journal inside the bearing increases but remains much closer to the equilibrium, as Fig. 2.3b shows.

The above discussion implies that higher eccentricities or reduced attitude angles are more prone to induce oil-whirl rather than oil-whip in the rotor system. However, even when the rotor displays oil-whirl, as the speed increases, the shaft will get closer and closer to the bearing center (the eccentricity will decrease) and, for plain bearings, oil-whip is inevitable. Nonetheless, it is much better to have oil-whirl prior to oil-whip as a warning sign, so that the machine is stopped immediately and oil-whip is avoided. It is worth mentioning that this analysis is merely qualitative, and it cannot be used to precisely point out when a rotor will experience oil-whip or oil-whirl.

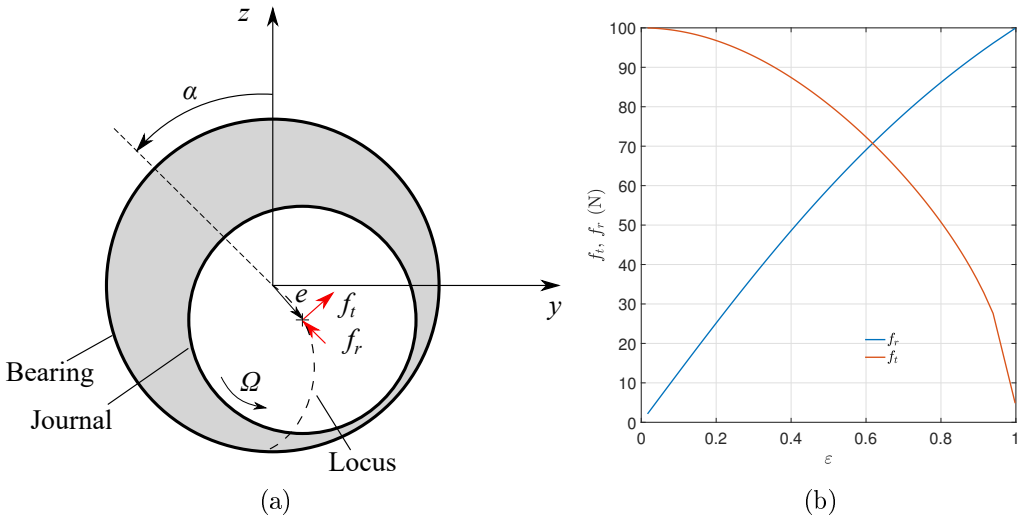

(a) (b)

Figure 2.2: Forces on a journal bearing as a function of eccentricity.

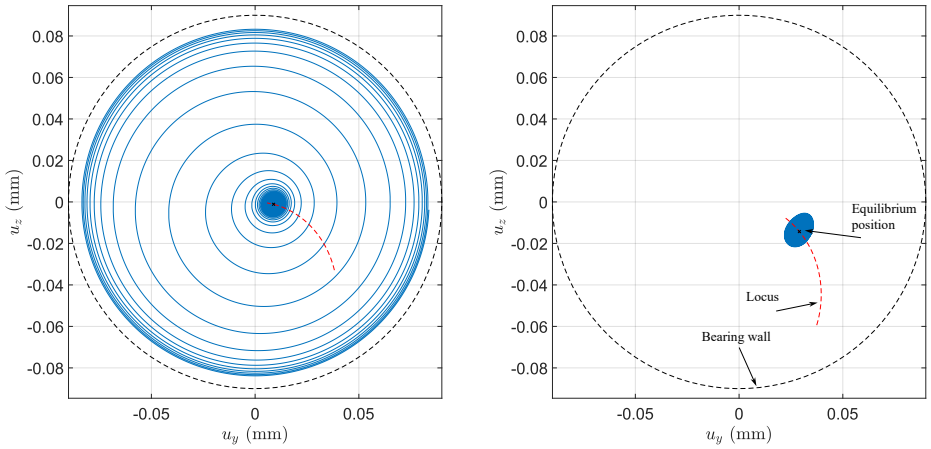

(a) (b)

Figure 2.3: Typical oil-whip (a) and oil-whirl (b) response for an initial condition close to the equilibrium. Note the difference between the equilibrium position along the locus in both cases.

2.2 Hydrodynamic forces using linearized dynamic coefficients

It is common practice in rotordynamics to model the effect of bearings using linearized dynamic coefficients. In this case, instead of considering the full model of the hydrodynamic force, the bearing is included as a spring-damper system in the rotor model. Hence, the bearing force is often given as,

$$\begin{Bmatrix} f_y \\ f_z \end{Bmatrix} = \begin{bmatrix} k_{yy} & k_{yz} \\ k_{zy} & k_{zz} \end{bmatrix} \begin{Bmatrix} u_y \\ u_z \end{Bmatrix} + \begin{bmatrix} c_{yy} & c_{yz} \\ c_{zy} & c_{zz} \end{bmatrix} \begin{Bmatrix} \dot{u}_y \\ \dot{u}_z \end{Bmatrix} \tag{2.1}$$

where k_{ij} and c_{ij} $(i, j = yy, zz, yz, zy)$ are the stiffness and damping coefficients. Figure 2.4 depicts this approach to represent the bearing. These coefficients can be obtained directly from the solution of the hydrodynamic pressure, and it is a very simple and effective way to model rotor systems. Stability analysis can be performed by including the coefficients in the finite element model of the rotor and studying the eigenvalues of the system (FRISWELL et al., 2010). When the real part of any eigenvalue crosses the real line, the system becomes unstable, indicating fluid instability.

The onset speed of the fluid instability can be reliably obtained using the model of Eq. (2.1), provided the coefficients are accurate. A lot of work has been done to correctly obtain these coefficients and the onset of oil-whirl/whip. Lund (1987) reviewed this approach and discussed its limitations. Elrod and Vijayaraghan (1994, 1995) included the effects of cavitation in the obtention of stability boundaries. Guo and Kirk (2003b, 2003a) studied the effect of damping in the unstable regions. They showed that damping,

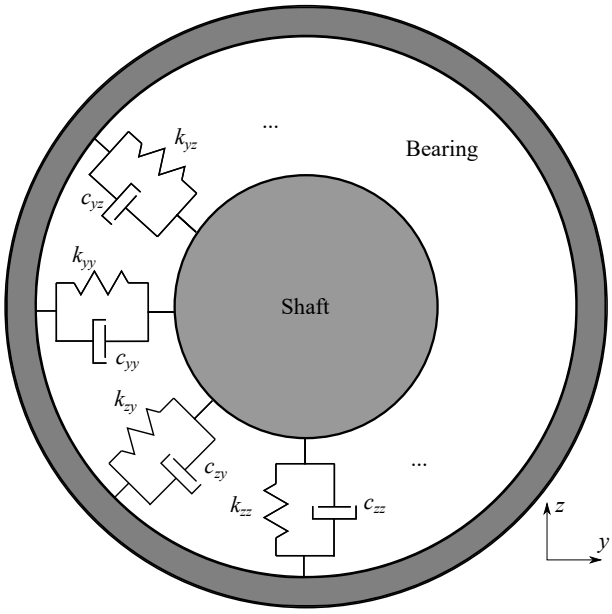

Figure 2.4: Modeling the hydrodynamic forces on a journal bearing using dynamic coefficients.

either in the shaft or in the bearing support, can suppress the fluid instability. Along these lines, Sorge (2008) proposed using dry friction in the journal housings to provide damping and reduce or eliminate oil-whip. Someya (1989) provided extensive sample calculations of dynamic coefficients for several types of bearings and in different configurations.

Some works focused on obtaining the dynamic coefficients experimentally. Zhang at al. (1992b, 1992a) presented a frequency-based technique to obtain the dynamic coefficients and applied it to numerical and experimental studies. Tieu and Qiu (1994) proposed a method that can detect the coefficients using unbalanced responses, excluding the need for complex excitation equipment. Tiwari and Chakravarthy (2009) presented a method for the simultaneous estimation of the bearing parameters and residual unbalance in a rigid rotor. Li et al. (2016) proposed a time-domain-based method consisting in reconstructing the oil-film forces in order to obtain the dynamic coefficients.

Despite the effectiveness of the dynamic coefficients approach to model the fluid-film forces and in to obtain the onset speed of instability, it cannot be used to know if the rotor will display oil-whirl or oil-whip. Since the force in Eq. (2.1) is linear, the stability is given by the eigenvalues of the system. The transient response when a real part of an eigenvalue crosses the real line is simply an exponentially increasing amplitude. However, the nonlinear analysis, and the experiments for that matter, clearly show that the system amplitude reaches a limit cycle in the oil-whirl and it is limited by the radial clearance in the oil-whip (see Fig. 2.3). Therefore, to know the type of fluid instability, one has to rely on nonlinear analyses such as the ones presented in the following sections.

2.3 Hopf bifurcation theory

As shown in Fig. 2.3, the oil-whirl/whip phenomena consist in the origination of limit cycles in the dynamics of the system. Limit cycles can only occur in nonlinear systems (STROGATZ, 2018), and hence, one cannot use the traditional approach of using linearized dynamic coefficients, reviewed in the last section, to study these cycles. The most basic way in which a limit cycle is created is through a Hopf bifurcation (or Andronov-Hopf). Consider a dynamical system given by the following equation of motion,

$$\dot{\mathbf{x}} = \mathbf{f}(\mathbf{x}, \xi) \tag{2.2}$$

where $\mathbf{x} \in \mathbb{R}^N$ contains the displacements and velocities, $\mathbf{f} : \mathbb{R}^N \times \mathbb{R} \to \mathbb{R}^N$ is a nonlinear map describing the dynamics and $\xi \in \mathbb{R}$ a parameter. The conditions for the occurrence of a Hopf bifurcation in this dynamical system are (HASSARD et al., 1981; WANG; KHONSARI, 2006a):

- The system has an equilibrium solution $\mathbf{x}_0 = \mathbf{x}_0(\xi)$;
- The jacobian $\mathbf{f}_\mathbf{x}(\xi) = \partial\mathbf{f}/\partial\mathbf{x}$ has a pair of complex conjugate eigenvalues $\lambda(\xi) = \sigma(\xi) \pm j\omega(\xi)$ such that when the parameter crosses a critical value $\xi > \xi_c$, one has $\sigma(\xi_c) = 0$ and $\omega(\xi_c) = \omega_0$. Also, the remaining eigenvalues have negative real parts, which means that only one mode becomes unstable;
- $\mathbf{f}$ is analytic in the neighborhood of $(\mathbf{x}, \xi) = (\mathbf{x}_0, \xi_c)$;
- The rate of change of the real part of the eigenvalue with respect to the parameter satisfies $d\sigma(\xi)/d\xi \neq 0$.

For a rotor on fluid-film bearings, perfectly balanced, one can find that all the above conditions hold by assuming the parameter ξ as the shaft speed Ω. A Hopf bifurcation can lead to two types of behavior, which are labeled super-critical and sub-critical. The difference between the two lies in the stability type of the limit cycles, which are stable in the super-critical case and exist for $\Omega > \omega_{th}$, and unstable for the sub-critical case and exist for $\Omega < \omega_{th}$, where ω_{th} denotes the onset speed of instability. Figure 2.5 depicts the two kinds of Hopf bifurcations and their effects on the system's dynamics. Starting from the super-critical case, Figure 2.5a, when the speed is $\Omega < \omega_{th}$, the rotor has a stable equilibrium solution. Hence, when an initial condition A is given, the system will arrive at this solution. However, after $\Omega > \omega_{th}$, this equilibrium solution becomes unstable and a limit cycle emerges due to the Hopf bifurcation. When two initial conditions B and B' are given, the rotor will always tend to the limit cycle. One may relate this behavior to the oil-whirl shown in Fig. 2.3b. The other case is presented in Figure 2.5b, where there is the emergence of an unstable limit cycle (also known as stability envelope) that

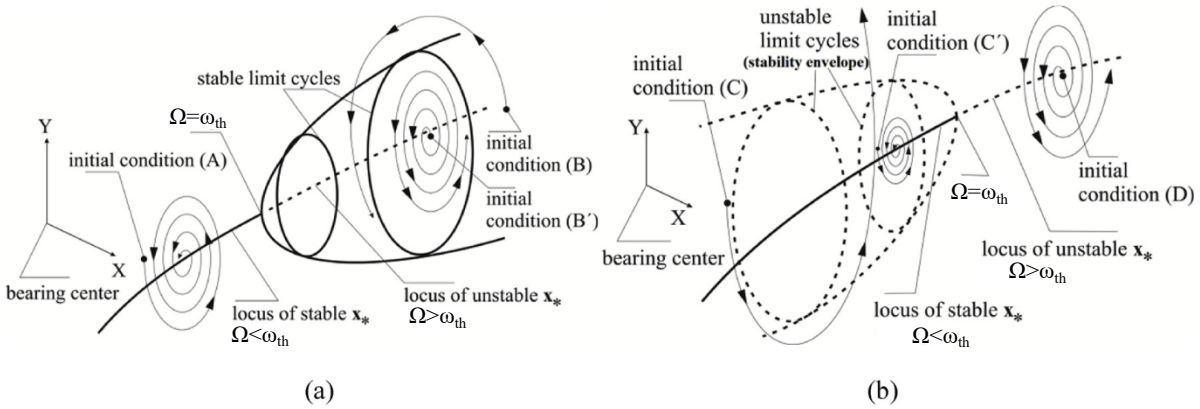

Figure 2.5: Types of Hopf bifurcations and their effects on the dynamics: super-critical (a) and sub-critical (b) (Source: Chasalevris (2020)).

extends prior to the threshold speed ω_{th}. When $\Omega < \omega_{th}$, the rotor has both the stable equilibrium and the unstable limit cycles. Depending on the initial condition, it may or may not reach the equilibrium curve as shown in Fig. 2.5b. As the threshold speed is passed, the equilibrium solution becomes again unstable, but now there are no other stable solutions nearby and the amplitude of the system may reach very high levels. This behavior resembles the oil-whip case observed in Fig. 2.3a.

The above discussion indicates that the type of Hopf bifurcation will dictate whether one will experience oil-whirl or oil-whip. It is also worth noting that, in the sub-critical case, oil-whip can be triggered before the onset speed ω_{th}, provided a strong enough disturbance is given to the rotor. Therefore, in addition to the instability threshold, the type of bifurcation and the amplitude of the emerging limit cycles become critical design parameters to ensure a safe operating regime for the machine.

A lot of research was done aiming at estimating the limit cycles. Myers (1984) and Hollis and Taylor (1986) applied Hopf bifurcation theory on a rigid rotor supported by fluid bearings. The former used the infinitely long (Sommerfeld) model to represent the hydrodynamic forces, while the latter used the infinitely short (Ocvirk) bearing approximation. The approach consists in performing a Taylor expansion of the hydrodynamic forces up to the third order. The information on the stability of the emerging limit cycles is contained in the second and third components of the force. Hollis and Taylor also showed that the type of bifurcation depends on the bearing parameters as well as the load. A similar study was also performed by Wang and Khonsari (2005). The same authors also studied the effect of fluid turbulence (WANG; KHONSARI, 2006a) and the effect of shaft flexibility (WANG; KHONSARI, 2006b) in the fluid instability. These studies examine basic rotor systems (Jeffcott model), but the method can be used for complex turbine-generator systems, as demonstrated by Chasalevris (2020). The research on Hopf bifurcation showed that the parameters of the bearing and the flexibility of the shaft can

affect the type of bifurcation present in the system. In addition, experimental evidence of the bifurcation phenomenon was given by Deepak and Noah (1998), who observed the existence of super-critical and sub-critical solutions.

2.4 Center manifold reduction

The basis of the Hopf bifurcation theory lies in studying the dynamics of a system on its center manifold. The center manifold is a type of invariant manifold, the others being the stable and unstable manifolds (WIGGINS, 2003). In the context of vibrating systems, invariant manifolds can be seen as extensions of the modes of vibration. While the latter is a hyper-plane in the phase space, the former is a curved hyper-surface, that accounts for the nonlinearities present in the system. To illustrate this fact, consider the following nonlinear two DOF spring-mass-damper system shown in Fig. 2.6. The equation of motion is given as,

$$\mathbf{M}\ddot{\mathbf{x}} + \mathbf{C}\dot{\mathbf{x}} + \mathbf{K}\mathbf{x} = \mathbf{f}(\mathbf{x}), \tag{2.3}$$

where,

$$\mathbf{x} = \begin{Bmatrix} x_1 \\ x_2 \end{Bmatrix}, \ \mathbf{M} = \begin{bmatrix} m & 0 \\ 0 & m \end{bmatrix}, \ \mathbf{C} = \begin{bmatrix} c & -c \\ -c & 2c \end{bmatrix}, \ \mathbf{K} = \begin{bmatrix} 2k & -k \\ -k & 2k \end{bmatrix}, \ \mathbf{f}(\mathbf{x}) = \begin{Bmatrix} -\gamma x_1^3 \\ 0 \end{Bmatrix}, \tag{2.4}$$

with $m = 1$ kg, $c = 0.03$ Ns/m, $k = 1$ N/m, and $\gamma = 0.5$ N/m^3. The system exhibits two distinct modes: one wherein the masses move in synchrony, and another where they move in opposite directions. These modes can be seen as motions occurring in a hyper-plane on the phase space, which has four dimensions. Figure 2.7a illustrate this. When no nonlinearities are present ($\gamma = 0$), the long-term dynamics of the system can be completely described by two planes, which represent the vibration modes. If an initial condition is given in one plane, the response will remain on it for all time. This means that these planes are *invariant* under the dynamics. This behavior is completely changed when the nonlinearity is considered ($\gamma \neq 0$), as Fig. 2.7b shows. Now an initial condition in either plane does not remain on it, but leaves, taking over a broad range in the phase space.

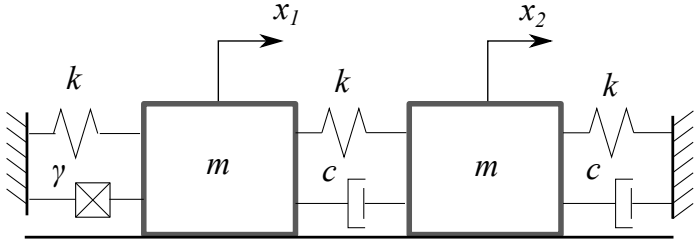

Figure 2.6: spring-mass-damper system with nonlinear spring.

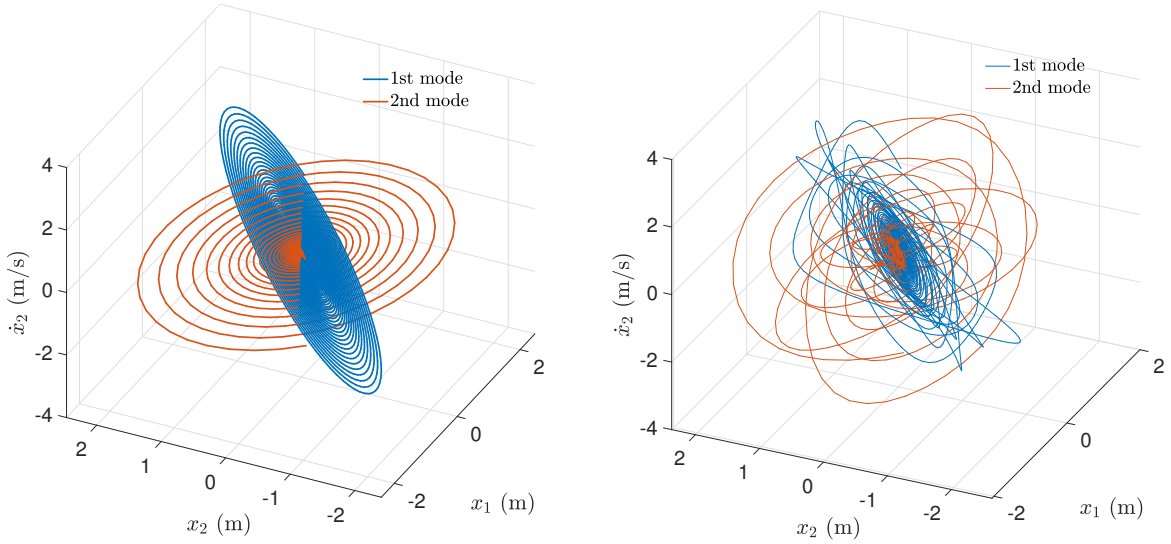

(a) (b)

Figure 2.7: Modes of a linear spring-mass-damper system can be seen as planes in the phase space (a), which are invariant under the dynamics. However, the invariant property is no longer valid when nonlinearity is considered (b).

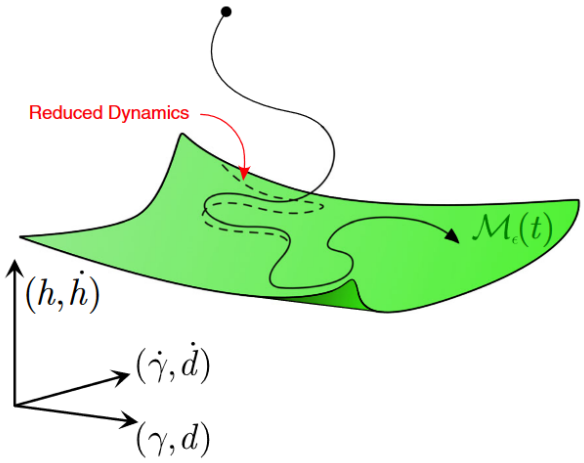

Figure 2.8: Illustration of the trajectory in phase space being attracted to an invariant manifold: the dashed line is the dynamics on the manifold while the solid line is the full trajectory. Here h, $\dot{h}$, γ, $\dot{\gamma}$, d and $\dot{d}$ represent state variables of the dynamical system (Source: Haller and Ponsioen (2017)).

However, one can still find an invariant quantity, namely an invariant manifold, which has the same properties as the vibration modes in the linear system. In this case, the manifolds are curved surfaces, tangent to the planes at the equilibrium, which take into account the exchange of energy between the vibrating modes. Because of the similarities to linear modes, Shaw and Pierre (1993) called these invariant manifolds the nonlinear normal modes (NNMs).

The center manifold is also an invariant quantity, and it is an extension of the vibration mode that becomes unstable at the Hopf bifurcation. Because near the bifurcating point the real part of the eigenvalue of the unstable mode becomes very close to zero, making it a slow mode (HALLER; PONSIOEN, 2017), the dynamics of the system will be attracted to the center manifold as time moves on, as depicted in Figure 2.8. This means that one can describe the dynamics of the system by only studying what happens on the center manifold (TROGER; STEINDL, 1991). The limitation of this approach is that it is only valid in the neighborhood of the bifurcation, since as one moves away from it, the center manifold turns into a regular stable or unstable manifold (depending on the direction).

The use of center manifolds to obtain the limit cycles is known as center manifold reduction (CMR), which is equivalent to the application of Hopf bifurcation theory. There are a limited number of papers that studied the Hopf bifurcation of rotors with fluid bearings using the CMR. Boyaci et al. (2009) used the CMR to estimate the bifurcation type and the amplitudes of the limit cycles in a rigid rotor on two floating-ring bearings. The results were compared with numerical continuation. Miura et al. (2017) applied the CMR in a flexible rotor with one plain bearing at the outboard side. They studied the influence of the rotor and bearing parameters on the type of bifurcation and the amplitude of the cycles. Kano et al. (2019) applied the CMR and a static reduction in a more complex rotor, with two disks and one journal bearing at the outboard side. They showed that, besides the flexibility of the shaft and the bearing parameters, the disk position can also alter the type of bifurcation and affect the amplitude of the limit cycles, in addition to providing experimental evidence for their theoretical findings.

As mentioned above, the main limitation of the CMR is that it is only valid in the region close to the bifurcating point. However, it is possible to improve the accuracy of the CMR by better approximating the center manifold. An important tool for this task is the parameterization method for invariant manifolds (HARO et al., 2016), which provides a systematic way to obtain invariant manifolds of dynamical systems. Some applications of this method in weakly damped mechanical systems in both autonomous (PONSIOEN et al., 2018; OPRENI et al., 2021; VIZZACCARO et al., 2022) and non-autonomous cases (PONSIOEN et al., 2020; TOUZÉ et al., 2021; OPRENI et al., 2023), show that the parameterization method is a fast and accurate approach to obtaining the response of nonlinear dynamical systems.

2.5 Bifurcation of cycles

In addition to the Hopf bifurcations, rotors on fluid bearings often experience a subsequent bifurcation of cycles, what is known as limit point of cycles (LPC). The LPC

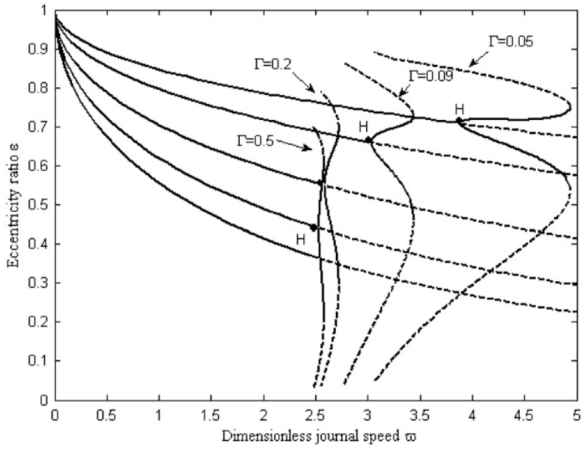

Figure 2.9: Bifurcation of cycles in a rigid rotor with fluid bearings (Source: Chouchane and Amamou (2011))

consists of a fold bifurcation and it changes the stability of the limit cycles that emerge in the Hopf point. Chouchane and Amamou (2011) performed extensive numerical studies on the bifurcation of cycles using numerical continuation. Figure 2.9 shows some of their results. In this figure, ε denotes the dimensionless eccentricity of the journal, $\bar{\omega} = \omega\sqrt{c_r/g}$ is the dimensionless speed and $\Gamma = (\mu R L_b^3)/(2m_r c_r^{2.5} g^{0.5})$ the bearing parameter [1]. The solid and dashed lines represent the stable and unstable solutions, respectively. One can note that the bifurcation of cycles changes dramatically with the bearing parameter. Kano et al. (2019) also experienced the existence of the LPC in a flexible rotor with two rigid disks by means of the shooting technique.

The existence of the bifurcation of cycles means that not only the limit cycles that emerge at the Hopf point need to be of concern, but also the global bifurcating behavior of the system because, as Fig. 2.9 presents, some solutions extend far away from the instability point.

2.6 Effect of unbalance on fluid instability

All the discussion around Fig. 2.5 is valid only for a perfectly balanced rotor supported by fluid bearings. However, the presence of mass unbalance is inherent to rotating machinery due to manufacture and assembly errors. When unbalance is considered, the equilibrium solution turns into a periodic orbit, while the limit cycles turn into quasi-periodic solutions. These quasi-periodic solutions will be a combination of the periodic orbit due to unbalance and the emergent limit cycles. Shaw and Shaw (SHAW; SHAW, 1990) studied the effect of unbalance in the fluid instability. They showed that different motions, from periodic to chaotic, can occur, depending on the ratio between the onset

[1] for the definition of the parameters one is referred to Chapter 3

speed of instability and the frequency of the limit cycle.

Rotors with fluid bearing and unbalance also display a period-doubling bifurcation, that is unrelated to the oil-whirl/whip. This phenomenon was studied by de Castro et al. (2008) and Rendl et al. (2023). These works showed that the period-doubling bifurcation is affected by the bearing parameters, the amount of unbalance, and the model used to describe the oil-film forces.

3 THEORETICAL BACKGROUND

3.1 Rotordynamic model

The mathematical model for the rotating machine is obtained through the finite element method (FEM). Figure 3.1 depicts a typical rotor system, consisting of stepped shafts, bearings and rigid disks. The shaft is modeled using Timoshenko beams elements in the two orthogonal directions, the disks are considered rigid masses with rotary inertia and the bearings are included at single nodes in the mesh. This approach is very common to model rotating machines and widely applied in practice (FRISWELL et al., 2010; VANCE et al., 2010). The ith nodal displacement is given by $\mathbf{x}^i = \{u_y^i,\ u_z^i,\ \psi_y^i,\ \psi_z^i\}^T$, being $u_{y,z}$ and $\psi_{y,z}$ the displacements and rotations, respectively, as indicated in Fig. 3.1. The equations of motion can be written as (FRISWELL et al., 2010),

$$\mathbf{M}\ddot{\mathbf{x}} + (\mathbf{C_s} + \Omega\mathbf{G})\dot{\mathbf{x}} + \mathbf{K_s}\mathbf{x} = \mathbf{f_b}(\mathbf{x}, \dot{\mathbf{x}}, \Omega) + \mathbf{f_g} + \mathbf{f_h}(\Omega t), \tag{3.1}$$

where $\mathbf{x} = \{\mathbf{x}^1,\ \mathbf{x}^2, \cdots,\ \mathbf{x}^{N_n}\}^T \in \mathbb{R}^N$ is the displacement vector of the discretized domain with N_n nodes and $N = 4N_n$ degrees of freedom (DOFs), $\Omega \in \mathbb{R}$ is the shaft rotating speed, $\mathbf{M}$, $\mathbf{C_s}$, $\mathbf{G}$ and $\mathbf{K_s} \in \mathbb{R}^{N\times N}$ are the mass, damping, gyroscopic and stiffness matrices of the shaft. One can consult any rotordynamics book, e.g., Friswell et al. (2010) or Ishida and Yamamoto (2012) about these matrices. Damping is considered proportional to the stiffness matrix, that is, $\mathbf{C_s} = \beta\mathbf{K_s}$, with $\beta = 1.5 \times 10^{-5}$ s as proposed by Liu and Novak (1995).

The external forces that act in the system are the bearing forces $\mathbf{f_b}(\mathbf{x}, \dot{\mathbf{x}}, \Omega)$, gravity $\mathbf{f_g}$, which is a constant vector acting in the center of mass of the rotor, and unbalance $\mathbf{f_h}(\Omega t)$, which is given by,

$$\mathbf{f_h}(\Omega t) = \mathbf{f_{hy}} m_{un}\Omega^2 \cos\Omega t + \mathbf{f_{hz}} m_{un}\Omega^2 \sin\Omega t. \tag{3.2}$$

Here, $\mathbf{f_{hy}}$ and $\mathbf{f_{hz}} \in \mathbb{R}^N$ are Boolean vectors that specify the nodes of the mesh where the

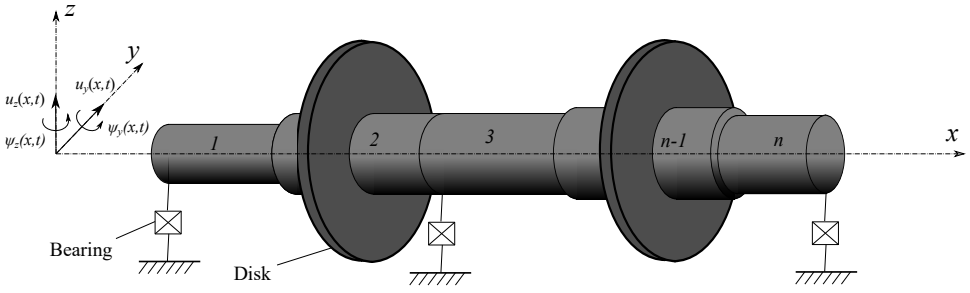

Figure 3.1: Representation of a typical rotor system.

force is applied and m_{un} represents the unbalance moment, expressed in kg·m.

In order to apply the CMR method, the hydrodynamic forces need to be in a polynomial form. This can be accomplished by expanding the term $\mathbf{f_b}(\mathbf{x}, \dot{\mathbf{x}}, \Omega)$ using Taylor series up to the third order, around the equilibrium position and with respect only to the displacements and velocity, leading to,

$$\begin{aligned}\mathbf{f_b}(\mathbf{x}, \dot{\mathbf{x}}, \Omega) &= \mathbf{f_b}(\mathbf{x}, \dot{\mathbf{x}}, \Omega)\Big|_{eq} + \frac{\partial \mathbf{f_b}(\mathbf{x}, \dot{\mathbf{x}}, \Omega)}{\partial \mathbf{x}}\Big|_{eq}(\mathbf{x} - \mathbf{x_e}) + \frac{\partial \mathbf{f_b}(\mathbf{x}, \dot{\mathbf{x}}, \Omega)}{\partial \dot{\mathbf{x}}}\Big|_{eq}\dot{\mathbf{x}} + \mathbf{f_{nl}}(\mathbf{x}, \dot{\mathbf{x}}, \Omega) \\ &= \mathbf{f_{b0}}(\Omega) - \mathbf{K_b}(\Omega)(\mathbf{x} - \mathbf{x_e}) - \mathbf{C_b}(\Omega)\dot{\mathbf{x}} + \mathbf{f_{nl}}(\mathbf{x}, \dot{\mathbf{x}}, \Omega)\end{aligned} \tag{3.3}$$

where eq means an evaluation at the equilibrium point $\mathbf{x} = \mathbf{x_e}$ and $\dot{\mathbf{x}} = \mathbf{0}$, $\mathbf{f_{b0}}(\Omega) = \mathbf{f_b}(\mathbf{x_e}, \mathbf{0}, \Omega)$ is the static bearing force, $\mathbf{K_b}(\Omega)$ and $\mathbf{C_b}(\Omega)$ are the bearing stiffness and damping matrices, and $\mathbf{f_{nl}} = \mathcal{O}(|\mathbf{x}|^2, |\mathbf{x}||\dot{\mathbf{x}}|, |\dot{\mathbf{x}}|^2)$ represents higher-order terms in the Taylor expansion. By substituting Eq. (3.3) into (3.1), one has,

$$\mathbf{M}\ddot{\mathbf{x}} + (\mathbf{C_s} + \mathbf{C_b}(\Omega) + \Omega\mathbf{G})\dot{\mathbf{x}} + (\mathbf{K_s} + \mathbf{K_b}(\Omega))\mathbf{x} = \mathbf{f_{b0}}(\Omega) + \mathbf{K_b}(\Omega)\mathbf{x_e} + \mathbf{f_{nl}}(\mathbf{x}, \dot{\mathbf{x}}, \Omega) + \mathbf{f_g} + \mathbf{f_h}(\Omega t). \tag{3.4}$$

The equilibrium position $\mathbf{x_e}$ and the static force $\mathbf{f_{b0}}$ are obtained from Eq. (3.4) by making $\mathbf{x} = \mathbf{x_e}$, $\ddot{\mathbf{x}} = \dot{\mathbf{x}} = \mathbf{f_h} = \mathbf{0}$, which leads to,

$$\mathbf{K_s}\mathbf{x_e} = \mathbf{f_{b0}}(\mathbf{x_e}, \Omega) + \mathbf{f_g}. \tag{3.5}$$

Equation (3.5) is a nonlinear algebraic equation that needs to be solved for $\mathbf{x_e}$. It is worth noting that, although not explicitly shown, this equation depends on the speed Ω because of the hydrodynamic force term $\mathbf{f_{b0}}(\Omega) = \mathbf{f_b}(\mathbf{x_e}, \mathbf{0}, \Omega)$, and its solution gives the locus of the rotor.

To apply the CMR, it is also required to write the system with respect to the equilibrium position, making it the origin of the system. Let $\mathbf{y} = \mathbf{x} - \mathbf{x_e}$. Using this new coordinate system, Equation (3.4) will now read,

$$\mathbf{M}\ddot{\mathbf{y}} + \mathbf{D}(\Omega)\dot{\mathbf{y}} + \mathbf{K}(\Omega)\mathbf{y} = \mathbf{f_{nl}}(\mathbf{y}, \dot{\mathbf{y}}, \Omega) + \mathbf{f_h}(\Omega t), \tag{3.6}$$

where Eq. (3.5) was used and,

$$\mathbf{D}(\Omega) = \mathbf{C_s} + \mathbf{C_b}(\Omega) + \Omega\mathbf{G}, \quad \mathbf{K} = \mathbf{K_s} + \mathbf{K_b}(\Omega). \tag{3.7}$$

3.2 Hydrodynamic bearing forces

The force $\mathbf{f_b}$ in Eq. (3.1) comes from the hydrodynamic effect of the rotating oil-film. This force is obtained in this work by solving the isoviscous Reynolds equation,

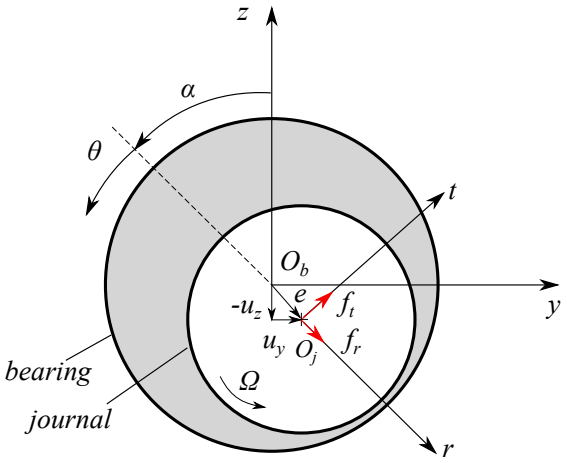

Figure 3.2: Bearing geometry and hydrodynamic forces

which is given as (HAMROCK et al., 2004),

$$\frac{1}{R^2}\frac{\partial}{\partial\theta}\left(h^3\frac{\partial p}{\partial\theta}\right)+\frac{\partial}{\partial x}\left(h^3\frac{\partial p}{\partial x}\right)=6\mu\Omega\frac{\partial h}{\partial\theta}+12\mu\frac{\partial h}{\partial t}, \tag{3.8}$$

in which $p = p(\theta, x)$ is the pressure distribution, R the journal radius, h the fluid-film thickness, θ and x the circumferential and axial coordinates. The oil-film thickness is given as (SZERI, 1998; MIRASKARI et al., 2017a),

$$h = c_r + R + e\cos\theta - R\sqrt{1-\left(\frac{e}{R}\right)^2\sin^2\theta} \tag{3.9}$$

where $e = \sqrt{u_y^2 + u_z^2}$ is the eccentricity and c_r is the radial clearance. Since the typical clearance in journal bearings is much smaller than the journal radius $c_r \ll R$, the term $(e/R)^2$ has a negligible contribution and can often be ignored. Hence, the thickness is given simply as,

$$h = c_r + e\cos\theta = c_r(1+\varepsilon\cos\theta) \tag{3.10}$$

being $\varepsilon = e/c_r$. The isoviscous Reynolds equation is often solved by means of an numerical procedure such as the FEM or finite volume method (FVM) (VERSTEEG; MALALASEKERA, 1995). However, in this work, an approximation is made to solve Eq (3.8), namely, the bearing is considered infinitely short. This solution is obtained by neglecting the circumferential gradient in Eq. (3.8), that is $\partial p/\partial\theta = 0$, allowing the obtention of a closed-form expression for the hydrodynamic pressure as,

$$p(\theta, x) = \left(\frac{3\mu L_b^2}{c_r^2}\right)\frac{\varepsilon(\Omega - 2\dot{\alpha})\sin\theta - 2\dot{\varepsilon}\cos\theta}{(1+\varepsilon\cos\theta)^3}\left(\left(\frac{x}{L_b}\right)^2 - \frac{1}{4}\right), \tag{3.11}$$

where L_b is the bearing length and $\dot{\alpha}$ denotes the whirl speed, which is given as,

$$\dot{\alpha} = \frac{u_y \dot{u}_z - u_z \dot{u}_y}{c_r^2 \varepsilon^2}. \tag{3.12}$$

With the pressure distribution at hand, the forces in the frame rotating with the shaft whirl ($r - t$ in Fig. 3.2) is obtained as,

$$\begin{Bmatrix} f_r \\ f_t \end{Bmatrix} = \int_0^{\theta_1} \int_{-L_b/2}^{L_b/2} p(\theta, x) \begin{Bmatrix} \cos\theta \\ \sin\theta \end{Bmatrix} dx R d\theta. \tag{3.13}$$

The integrations (3.13) are performed assuming $\theta_1 = \pi$, which is known as the π-film or half-Sommerfeld boundary condition, giving the following expressions (WANG; KHONSARI, 2006b),

$$f_r = -\frac{\mu R L_b^3}{2c_r^2} \left[\frac{2\varepsilon^2(\Omega - 2\dot{\alpha})}{(1-\varepsilon^2)^2} + \frac{\pi(1+2\varepsilon^2)\dot{\varepsilon}}{(1-\varepsilon^2)^{5/2}} \right], \tag{3.14}$$

$$f_t = \frac{\mu R L_b^3}{2c_r^2} \left[\frac{\pi(\Omega - 2\dot{\alpha})\varepsilon}{2(1-\varepsilon^2)^{3/2}} + \frac{4\varepsilon\dot{\varepsilon}}{(1-\varepsilon^2)^2} \right]. \tag{3.15}$$

To express the hydrodynamic forces in the fixed reference frame, the following transformation can be applied,

$$\begin{Bmatrix} f_y \\ f_z \end{Bmatrix} = \begin{bmatrix} \sin\alpha & \cos\alpha \\ -\cos\alpha & \sin\alpha \end{bmatrix} \begin{Bmatrix} f_r \\ f_t \end{Bmatrix} \tag{3.16}$$

with,

$$\alpha = -\tan^{-1}\left(\frac{u_y}{u_z}\right). \tag{3.17}$$

Additionally, the hydrodynamic forces can be incorporated into the finite element model by using,

$$\mathbf{f_b}(\mathbf{x}, \dot{\mathbf{x}}, \Omega) = \sum_{i=1}^{n_b} \left(\mathbf{f_{by}}^i f_y^i(\mathbf{x_b}^i, \dot{\mathbf{x}}_\mathbf{b}^i, \Omega) + \mathbf{f_{bz}}^i f_z^i(\mathbf{x_b}^i, \dot{\mathbf{x}}_\mathbf{b}^i, \Omega) \right), \tag{3.18}$$

where n_b is the number of bearings, $\mathbf{f_{by}}$ and $\mathbf{f_{bz}} \in \mathbb{R}^N$ are Boolean vectors that define the nodes of the mesh in which the forces act, and $\mathbf{x_b}^i = \{u_y^i, u_z^i\}$ and $\dot{\mathbf{x}}_\mathbf{b}^i = \{\dot{u}_y^i, \dot{u}_z^i\}$ are the displacements and velocities at the ith bearing.

The stiffness and damping coefficients can be obtained by performing the differentiations indicated in Eq. (3.3), which can be done using any software for symbolic computation. In addition, the higher order terms $\mathbf{f_{nl}}(\mathbf{y}, \dot{\mathbf{y}})$ used in Eq. (3.6) are obtained from a Taylor expansion up to the third order and are given as,

$$\mathbf{f_{nl}}(\mathbf{y}, \dot{\mathbf{y}}, \Omega) = \sum_{i=1}^{n_b} \left(\mathbf{f_{by}}^i f_{nl,y}^i(\mathbf{y_b}^i, \dot{\mathbf{y}}_\mathbf{b}^i, \Omega) + \mathbf{f_{bz}}^i f_{nl,z}^i(\mathbf{y_b}^i, \dot{\mathbf{y}}_\mathbf{b}^i, \Omega) \right), \tag{3.19}$$

with

$$f_{nl,(y,z)}(\mathbf{y_b}, \dot{\mathbf{y}}_\mathbf{b}, \Omega) = \beta_{(y,z),(2000)} u_y^2 + \beta_{(y,z),(0200)} u_z^2 + \beta_{(y,z),(0020)} \dot{u}_y^2 + \beta_{(y,z),(0002)} \dot{u}_z^2 + \cdots$$
$$+ \beta_{(y,z),(3000)} u_y^3 + \beta_{(y,z),(0300)} u_z^3 + \beta_{(y,z),(0030)} \dot{u}_y^3 + \cdots = \sum_{i,j,k,l} \beta_{(y,z),(ijkl)} u_y^i u_z^j \dot{u}_y^k \dot{u}_z^l, \quad (3.20)$$

and,

$$\beta_{(y,z),(ijkl)} = \frac{\partial^i f_{(y,z)}}{\partial u_y^i} \frac{\partial^j f_{(y,z)}}{\partial u_z^j} \frac{\partial^k f_{(y,z)}}{\partial \dot{u}_y^k} \frac{\partial^l f_{(y,z)}}{\partial \dot{u}_y^l}. \quad (3.21)$$

Note that the displacements above are measured relative to the equilibrium position $\mathbf{x_e}$. In Miraskari et al. (2017b) one finds closed-form expressions for the linear and higher order coefficients $\beta_{(y,z),(ijkl)}$

3.3 Center manifold reduction

3.3.1 Autonomous system

This section presents the application of the parameterization method for invariant manifolds (HARO et al., 2016) to estimate the center manifold of the system and perform a CMR. Here, the unbalance force is neglected, $\mathbf{f_h} = \mathbf{0}$, making the system given by Eq. (3.6) autonomous. In addition, all the procedure is performed for a fixed speed Ω, thus the dependence of the hydrodynamic terms on Ω is omitted, thus $\mathbf{K_b}(\Omega) = \mathbf{K_b}$, $\mathbf{C_b}(\Omega) = \mathbf{C_b}$, and so on. This also means that this analysis must be performed at each speed Ω separately.

Firstly, the system needs to be recast in a first-order form, that is,

$$\dot{\mathbf{w}} = \mathbf{A}\mathbf{w} + \mathbf{g}(\mathbf{w}), \quad (3.22)$$

where,

$$\mathbf{A} = \begin{bmatrix} \mathbf{0} & \mathbf{I} \\ -\mathbf{M}^{-1}\mathbf{K} & -\mathbf{M}^{-1}\mathbf{D} \end{bmatrix}, \quad \mathbf{w} = \begin{Bmatrix} \mathbf{y}, & \dot{\mathbf{y}} \end{Bmatrix}^T, \quad \mathbf{g}(\mathbf{w}) = \begin{Bmatrix} \mathbf{0}, & \mathbf{M}^{-1}\mathbf{f_{nl}}(\mathbf{w}) \end{Bmatrix}^T. \quad (3.23)$$

Next, the vector $\mathbf{w}$ needs to be expanded in terms of the modes or eigenvectors of the matrix $\mathbf{A} \in \mathbb{R}^{2N \times 2N}$ as,

$$\mathbf{w} = \sum_{i=1}^{2N} \boldsymbol{\phi}^i q_i = [\boldsymbol{\phi}^1 \ \boldsymbol{\phi}^2 \ \cdots \ \boldsymbol{\phi}^{2N}]\mathbf{q} = \boldsymbol{\phi}\mathbf{q}, \quad (3.24)$$

$\boldsymbol{\phi} \in \mathbb{C}^{2N \times 2N}$ being the matrix with the eigenvectors at its columns, and $\mathbf{q} \in \mathbb{C}^{2N}$ the generalized coordinates. The columns of $\boldsymbol{\phi}$ are either complex conjugate or purely real,

so that the result (3.24) is also real. In rotor systems, the matrix $\mathbf{A}$ is in general not hermitian, and thus one needs to solve two eigenvalue problems, namely (LEE, 1993),

$$\begin{aligned} \mathbf{A}\boldsymbol{\phi}^i &= \lambda_i \boldsymbol{\phi}^i, \\ \mathbf{A}^H \boldsymbol{\psi}^i &= \lambda_i^* \boldsymbol{\psi}^i, \end{aligned} \tag{3.25}$$

in which $i \in \{1, \cdots, 2N\}$, λ_i are the eigenvalues, $\boldsymbol{\psi}^i$ the ith adjoint eigenvector, * denotes complex conjugation and H denotes the hermitian (complex conjugate) transpose. Both $\boldsymbol{\phi}^i$ and $\boldsymbol{\psi}^i$ can be normalized to satisfy,

$$\begin{aligned} (\boldsymbol{\psi}^j)^H \boldsymbol{\phi}^i &= \delta_{ij}, \\ (\boldsymbol{\psi}^j)^H \mathbf{A} \boldsymbol{\phi}^i &= \lambda_j \delta_{ij}, \end{aligned} \tag{3.26}$$

where δ_{ij} is the Kronecker delta and $i, j \in \{1, \cdots, 2N\}$. The conditions above are commonly referred to as biorthonormality conditions (LEE, 1993; MEIROVITCH, 1980). One may write Eq. (3.22) in its diagonal form by using the expansion (3.24), pre-multiplying the result by $\boldsymbol{\psi}^H$, and using the biorthonormality conditions, one arrives at,

$$\dot{\mathbf{q}} = \boldsymbol{\Lambda}\mathbf{q} + \boldsymbol{\psi}^H \mathbf{g}\big(\boldsymbol{\phi}\mathbf{q}\big), \tag{3.27}$$

where $\boldsymbol{\Lambda} = \text{diag}(\lambda_1, \cdots, \lambda_{2N})$. In the studied system, as the speed increases, the fluid-induced instability arises. This phenomenon is seen as the real part of an eigenvalue becoming positive, making the system unstable. Let $\mathbf{q_m} \in \mathbb{C}^2$ denote the coordinates of the mode that becomes unstable as $\Omega > \omega_{th}$, where ω_{th} is the instability threshold speed. The remaining coordinates are labeled $\mathbf{q_s} \in \mathbb{C}^{2N-2}$. In this way, Eq. (3.27) can be written as,

$$\dot{\mathbf{q}}_\mathbf{m} = \boldsymbol{\Lambda}_{\boldsymbol{m}} \mathbf{q}_\mathbf{m} + \boldsymbol{\psi}_{\boldsymbol{m}}{}^H \mathbf{g}(\mathbf{q}_\mathbf{m}, \mathbf{q}_\mathbf{s}), \tag{3.28a}$$

$$\dot{\mathbf{q}}_\mathbf{s} = \boldsymbol{\Lambda}_{\boldsymbol{s}} \mathbf{q}_\mathbf{s} + \boldsymbol{\psi}_{\boldsymbol{s}}{}^H \mathbf{g}(\mathbf{q}_\mathbf{m}, \mathbf{q}_\mathbf{s}), \tag{3.28b}$$

where $\boldsymbol{\Lambda}_{\boldsymbol{m}} = \text{diag}(\lambda_1, \lambda_2)$, with $\lambda_2 = \lambda_1^*$, and $\boldsymbol{\Lambda}_{\boldsymbol{s}} = \text{diag}(\lambda_3, \cdots, \lambda_{2N})$[2]. Note that Eqs. (3.28a) and (3.28b) are coupled due to the nonlinear term $\mathbf{g}(\mathbf{q})$. One could assume $\mathbf{q_s} = \mathbf{0}$ in (3.28a) and integrate the equation for $\mathbf{q_m}$. However, this, in addition to not giving the dynamics on the center manifold, may also lead to erroneous predictions such as spurious bifurcations (TROGER; STEINDL, 1991). The proper way to perform a CMR is by assuming $\mathbf{q_s} = \mathbf{h_s}(\mathbf{q_m})$, which will lead to,

$$\dot{\mathbf{q}}_\mathbf{m} = \boldsymbol{\Lambda}_{\boldsymbol{m}} \mathbf{q}_\mathbf{m} + \boldsymbol{\psi}_{\boldsymbol{m}}{}^H \mathbf{g}\big(\mathbf{q}_\mathbf{m}, \mathbf{h}_\mathbf{s}(\mathbf{q}_\mathbf{m})\big), \tag{3.29a}$$

$$\frac{\partial \mathbf{h_s}}{\partial \mathbf{q_m}} \dot{\mathbf{q}}_\mathbf{m} = \boldsymbol{\Lambda}_{\boldsymbol{s}} \mathbf{h}_\mathbf{s}(\mathbf{q}_\mathbf{m}) + \boldsymbol{\psi}_{\boldsymbol{s}}{}^H \mathbf{g}\big(\mathbf{q}_\mathbf{m}, \mathbf{h}_\mathbf{s}(\mathbf{q}_\mathbf{m})\big). \tag{3.29b}$$

[2]Note that this might require a reordering of matrices $\boldsymbol{\Lambda}$ and $\boldsymbol{\psi}$, depending on the rotor system

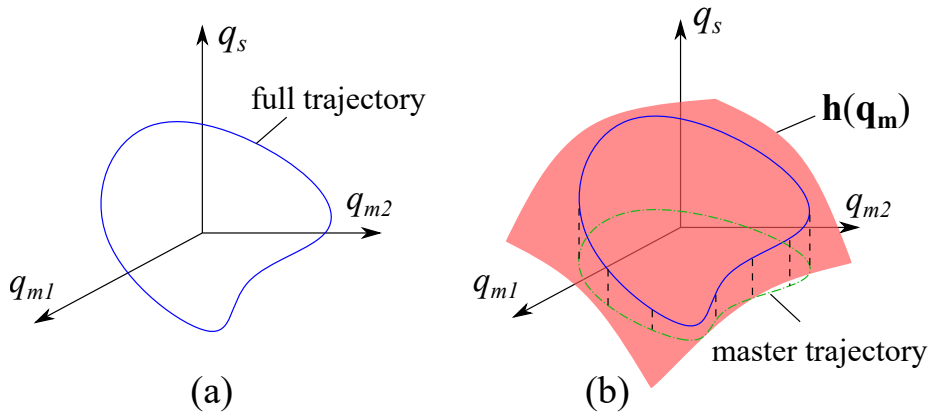

Figure 3.3: Depiction of the CMR: instead of obtaining the full trajectories by integrating all coordinates (a), in the CMR one only solves for the master coordinates and uses the geometry of the center manifold to obtain the full trajectory (b).

Where now, only Eq. (3.29a) needs to be integrated, and the coupling between the master and slave modes is given by the function $\mathbf{h_s}(\mathbf{q_m})$, which in turn is obtained from Eq. (3.29b). The function $\mathbf{h_s} : \mathbb{C}^2 \to \mathbb{C}^{2N-2}$ encodes the interaction between the modes and it is also what gives the geometry of the center manifold of the system. The difference between the problems given by Eqs. (3.28a)-(3.28b) and (3.29a)-(3.29b) is depicted in Fig. 3.3. In this first case, one needs to integrate for both $\mathbf{q_m}$ and $\mathbf{q_s}$ to obtain the response, whereas in the second case only the solution for $\mathbf{q_m}$ is needed, and the coupling between the two coordinates will be taken into account by the geometry of the manifold, given by $\mathbf{h}(\mathbf{q_m})$.

One can go further and simplify Eq. (3.29a) by only retaining the most relevant terms. This procedure is known as normal form transformation (WAGG, 2022). Let $\mathbf{p} \in \mathbb{C}^2$ denote the coordinates in normal form (also known as the parameterization coordinates), and $\mathbf{h_m} : \mathbb{C}^2 \to \mathbb{C}^2$ a map that transforms the master coordinates $\mathbf{q_m}$ in the normal coordinates $\mathbf{p}$, that is,

$$\mathbf{q_m} = \mathbf{h_m}(\mathbf{p}). \tag{3.30}$$

The dynamics of the system in normal form will be given as,

$$\dot{\mathbf{p}} = \mathbf{r}(\mathbf{p}), \tag{3.31}$$

in which $\mathbf{r} : \mathbb{C}^2 \to \mathbb{C}^2$ is a function that defines the reduced dynamics on the center manifold and it consists of a simplified form of the right-hand side of Eq. (3.29a). By substituting Eq. (3.30) into (3.29a), and using (3.31), one has

$$\frac{\partial \mathbf{h_m}}{\partial \mathbf{p}}\mathbf{r}(\mathbf{p}) = \boldsymbol{\Lambda_m}\mathbf{h_m}(\mathbf{p}) + \boldsymbol{\psi_m}{}^H\mathbf{g}\big(\mathbf{h_m}(\mathbf{p}), \mathbf{h_s}(\mathbf{p})\big), \tag{3.32}$$

where the map $\mathbf{h_s}$ is redefined as $\mathbf{h_s}(\mathbf{p}) = \mathbf{h_s}(\mathbf{h_m}(\mathbf{p}))$. Hence, Eq. (3.29b) becomes,

$$\frac{\partial \mathbf{h_s}}{\partial \mathbf{p}}\mathbf{r}(\mathbf{p}) = \boldsymbol{\Lambda_s}\mathbf{h_s}(\mathbf{p}) + \boldsymbol{\psi_s}^H \mathbf{g}\big(\mathbf{h_m}(\mathbf{p}), \mathbf{h_s}(\mathbf{p}))\big). \tag{3.33}$$

Equations (3.32) and (3.33) can be combined by making $\mathbf{h} = \{\mathbf{h_m},\ \mathbf{h_s}\}^T$, leading to,

$$\frac{\partial \mathbf{h}}{\partial \mathbf{p}}\mathbf{r}(\mathbf{p}) = \boldsymbol{\Lambda}\mathbf{h}(\mathbf{p}) + \mathbf{g}_1(\mathbf{p}), \tag{3.34}$$

where $\mathbf{g}_1 = \boldsymbol{\psi}^H \mathbf{g}\big(\mathbf{h}(\mathbf{p})\big)$. The problem now consists in finding $\mathbf{h}$ that maps the normal coordinates to the generalized coordinates, $\mathbf{q} = \mathbf{h}(\mathbf{p})$, and $\mathbf{r}$ that gives the equation of motion for the normal coordinates. Note that by obtaining $\mathbf{h}$ one not only performs a CMR, but is also able to simplify the equations of motion for the master modes $\mathbf{q_m}$ at the same time. This approach is known in the literature as the parameterization method (HARO et al., 2016).

Equation (3.34) is labeled as the invariance equation (HARO et al., 2016; PONSIOEN et al., 2020). This equation is a Partial Differential Equation (PDE), and it can be solved by any method aimed at this kind of problem (see Renson et al. (2016) for a review of the computation of invariant manifolds). In this work, the PDE is solved by expanding $\mathbf{h}$ and $\mathbf{r}$ into multivariate polynomials as,

$$h_i(\mathbf{p}) = H_{i,(1,0)}p_1 + H_{i,(0,1)}p_2 + H_{i,(1,1)}p_1p_2 + \cdots = \sum_{\mathbf{k}} H_{i,\mathbf{k}}\mathbf{p}^{\mathbf{k}}, \tag{3.35}$$

$$r_j(\mathbf{p}) = R_{j,(1,0)}p_1 + R_{j,(0,1)}p_2 + R_{j,(1,1)}p_1p_2 + \cdots = \sum_{\mathbf{k}} R_{j,\mathbf{k}}\mathbf{p}^{\mathbf{k}}, \tag{3.36}$$

in which $i \in \{1, \cdots, 2N\}$, $j \in \{1,\ 2\}$, $\mathbf{k} = (k_1,\ k_2) = \{(1,0),\ (0,1),\ (1,1), \cdots\}$ is a vector with the polynomial indices with $k_i \in \mathbb{N}$, and $\mathbf{p}^{\mathbf{k}} = p_1^{k_1}p_2^{k_2}$. This notation for representing multivariate polynomials is known as multi-index notation (PONSIOEN et al., 2020). The order of the multivariate polynomial is given by $|\mathbf{k}| = k_1 + k_2$, while the coefficients are included in the multi-dimensional complex arrays $\mathbf{H} = [H_{1,\mathbf{k}}, \cdots,\ H_{2N,\mathbf{k}}] \in \mathbb{C}^{2N\times P\times P}$ and $\mathbf{R} = [R_{1,\mathbf{k}},\ R_{2,\mathbf{k}}] \in \mathbb{C}^{2\times P\times P}$, being P the highest polynomial order.

By substituting Eqs. (3.35)-(3.36) into (3.34), one has,

$$\sum_{j=1}^{2}\left(\sum_{\mathbf{k}} k_j H_{i,\mathbf{k}}\mathbf{p}^{\mathbf{k}-\mathbf{e}_j}\right)\sum_{\mathbf{m}} R_{j,\mathbf{m}}\mathbf{p}^{\mathbf{m}} = \lambda_i \sum_{\mathbf{k}} H_{i,\mathbf{k}}\mathbf{p}^{\mathbf{k}} + g_{1i}(\mathbf{p}), \tag{3.37}$$

where $\mathbf{e}_j \in \mathbb{R}^2$ denotes a unit vector that has a one in its jth element and zeros elsewhere. One may obtain $H_{i,\mathbf{k}}$ and $R_{j,\mathbf{k}}$ by matching the order of the polynomials $|\mathbf{k}| = 1, 2, \cdots, P$ in Eq. (3.37). However, this system of equations is under-determined, because there are more unknowns than equations. One way to overcome this to obtain a unique solution

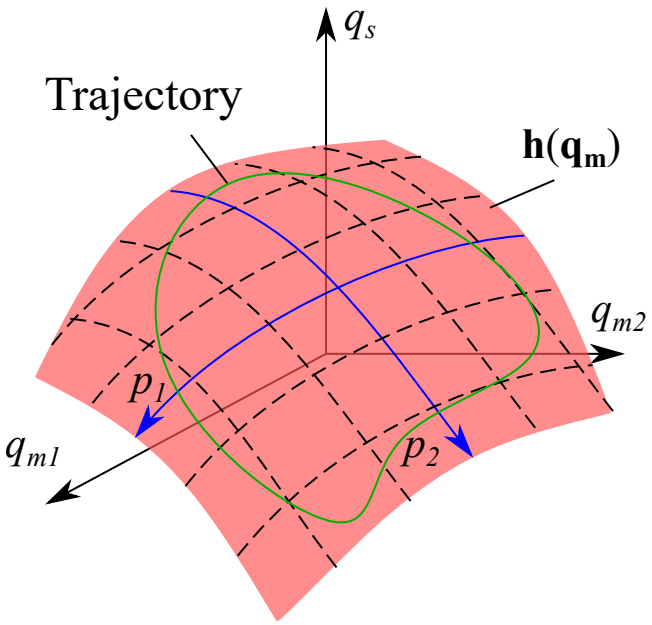

Figure 3.4: Depiction of the normal form style of parameterization of the invariant manifold: instead of using the master coordinates one uses the parameterization coordinates to obtain the dynamics on the manifold.

is to assume the terms in $R_{j,\mathbf{k}}$. The approach one uses in this assumption defines the so-called *style of parameterization* (HARO et al., 2016; JAIN; HALLER, 2022). Recall that $\mathbf{r}(\mathbf{p})$ comes from the right-hand side of Eq. (3.29a). Styles of parameterization refer to which terms are retained for the equation of motion of $\mathbf{p}$. When all terms are retained, one has the *graph style*, in which $\mathbf{r}(\mathbf{p})$ is the same as the right-hand side of Eq. (3.29a), thus $\mathbf{p} = \mathbf{q_m}$. This method might present problems when there is a fold in the invariant manifold (VIZZACCARO et al., 2022). On the other hand, in the *normal form style*, only terms that cause inner resonances are retained (which will become clear in the following). The normal form style is equivalent to performing a nonlinear change of coordinates to represent the invariant manifold (OPRENI et al., 2021), as depicted in Fig. 3.4. The normal form style is adopted in the following derivations.

At linear order, $|\mathbf{k}| = 1$, Eq. (3.37) gives,

$$H_{i,(1,0)}R_{1,(1,0)} + H_{i,(1,0)}R_{1,(0,1)} + H_{i,(0,1)}R_{2,(1,0)} + H_{i,(0,1)}R_{2,(0,1)} = \lambda_i \left(H_{i,(1,0)} + H_{i,(0,1)}\right). \tag{3.38}$$

In order to make the center manifold tangent to the linear eigenspace, $\mathbf{r}(\mathbf{p})$ has to match the right-hand side of Eq. (3.28a) at linear order, thus

$$R_{1,(1,0)} = \lambda_1, \quad R_{2,(0,1)} = \lambda_2, \quad R_{1,(0,1)} = R_{2,(1,0)} = 0, \tag{3.39}$$

or

$$R_{i,\mathbf{e}_j} = \lambda_j \delta_{ij}, \tag{3.40}$$

which in turn gives,

$$H_{i,\mathbf{e}_j} = \delta_{ij}. \tag{3.41}$$

Now, moving on to the case in which $|\mathbf{k}| > 1$. By performing the polynomial multiplication in the left-hand side of Eq. (3.37) one has,

$$\begin{aligned}\sum_{j=1}^{2}\sum_{\mathbf{k}}\sum_{\mathbf{m}} k_j H_{i,\mathbf{k}} R_{j,\mathbf{m}} \mathbf{p}^{\mathbf{k}-\mathbf{e}_j}\mathbf{p}^{\mathbf{m}} &= \sum_{j=1}^{2}\left(\sum_{\mathbf{k}} k_j H_{i,\mathbf{k}} R_{j,\mathbf{e}_j}\mathbf{p}^{\mathbf{k}} + \sum_{\mathbf{m}} H_{i,\mathbf{e}_j} R_{j,\mathbf{m}}\mathbf{p}^{\mathbf{m}}\right) \\ &\quad + \sum_{j=1}^{2}\sum_{|\mathbf{k}|>1}\sum_{|\mathbf{m}|>1} k_j H_{i,\mathbf{k}} R_{j,\mathbf{m}}\mathbf{p}^{\mathbf{k}-\mathbf{e}_j}\mathbf{p}^{\mathbf{m}} \\ &= \sum_{j=1}^{2}\left(\sum_{\mathbf{k}} k_j \lambda_j H_{i,\mathbf{k}}\mathbf{p}^{\mathbf{k}} + \sum_{\mathbf{m}} \delta_{ij} R_{j,\mathbf{m}}\mathbf{p}^{\mathbf{m}} + \sum_{\mathbf{n}=\mathbf{k}+\mathbf{m}}\left(\sum_{\mathbf{k}\leq\mathbf{n}+\mathbf{e}_j} k_j H_{i,\mathbf{k}} R_{j,\mathbf{n}+\mathbf{e}_j-\mathbf{k}}\right)\mathbf{p}^{\mathbf{n}}\right).\end{aligned} \tag{3.42}$$

Additionally, the nonlinear force can be expressed as,

$$g_{1i}(\mathbf{p}) = G_{i,\mathbf{k}}\mathbf{p}^{\mathbf{k}}. \tag{3.43}$$

Substituting Eqs. (3.42) and (3.43) into (3.37), and matching the polynomial orders $|\mathbf{k}| = 2, 3, \cdots, P$, one has,

$$\left(\lambda_i - \sum_{j=1}^{2} k_j\lambda_j\right) H_{i,\mathbf{k}} = \sum_{j=1}^{2}\left(\delta_{ij} R_{j,\mathbf{k}} + \sum_{\mathbf{m}\leq\tilde{\mathbf{k}}_j} m_j H_{i,\mathbf{m}} R_{j,\tilde{\mathbf{k}}_j-\mathbf{m}}\right) + G_{i,\mathbf{k}}, \tag{3.44}$$

where $\tilde{\mathbf{k}}_j = \mathbf{k} + \mathbf{e}_j$. Equation (3.44) can be readily solved for $H_{i,\mathbf{k}}$, leading to,

$$H_{i,\mathbf{k}} = \frac{\sum_{j=1}^{2}\delta_{ij}R_{j,\mathbf{k}} + Q_{i,\mathbf{k}}}{\lambda_i - \sum_{j=1}^{2} k_j\lambda_j}, \tag{3.45}$$

being $Q_{i,\mathbf{k}}$ defined from Eq. (3.44). One may note that in case $\lambda_i - \sum_{j=1}^{2} k_j\lambda_j \approx 0$, the coefficients $H_{i,\mathbf{k}}$ may have large or undefined values. This can affect the convergence of the Taylor series approximation of the center manifold (PONSIOEN et al., 2020). Since the present system displays a Hopf bifurcation at the instability speed $\Omega = \omega_{th}$, the following conditions hold (WIGGINS, 2003):

$$\lambda_{1,2} - (k_1\lambda_{1,2} + k_2\lambda_{1,2}^*) = 0, \tag{3.46}$$

when k_1 and k_2 are odd. Therefore, $H_{i,\mathbf{k}}$ has undefined values when $\mathbf{k}' = \{\mathbf{k} \mid |\mathbf{k}| = 3, 5, 7, \dots\}$. In order to overcome this problem, one assumes the values in $R_{j,\mathbf{k}}$ to set the left-hand side of Eq. (3.45) zero. In this way, both $H_{i,\mathbf{k}}$ and $R_{j,\mathbf{k}}$ are obtained at the

same time, giving the geometry of and dynamics on the center manifold, respectively. To remove the terms that cause resonance, one may perform,

$$R_{1,\mathbf{k}'} = -Q_{1,\mathbf{k}'}, \quad R_{2,\mathbf{k}'} = -Q_{2,\mathbf{k}'}, \tag{3.47}$$

$\mathbf{k}' = (k_1',\ k_2')$ being the set of orders that satisfy Eq. (3.46). By applying (3.47), one transforms Eq. (3.31) into the well known Hopf normal form,

$$\dot{p}_1 = r_1(p_1, p_2) = \lambda_1 p_1 + R_{1,(2,1)} p_1^2 p_2 + R_{1,(3,2)} p_1^3 p_2^2 + \mathcal{O}(|\mathbf{p}|^7), \tag{3.48a}$$

$$\dot{p}_2 = r_2(p_1, p_2) = \lambda_2 p_2 + R_{2,(1,2)} p_2^2 p_1 + R_{2,(2,3)} p_2^3 p_1^2 + \mathcal{O}(|\mathbf{p}|^7), \tag{3.48b}$$

which is a set of complex differential equations for $\mathbf{p} = \{p_1,\ p_2\}$. One can recast the above equations in polar coordinates by making $p_1 = ae^{\mathrm{i}\theta}$ and $p_2 = ae^{-\mathrm{i}\theta}$, with $a \in \mathbb{R}$ and $\mathrm{i} = \sqrt{-1}$, and then separating the real and imaginary parts, leading to,

$$\dot{a} = b_1 a + c_1 a^3 + d_1 a^5 + \mathcal{O}(a^7), \tag{3.49a}$$

$$\dot{\theta} = b_2 + c_2 a^2 + d_2 a^4 + \mathcal{O}(a^6), \tag{3.49b}$$

in which $b_1 = \mathrm{Re}[\lambda_1]$, $b_2 = \mathrm{Im}[\lambda_1]$, $c_1 = \mathrm{Re}[R_{1,(2,1)}]$, $c_2 = \mathrm{Im}[R_{1,(2,1)}]$, $d_1 = \mathrm{Re}[R_{1,(3,2)}]$ and $d_2 = \mathrm{Im}[R_{1,(3,2)}]$. Either Eq. (3.49) or (3.48) may be used to obtain the dynamics of the system in the parameterization coordinates $\mathbf{p}$.

The steady-state amplitudes of motions can be computed directly from Eq. (3.49a) by making $\dot{a} = 0$ and solving for a. Substituting this value in Eq. (3.49b) gives the frequency of the motion $\dot{\theta}$. Near the Hopf bifurcation, in addition to the equilibrium solution $a = 0$, the system will display another solution, namely $a = a^*$, which represents the emerging limit cycle. Therefore, no numerical integration is required, only the solution of a polynomial equation (3.49a). The stability of the cycles can be assessed by the sign of c_1 (WIGGINS, 2003). Sub-critical bifurcations occur for $c_1 < 0$, where unstable cycles emerge prior to the bifurcating point (hence the prefix "sub") and super-critical when $c_1 > 0$, where the cycles emerge after the bifurcation (hence the prefix "super"). After the dynamics in the parameterization coordinates is obtained, one can use the map $\mathbf{h}(\mathbf{p})$ to obtain the response in terms of the generalized coordinates $\mathbf{q}$. The physical coordinates are obtained from the modal expansion, Equation (3.24). This process is illustrated in Fig. 3.5. Note that the rotor model may possess a large number of DOFs, and yet its response can be obtained by only the dynamics on the center manifold. This is the greatest advantage of the CMR method, and makes it a feasible tool for the analysis and design of real rotating machinery.

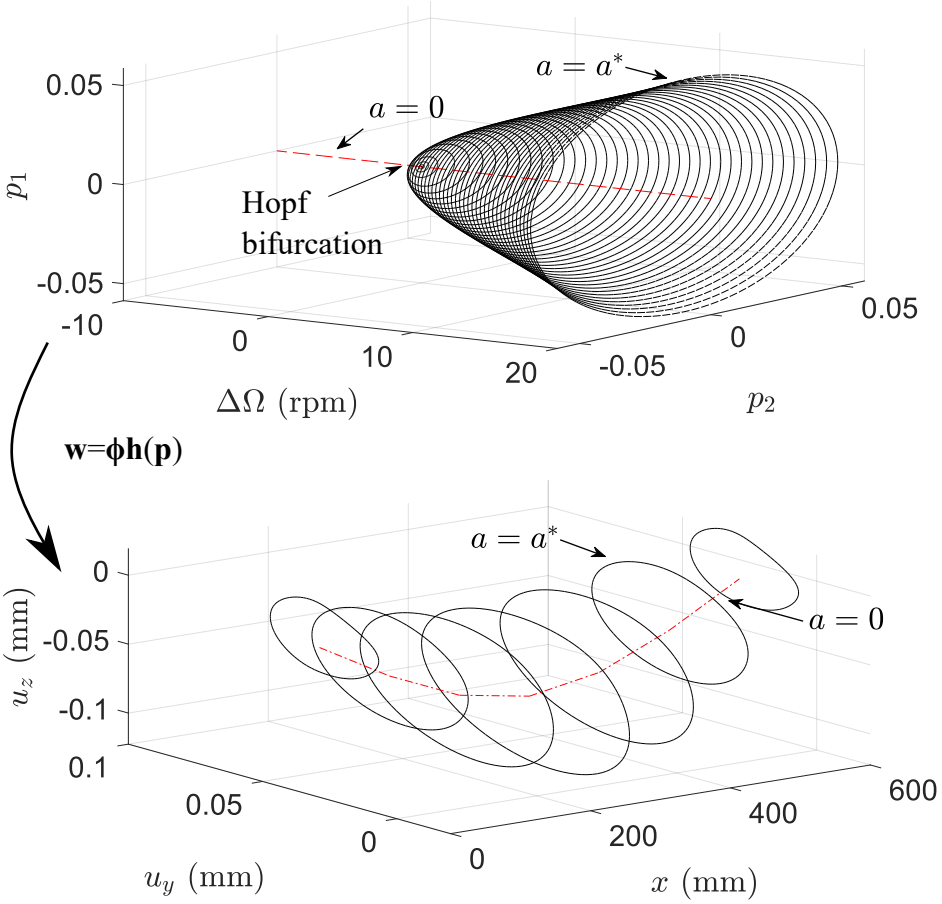

Figure 3.5: Summarizing the CMR method: one can obtain the limit cycles ($a = a^*$) and equilibrium ($a = 0$) solutions from the reduced dynamics (top), and then use the transformation $\mathbf{w} = \boldsymbol{\phi}\mathbf{h}(\mathbf{p})$ to obtain the response in physical coordinates (bottom). No numerical integration is required.

3.3.2 Non-autonomous system

The approach presented in the previous section is only valid for a perfectly balanced rotor. However, the CMR can be extended to the non-autonomous case by simple adjustments in the equations of motion. The approach developed here differs from (PONSIOEN et al., 2020) in that the non-autonomous term is not treated as a perturbation of the autonomous manifolds. Instead, the system is augmented considering the excitation as state variables, and in cartesian form. This approach allows the external force to be fairly strong and avoids the small force assumptions in (PONSIOEN et al., 2020). In addition, similar to the previous case, the analysis is performed for a fixed Ω, thus any dependence on this parameter is omitted.

Let $u = \cos\Omega t$ and $v = \sin\Omega t$, which are now considered as state variables for the system. Equation (3.6) can now be rewritten as,

$$\mathbf{M}\ddot{\mathbf{y}} + \mathbf{D}\dot{\mathbf{y}} + \mathbf{K}\mathbf{y} = \mathbf{f}_{\mathbf{nl}}(\mathbf{y}, \dot{\mathbf{y}}) + \mathbf{f}_{\mathbf{hy}} m_{un}\Omega^2 u + \mathbf{f}_{\mathbf{hz}} m_{un}\Omega^2 v \tag{3.50a}$$

$$\dot{u} = -\Omega v \tag{3.50b}$$

$$\dot{v} = \Omega u \tag{3.50c}$$

where Eq. (3.2) was employed. Note that Eq. (3.50) is now independent of time, and hence autonomous. This equation can be recast in the same form as Eq. (3.22), with the following matrices and vectors,

$$\begin{aligned} \mathbf{A} &= \begin{bmatrix} \mathbf{0}_{N\times N} & \mathbf{I}_{N\times N} & \mathbf{0}_N & \mathbf{0}_N \\ -\mathbf{M}^{-1}\mathbf{K} & -\mathbf{M}^{-1}\mathbf{D} & \mathbf{M}^{-1}\mathbf{f_{hy}} m_u \varepsilon \Omega^2 & \mathbf{M}^{-1}\mathbf{f_{hz}} m_u \varepsilon \Omega^2 \\ \mathbf{0}_{N\times N} & \mathbf{0}_{N\times N} & 0 & -\Omega \\ \mathbf{0}_{N\times N} & \mathbf{0}_{N\times N} & \Omega & 0 \end{bmatrix}, \\ \mathbf{w} &= \Big\{ \mathbf{y}, \quad \dot{\mathbf{y}}, \quad u, \quad v \Big\}^T, \quad \mathbf{g}(\mathbf{w}) = \Big\{ \mathbf{0}_N, \quad \mathbf{M}^{-1}\mathbf{f_{nl}}(\mathbf{w}), \quad 0, \quad 0 \Big\}^T \end{aligned} \tag{3.51}$$

From this point onwards, the application of the CMR is now very similar to what was shown in the previous section. One may expand the state vector $\mathbf{w}$ in terms of the eigenvetors of the matrix $\mathbf{A} \in \mathbb{R}^{(2N+2)\times(2N+2)}$, and write the dynamical system in its diagonal form (Equation (3.27)). Due to the augmented system, one pair of eigenvalues of $\mathbf{A}$ will be purely imaginary, with the imaginary part corresponding to the speed Ω, which is a fictitious mode and it does not correspond to any vibrating mode of the rotor.

The master coordinates will consist of the mode that becomes unstable and the fictitious mode due to unbalance. Hence $\mathbf{q_m} \in \mathbb{C}^M$, with $M = 4$, while $\mathbf{q_s} \in \mathbb{C}^{N_s}$, with $N_s = 2N+2-M$. Therefore, the reduced dynamics will be $\mathbf{r} : \mathbb{C}^M \to \mathbb{C}^M$ and the normal coordinates $\mathbf{p} \in \mathbb{C}^M$. The map $\mathbf{h}(\mathbf{p})$ can still be found by Eq. (3.34). The multivariate polynomials are now given as,

$$\begin{aligned} h_i(\mathbf{p}) = H_{i,(1,0,0,0)}p_1 + H_{i,(0,1,0,0)}p_2 + H_{i,(1,1,0,0)}p_1p_2 \\ + H_{i,(0,0,1,0)}p_3 + H_{i,(0,0,0,1)}p_4 + \cdots = \sum_{\mathbf{k}} H_{i,\mathbf{k}}\mathbf{p}^{\mathbf{k}}, \end{aligned} \tag{3.52}$$

$$r_j(\mathbf{p}) = R_{j,(1,0,0,0)}p_1 + R_{j,(0,1,0,0)}p_2 + \cdots = \sum_{\mathbf{k}} R_{j,\mathbf{k}}\mathbf{p}^{\mathbf{k}}, \tag{3.53}$$

in which $i \in \{1, \cdots, 2N+2\}$, $j \in \{1, \cdots, M\}$ and $\mathbf{k} = (k_1, k_2, k_3, k_4) = \{(1,0,0,0), \cdots\}$. The polynomial coefficients are contained in $\mathbf{H} = [H_{1,\mathbf{k}}, \cdots, H_{2N+2,\mathbf{k}}] \in \mathbb{C}^{2N\times P\times P\times P\times P}$ and $\mathbf{R} = [R_{1,\mathbf{k}}, \cdots, R_{M,\mathbf{k}}] \in \mathbb{C}^{M\times P\times P\times P\times P}$, being P the highest polynomial order. Note that these arrays can become very large, depending on the order P, which might require a high usage of memory in the numerical implementation. However, these arrays are sparse and can be efficiently stored by keeping the nonzero terms only, as explained by Ponsioen et al. (2020).

The solution of Eq. (3.34) is obtained by substituting the polynomials expansions

(3.52)-(3.53), and equating the orders $|\mathbf{k}| = 1, 2, \cdots, P$, exactly as shown in the previous section. The higher order coefficients will be obtained from,

$$H_{i,\mathbf{k}} = \frac{\sum_{j=1}^{M} \delta_{ij} R_{j,\mathbf{k}} + Q_{i,\mathbf{k}}}{\lambda_i - \sum_{j=1}^{M} k_j \lambda_j}, \tag{3.54}$$

and the terms that enter into the reduced dynamics $\mathbf{r}(\mathbf{p})$ are the ones that make the numerator in Eq. (3.54) zero, that is, $\lambda_i - \sum_{j=1}^{M} k_j \lambda_j \approx 0$. From the previous section, due to the Hopf bifurcation, one has, $\lambda_{1,2} - (k_1\lambda_1 + k_2\lambda_1^*) = 0$, with $k_1 + k_2$ odd and $k_3 = k_4 = 0$. In addition to these terms, whenever $k_3 = k_4$, there is also internal resonance, because,

$$\begin{aligned} \lambda_i - \sum_{j=1}^{M} k_j \lambda_j &= \lambda_i - k_1\lambda_1 - k_2\lambda_2 - k_3\lambda_3 - k_4\lambda_4 \\ &= \lambda_i - k_1\lambda_1 - k_2\lambda_2 - k_3 \mathrm{i}\Omega - k_3(-\mathrm{i}\Omega) = \lambda_i - k_1\lambda_1 - k_2\lambda_2. \end{aligned} \tag{3.55}$$

Therefore, when $i \in \{1, 2\}$, the following polynomial terms will be problematic,

$$\mathbf{k}' = (k_1, k_2, k_3, k_4) = \{\mathbf{k} \mid k_3 = k_4, \;\; k_1 + k_2 = 1, 3, 5, 7, \dots\}. \tag{3.56}$$

These terms are removed from Eq. (3.54) by means of Eq. (3.47). The reduced dynamics then becomes,

$$\dot{p}_1 = \lambda_1 p_1 + R_{1,(1,0,1,1)} p_1 p_3 p_4 + R_{1,(2,1,0,0)} p_1^2 p_2 + R_{1,(2,1,1,1)} p_1^2 p_2 p_3 p_4 + \mathcal{O}(|\mathbf{p}|^5), \tag{3.57a}$$

$$\dot{p}_2 = \lambda_2 p_2 + R_{2,(0,1,1,1)} p_2 p_3 p_4 + R_{2,(1,2,0,0)} p_2^2 p_1 + R_{2,(1,2,1,1)} p_2^2 p_1 p_3 p_4 + \mathcal{O}(|\mathbf{p}|^5), \tag{3.57b}$$

$$\dot{p}_3 = \mathrm{i}\Omega p_3, \tag{3.57c}$$

$$\dot{p}_4 = -\mathrm{i}\Omega p_4. \tag{3.57d}$$

Equations (3.57c)-(3.57d) can be readily solved as $p_3 = p_0 e^{\mathrm{i}\Omega}$ and $p_4 = p_0^* e^{-\mathrm{i}\Omega}$, where $p_0 \in \mathbb{C}$ is the initial condition. Substituting these solutions in Eqs. (3.57a)-(3.57b) leads to,

$$\begin{aligned} \dot{p}_1 = &\left(\lambda_1 + |p_0|^2 + |p_0|^4 + |p_0|^6 + \cdots\right) p_1 \\ &+ \left(R_{1,(2,1,0,0)} + R_{1,(2,1,1,1)}|p_0|^2 + R_{1,(2,1,2,2)}|p_0|^4 + \cdots\right) p_1^2 p_2 \\ &+ \left(R_{1,(3,2,0,0)} + R_{1,(3,2,1,1)}|p_0|^2 + R_{1,(3,2,2,2)}|p_0|^4 + \cdots\right) p_1^3 p_2^2 + \mathcal{O}(|\mathbf{p}|^7), \end{aligned} \tag{3.58a}$$

$$\begin{aligned} \dot{p}_2 = &\left(\lambda_2 + |p_0|^2 + |p_0|^4 + |p_0|^6 + \cdots\right) p_2 \\ &+ \left(R_{2,(2,1,0,0)} + R_{2,(2,1,1,1)}|p_0|^2 + R_{2,(2,1,2,2)}|p_0|^4 + \cdots\right) p_1 p_2^2 \\ &+ \left(R_{2,(3,2,0,0)} + R_{1,(3,2,1,1)}|p_0|^2 + R_{2,(3,2,2,2)}|p_0|^4 + \cdots\right) p_1^2 p_2^3 + \mathcal{O}(|\mathbf{p}|^7), \end{aligned} \tag{3.58b}$$

which is very similar to the autonomous case, Equation (3.48), except with some additional terms due to the non-autonomous forcing. Note that the non-autonomous terms affect the cubic coefficients $p_1 p_2^2$, and hence the type of Hopf bifurcation (See discussion at the end of the previous section). This was shown in the studies performed by Rendl et al. (2023).

The initial condition p_0 is obtained in the following way. Firstly, note that $u = \cos\Omega t$ and $v = \sin\Omega t$, by definition. Thus, the initial conditions for u and v are $u_0 = 1$ and $v_0 = 0$. Secondly, the initial condition for the generalized coordinates is obtained as,

$$\mathbf{q}_0 = \boldsymbol{\psi}^T \mathbf{w}_0 = \boldsymbol{\psi}^T \begin{bmatrix} \mathbf{y}_0 \\ \dot{\mathbf{y}}_0 \\ u_0 \\ v_0 \end{bmatrix}, \tag{3.59}$$

where $\mathbf{y}_0$ and $\dot{\mathbf{y}}_0$ are the initial displacements and velocities. Assuming $\mathbf{y}_0 = \dot{\mathbf{y}}_0 = \mathbf{0}$, one has

$$\mathbf{q}_0 = \boldsymbol{\psi}^T \begin{bmatrix} \mathbf{0}_N \\ \mathbf{0}_N \\ 1 \\ 0 \end{bmatrix} = \boldsymbol{\psi}_u \tag{3.60}$$

where $\boldsymbol{\psi}_u$ is the column of $\boldsymbol{\psi}^T$ corresponding to the state variable u. Therefore, the initial condition will be,

$$p_0 = \psi_u^k \tag{3.61}$$

being ψ_u^k the kth element of the vector $\boldsymbol{\psi}_u$ that correspond to the forcing mode. For an initial condition with a nonzero phase, the same straightforward procedure can be followed, but then $(u_0, v_0) \in [0, 1]$.

4 EXPERIMENTAL TEST RIG

The test rig used for the experiments is located at the Faculty of Mechanical Engineering of the University of Campinas (Unicamp). It is one of the test rigs belonging to the Laboratory of Rotating Machines (*Laboratório de Máquinas Rotativas* - LAMAR in Portuguese). The rig consists of a steel plate with dimensions $1170 \times 280 \times 30$ mm, mounted on top of a large concrete block, which in turn is supported by springs and a layer of foam on another concrete block. The plate has a large number of holes that allow the positioning of bearing pedestals in different configurations.

Figure 4.1 shows the two configurations, with one and two disks, used in this work. A detailed indication of the components and sensors is provided by Fig. 4.2. The instrumentation consists of sensors to measure the displacements of the rotor inside the bearings and at the disks and acceleration of the bearing supports. Temperature of the lubricating oil (ISO VG 32) is measured at the oil reservoir and bearing housing. Also, an optic sensor (PHCT 203) provides speed measurements and it is used as a trigger mechanism to ensure all measurements start at the same phase (Figure 4.3). Table 4.1 gives a detailed description of the sensors used.

Figure 4.4 shows the oil feeding system of the test rig. The pump is of the diaphragm type and has a variable injection pressure in the 40-60 kPa range. Oil is pumped from the reservoir to an oil filter, it passes through an air trap to remove any air contained in the lubricant, and then it is sent to the bearings through a "T" connection, as shown

Table 4.1: List of sensors used in the experiments.

Description	Model	Sensitivity	Range
Displacements of disks	Turk Bi5-M18-LU	5.3 V @ 1 mm	2 mm
Displacements of journal	Bently Nevada	1 V @ 10 mils	1.5 mm
Reaction forces of bearing casing	Honeywell Model 102	2.5 mV/V	100 kg
Acceleration of bearing casing	DeltaTron Type 4534-B	1 mV/ms^{-2}	7000 ms^{-2}

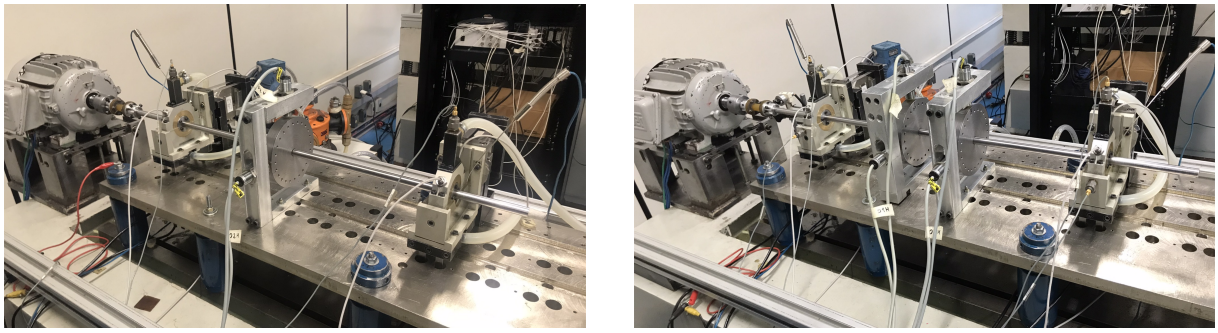

(a) (b)

Figure 4.1: Experimental test rig: configuration with one disk (a) and two disks (b).

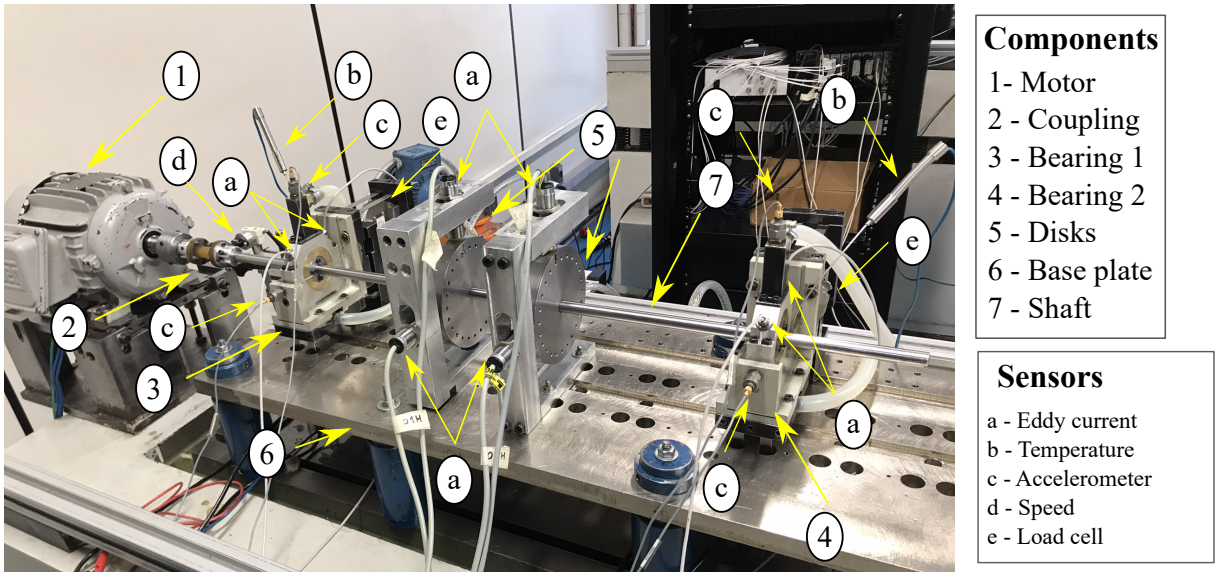

Figure 4.2: Experimental test rig: components and sensors.

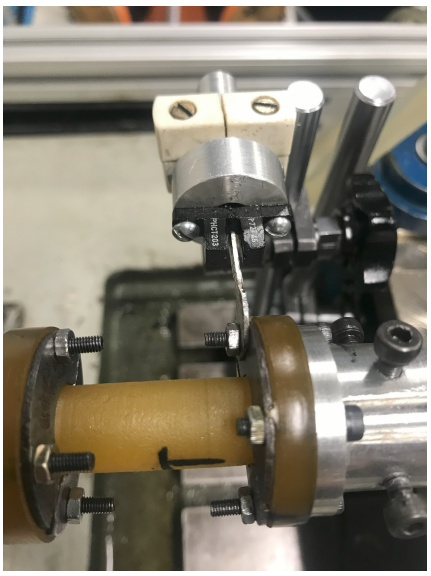

Figure 4.3: Trigger mechanism: an optic sensor detects the passage of a small metal plate to start the measurements.

in the figure. In addition, the oil flowing out from the bearings goes directly back to the reservoir.

The bearing pedestals are mounted on two four-bar mechanisms developed by Dedini (1993), and consist of four thin beams in each direction. The difference of the beams stiffness allows the horizontal and vertical reaction forces to be independently measured through a load cell, as shown in Fig. 4.5. However, it is worth mentioning that this assembly makes the pedestals flexible. As shown in Nonato (2013), the natural frequencies of the pedestals are 68.5 Hz, 149.0 Hz and 223.0 Hz. In the present work, the maximum rotor speed considered was 60 Hz, thus not in the range of the frequencies.

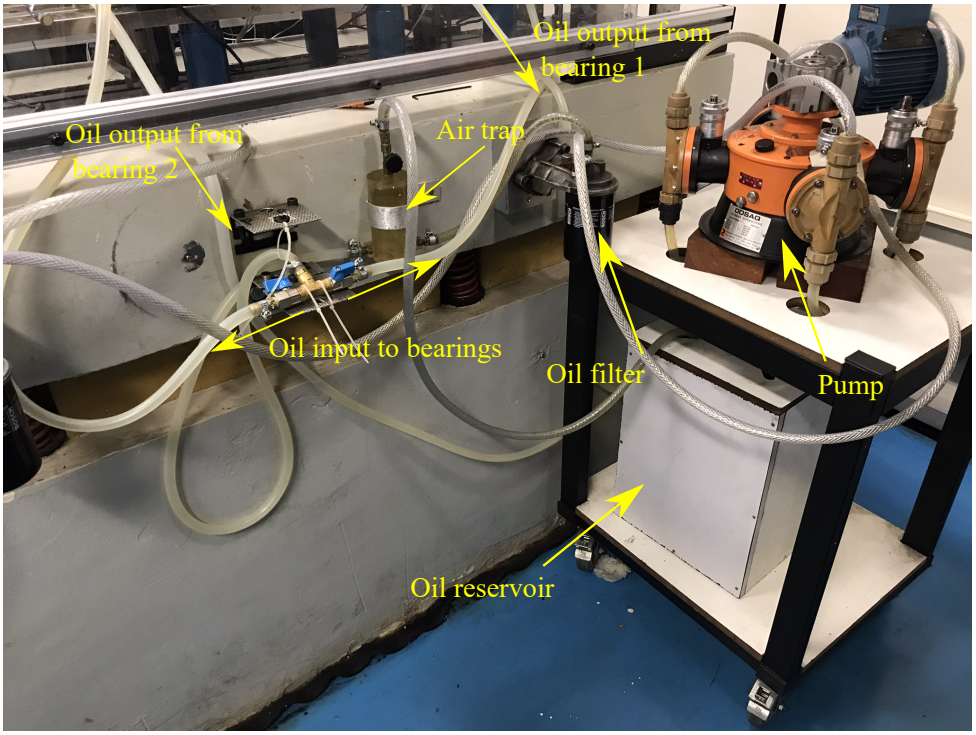

Figure 4.4: Oil feeding system.

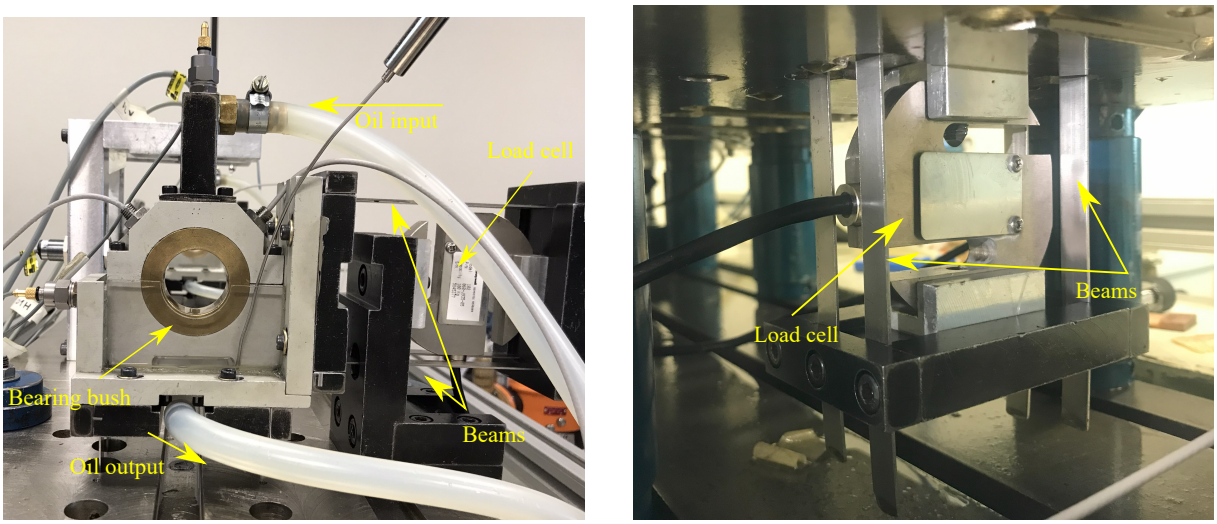

(a) (b)

Figure 4.5: Bearing pedestal: front view (a) and bottom load cell (b).

The bearing casing is made of aluminium, while the bush is made of bronze and has three holes, one for the oil input and two for inserting displacement sensors. The displacements are measured at a 45° angle between the vertical axis, and a rotation transformation needs to be performed to obtain the vertical and horizontal components.

The shaft is made of AISI 1055 steel and has a diameter of 12 mm and a length of 800 mm. It is placed between two bearing pedestals, which are positioned 530 mm apart from each other. The disks are made of SAE 1020 steel with 120 mm of diameters and 20

mm of thickness. In the configuration with one disk, it is placed at the midspan between the bearings. In the configuration with two disks, they were placed symmetrically along the shaft, and their distance between each other was varied throughout the studies.

The motor that drives the system is a 3 CV WEG AC motor, and it is connected to the shaft through a flexible coupling, which can be seen in Fig. 4.3. To control the motor speed, a WEG CFW-08 frequency inverter is used, which is connected to a PC by means of a serial port. The signal is acquired through a National Instruments board, model USB-9162. However, before entering the board, the signals from the displacement and accelerometers pass through signal conditioners. In the case of the displacement sensors, the conditioners consist of an amplifier (only for the Bentley sensors), and low-pass, with a 1 kHz cut-off, and DC filters. For the accelerometers, the signal conditioner Type 2694 from Brüel & Kjær is used. Despite the availability of this sensing equipment, in the present work only the displacement sensors were used, due to the nature of the current study.

5 NUMERICAL STUDY

This chapter presents the validation of the CMR approach deduced in Chapter 3. The validation is divided into the autonomous, Section 5.1, and non-autonomous, Section 5.2, approaches.

5.1 Autonomous system

The following text was first published in "Nonlinear Dynamics, 111, 17749–17767, 2023" and it is reproduced with permission from Springer Nature.

This section presents the application of the CMR to obtain stable and unstable limit cycles. The effectiveness of the method will be assessed through a comparison of its results with those obtained using the open-source software MATCONT (DHOOGE et al., 2003), which is a numerical continuation package based in MATLAB^{TM}. MATCONT utilizes a modified pseudo-arclength continuation. It can be used to continue equilibria and limit cycles and to detect a wide range of bifurcations (DHOOGE et al., 2003). This software has been used by other authors to study bifurcations in rotors with fluid-film bearings before, e.g., (CHOUCHANE; AMAMOU, 2011; AMAMOU, 2022; BOYACI, 2016; ANASTASOPOULOS; CHASALEVRIS, 2022). In the MATCONT solutions, the full bearing force given by Eq. (3.16) is used, that is, with no polynomial approximation as in the CMR method. Therefore, this approach not only evaluates the CMR ability to detect bifurcations, but also the suitability of the polynomial approximation to represent the fluid-film bearing force. The default options in MATCONT were used in all continuation runs performed.

The CMR will be evaluated in two systems: a simple and a realistic rotor. In the following studies, the polynomial expansions in Eqs. (3.35)-(3.36) were considered up to the fifth order, except when indicated otherwise. In addition, the main purpose of this section is to evaluate and compare the predictions given by the proposed method with an established software, thus the parametric studies will be limited. However, extensive studies have already been performed in this sense, where various factors that affect the bifurcations in rotors with fluid bearings were studied, and the reader is referred to (WANG; KHONSARI, 2006b; CHASALEVRIS, 2020; KANO et al., 2019; CHOUCHANE; AMAMOU, 2011; MIURA et al., 2017).

5.1.1 Simple rotor system

Figure 5.1 shows the geometry and mesh of the studied system. This rotor system is based on an experimental test rig (MACHADO et al., 2018). It consists of a shaft,

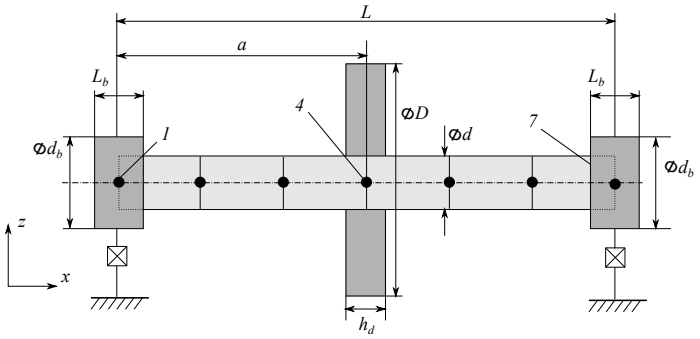

Figure 5.1: Geometry and mesh of the simple rotor system studied.

Table 5.1: Reference values for the parameters used in the simulations for the simple rotor system.

Parameter	Value
Shaft length (L)	600 mm
Shaft diameter (d)	24 mm
Disk diameter (D)	90 mm
Disk thickness (h_d)	47 mm
Disk position (a)	300 mm
Young's modulus (E)	207 GPa
Poisson's ratio (ν)	0.3
Density of the material (ρ)	7850 kg·m^3
Bearing length (L_b)	20 mm
Bearing diameter (d_b)	31 mm
Fluid	ISO VG 32
Fluid viscosity (μ)	0.028 Pa·s (at 40 °C)
Fluid density (ρ_f)	870 kg·m^3
Radial clearance (c_r)	90 μm

discretized into 6 finite elements, with a disk and two identical fluid-film bearings. The disk and journal are considered rigid masses (with rotary and polar inertia), and they are placed at nodes 1, 4, and 7. The nonlinear forces are introduced at the center of the bearings, nodes 1 and 7. The parameters used are listed in Tab. 5.1. Some of these parameters will be varied in the following study, and if nothing is mentioned, the assumed values are the ones in the table.

Figure 5.2 shows the limit cycles originated after the instability threshold for different length-to-diameter ratios (L_b/d_b) of the bearings. The ratio is varied by fixing the diameter at $d_b = 31$ mm, and varying the bearing length L_b. In the figures, $\Delta\Omega = \Omega - \omega_w$, where ω_w is the instability speed, which is also shown. The system starts at equilibrium and at $\Delta\Omega = 0$, one has the creation of limit cycles (Hopf bifurcation). The top row figures show the maximum and minimum displacements of the cycles normalized by the radial clearance c_r, while the bottom row shows the orbits at the demarcated line A–A. For $L_b/d_b = 0.4$, one gets a super-critical bifurcation with stable limit cycles extending as far as 175 rpm from the instability point (Figure 5.2a). Although the amplitudes of these limit cycles reach a fairly high value, it still is a safe operating speed. The CMR

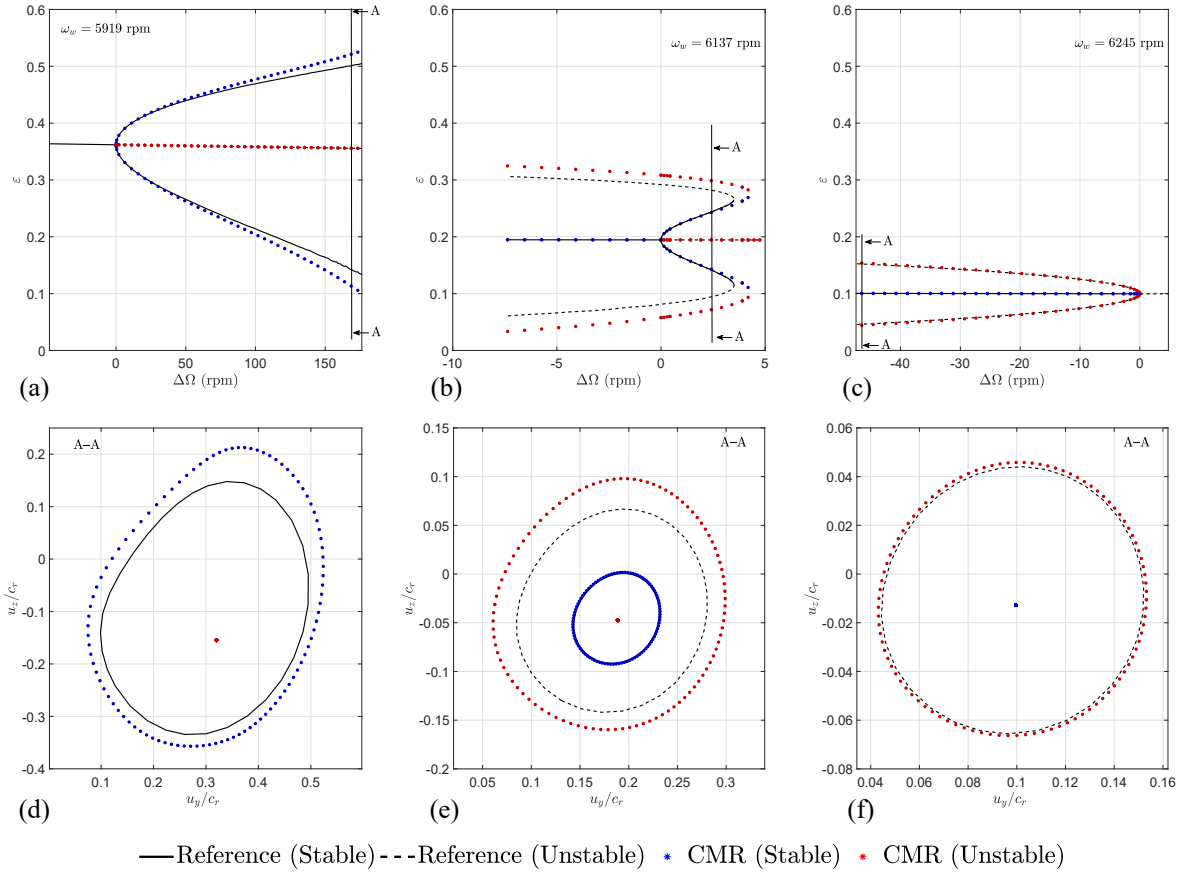

Figure 5.2: Effect of L_b/d_b ratio on the limit cycles near the instability speed at bearing 1: $L_b/d_b = 0.4$ (a-d), $L_b/d_b = 0.5$ (b-e) and $L_b/d_b = 0.65$ (c-f).

shows a good agreement with the numerical results obtained with MATCONT (which are labeled as reference in the figures), as one notes from the radial displacements and orbits (Figures 5.2a-d).

As the ratio is increased to $L_b/d_b = 0.5$, one notes that the system shows stable limit cycles that turn into unstable ones at a Limit Point of Cycles (LPC). The LPC is a fold bifurcation, and it is one type of bifurcation that can occur in limit cycles, the others being Period-Doubling (PD) and Neimark-Sacker (NS) (WIGGINS, 2003). In the present system, only the fold bifurcation occurs due to the fluid-film bearing model adopted. It is worth mentioning that the zeros of Eq. (3.48a) or (3.49a) give automatically *all solutions* of the system. Thus, at line A–A in Figure 5.2b, both stable and unstable limit cycles are already given by the CMR. On the other hand, in MATCONT one must continue the solution, encounter the LPC, and continue further to find the unstable cycles. Although the CMR predicted higher unstable cycles, the stable cycles are quite accurate, as shown in Fig. 5.2e.

In Fig. 5.2c-f, the ratio is $L_b/d_b = 0.65$, and one notes that no stable solutions exist after the instability and the bifurcation is sub-critical, with a very small limit cycle.

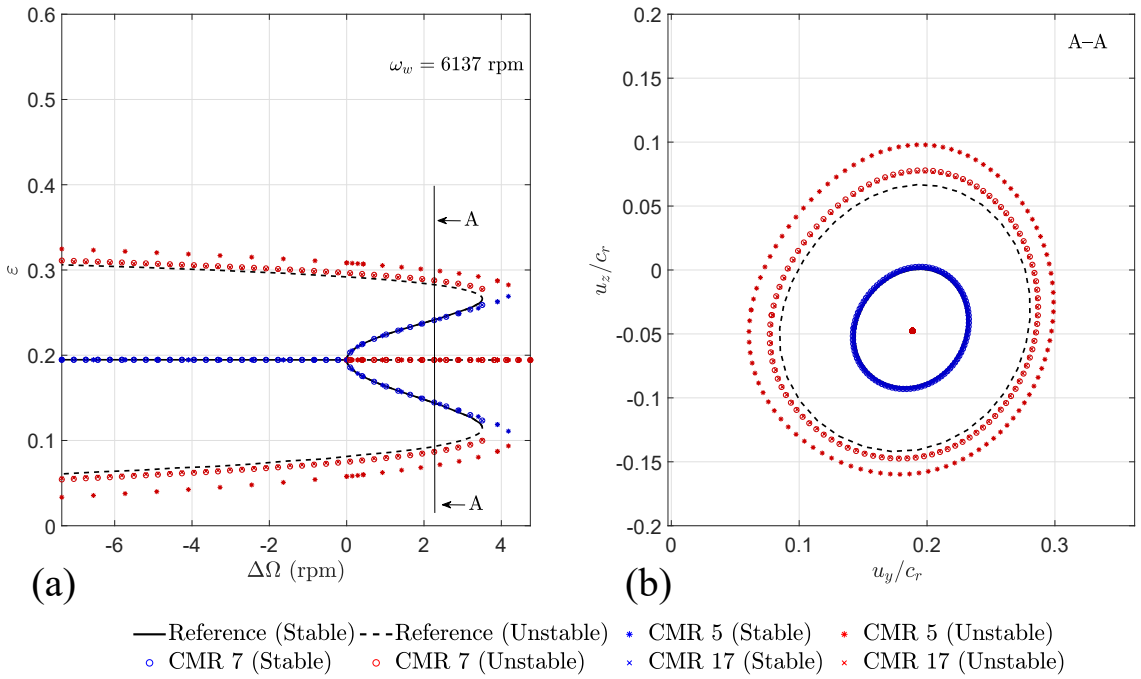

Figure 5.3: Limit cycles for $L_b/d_b = 0.5$ considering higher polynomial orders for the CMR.

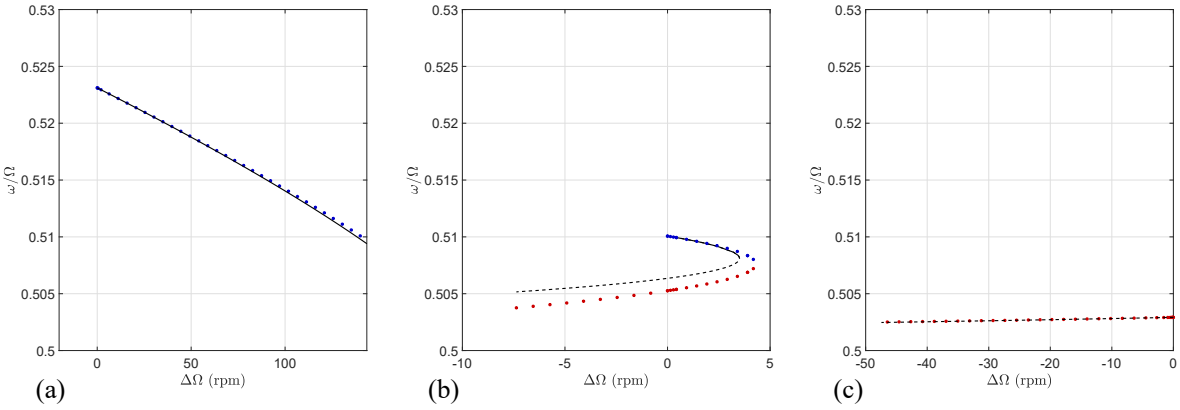

Figure 5.4: Effect of L_b/d_b ratio on the whirl frequency ratio: $L_b/d_b = 0.4$ (a), $L_b/d_b = 0.5$ (b) and $L_b/d_b = 0.65$ (c).

Compared with the other cases, it is clear that this is the less optimal configuration for the rotor system, as any small disturbance will make the rotor unstable even as far as 50 rpm from the instability speed. The disappearance of the stable limit cycles occurs when the LPC point coalesces with the Hopf point. Here, the agreement between the CMR and MATCONT was also very good. By analyzing all results in Fig. 5.2, one notes that the L_b/d_b ratio greatly affects the eccentricity at equilibrium. The higher the eccentricity, the lower the range with stable limit cycles. It is also worth mentioning that, by altering the L_b/d_b ratio, one can alter the type of bifurcation at hand.

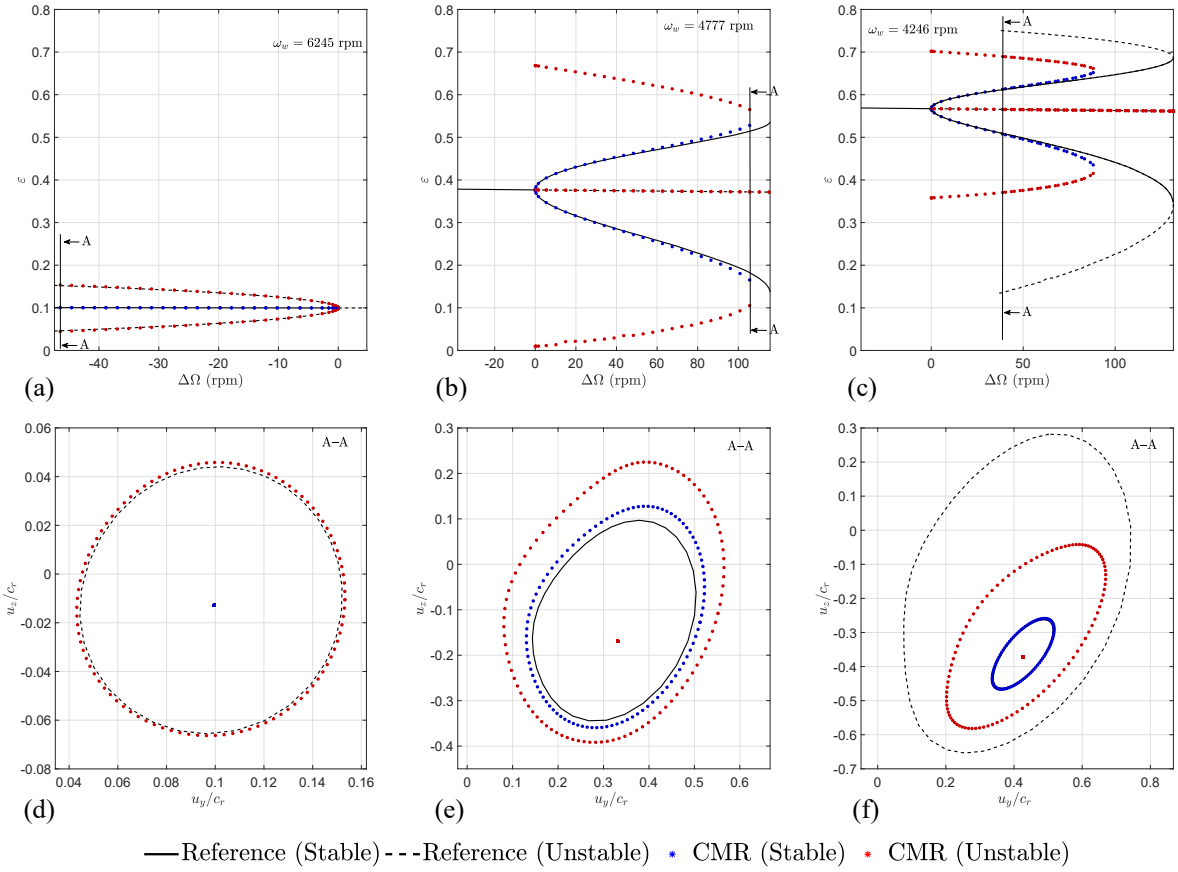

Figure 5.5: Effect of radial clearance c_r on the limit cycles near the instability speed at bearing 1: $c_r = 90$ μm (a-d), $c_r = 180$ μm (b-e) and $c_r = 270$ μm (c-f).

The results of Fig. 5.2 (and all other results, except where indicated) were obtained using a fifth-order polynomial for the CMR. In case better accuracy is required, one can consider higher polynomial orders, which results in higher computational costs as well. Figure 5.3 shows a comparison between the CMR using higher order polynomials, namely 5, 7, and 17, for the case with $L_b/d_b = 0.5$. One sees that the unstable limit cycles are better approximated when higher polynomial orders are considered in the CMR. However, even for a 17th order polynomial, the CMR fails to converge to the numerical result. This is simply a limitation of the approach, which is mostly valid in the neighborhood of the bifurcation.

Figure 5.4 shows the whirl frequency ratio of the limit cycles shown in Fig. 5.2. This frequency is given automatically by MATCONT, while in the CMR it is obtained by substituting the amplitude in Eq. (3.49b). The frequency of the stable limit cycle is what it is known as oil-whirl frequency, and it is observed in experiments as a stable solution (MUSZYNSKA, 1988; El-Shafei et al., 2004). Both MATCONT and CMR showed results consistent with experiments, where the frequency of the limit cycles was sub-synchronous and around $0.5\times\Omega$. It is also worth mentioning that the frequency in Fig. 5.4c corresponds to an unstable cycle, and it cannot be reached in practice. When the rotor encounters

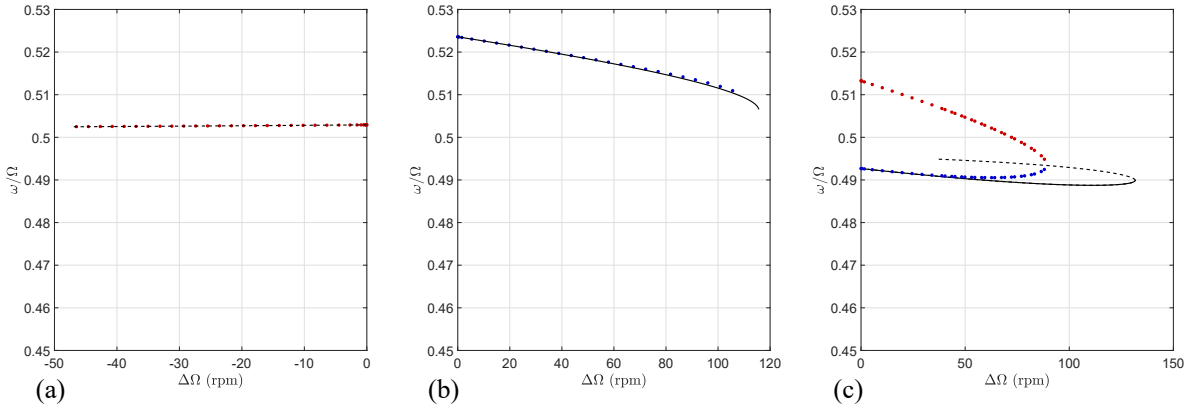

Figure 5.6: Effect of radial clearance c_r on the whirl frequency ratio: $c_r = 90$ μm (a), $c_r = 180$ μm (b) and $c_r = 270$ μm (c).

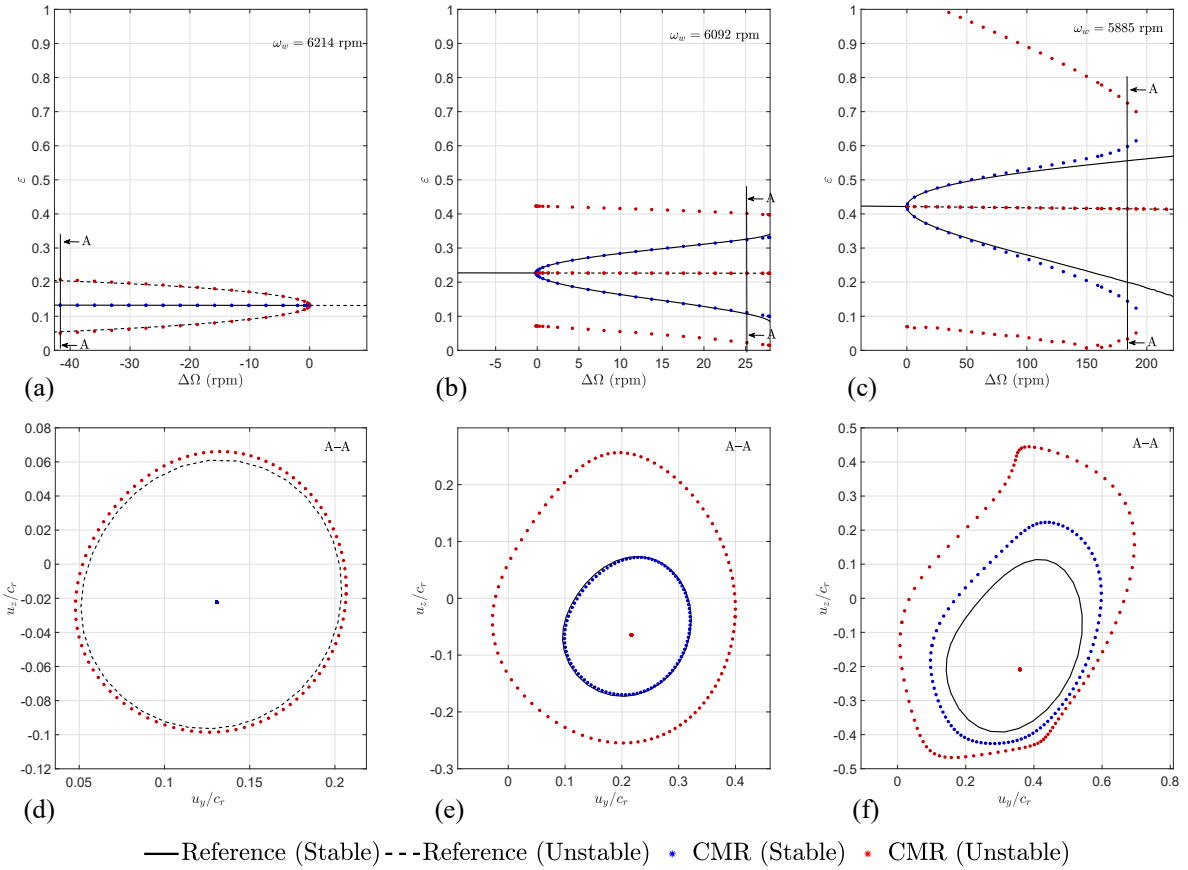

Figure 5.7: Effect of fluid viscosity μ on the limit cycles near the instability speed at bearing 1: $\mu = 0.0209$ Pa·s ($T = 50$ °C) (a-d), $\mu = 0.0114$ Pa·s ($T = 70$ °C) (b-e) and $\mu = 0.0046$ Pa·s ($T = 100$ °C) (c-f).

an unstable cycle, it spirals until it reaches a physical barrier or another stable solution. This is often called oil-whip and is more violent than oil-whirl.

The effect of the radial clearance in the limit cycles is shown in Fig. 5.5. The

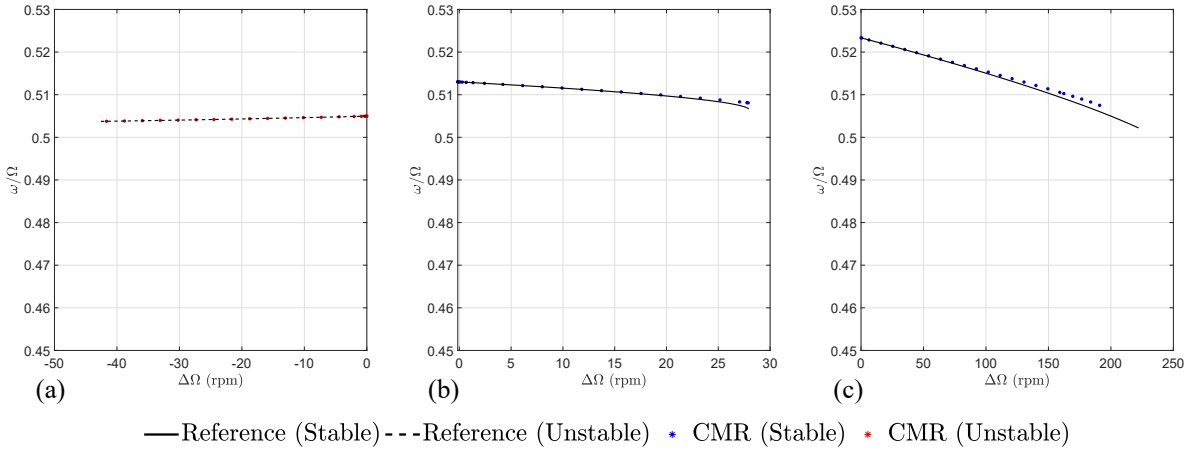

Figure 5.8: Effect of fluid viscosity μ on the whirl frequency ratio: $\mu = 0.0209$ Pa·s ($T = 50$ °C) (a), $\mu = 0.0114$ Pa·s ($T = 70$ °C) (b) and $\mu = 0.0046$ Pa·s ($T = 100$ °C) (c).

increase of the radial clearance has the effect of increasing the eccentricity at equilibrium, opposite to what occurs if the ratio L_b/d_b is increased. When $c_r = 180$ μm, the CMR predicts an LPC point and unstable limit cycles. In MATCONT, the solutions could not be continued further due to numerical difficulties (when the eccentricity becomes too small, $\varepsilon \approx 0$, the system becomes stiff and the Newton-Raphson procedure in MATCONT does not converge), and the LPC point could not be reached. When $c_r = 270$ μm, however, MATCONT successfully delivered the unstable limit cycles and the LPC point. From Figs. 5.5c-f, one notes that the CMR results for the second bifurcation (after the LPC) are not as accurate as the first one, and numerical continuation is required in such cases. However, in the results of Fig. 5.5, the limit cycles given by the CMR after the LPC point are in general smaller, thus giving a conservative estimate of the presence of unstable solutions, which can still be helpful information in the design stage fluid bearings. In addition, the whirl frequencies are shown in Fig. 5.6, showing similar results to the previous case.

Figure 5.7 presents the last study performed, where the viscosity of the fluid μ was varied. To realistically alter this parameter, the temperature T was varied and the data on the ISO VG 32 fluid was used to obtain the values of μ for a given T (ASTM D2270-10, 2016). Similarly to the previous case, the LPC point could not be reached in MATCONT due to numerical difficulties. Here again, one notes that the CMR is very accurate in the first bifurcation, but gives wrong results in the second one. Nonetheless, the CMR can indicate that there is a presence of an LPC point nearby, but the true point can only be found numerically through continuation. Figure 5.8 shows the whirl frequencies for the case with variable viscosity. Similarly to the previous cases, the frequency is well situated close to $0.5 \times \Omega$.

As one can note from the results in Fig. 5.7, the viscosity greatly affects the

limit cycles at the bifurcation. In general, lower viscosity tends to produce stable limit cycles with a higher speed range. The results agree with experimental data (WANG; KHONSARI, 2006b), where the change in viscosity was shown to affect the type of Hopf bifurcation. The explanation of this change is highlighted in Fig. 5.7, and occurs when the LPC point coalesces with the Hopf bifurcation point.

5.1.2 Complex rotor system

This example presents the applicability of the CMR to a realistic rotor system. Figure 5.9 shows the finite element mesh based on a real turbomachine. The system has a total length of $L = 2.5$ m, weights $W_r = 17.94$ kN, and is discretized using 26 elements and 27 nodes. The elements used are 1D Timoshenko beams in both orthogonal directions, while torsional and axial movements are ignored. Details of the mesh can be consulted in Mereles and Cavalca (2021) or Mereles et al. (2022). The rotor has four rigid disks positioned at nodes 12, 15, 17, and 19; and two bearings at nodes 6 and 23. Although the bearings of the real machine are elliptical, a fixed-geometry cylindrical bearing is considered here, using the model presented in Section 2.1. Two different data for the bearings were considered, and they are listed in Table 5.2. The only difference between the two cases is the radial clearance, which is larger in case II. In addition, the fluid viscosity $\mu = 0.027$ Pa·s (ISO VG 46 at 50 °C) is assumed in both bearings and all cases.

The total number of DOFs of the system presented in Fig. 5.9 is 108 (since each node has 4 DOFs). For the analysis to be feasible using MATCONT, a reduction was performed by means of a Component Mode Synthesis (CMS) method, namely the Craig-

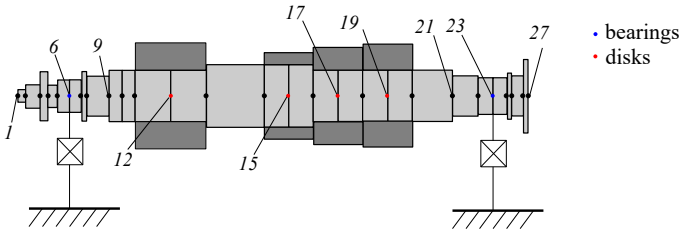

Figure 5.9: Mesh of the complex rotor system.

Table 5.2: Bearing data for the complex rotor system (dimensions in mm).

	Parameter	Case I	Case II
Bearing 1	Length (L_{b1})	88	88
	Diameter (d_{b1})	160	160
	Radial clearance (c_{r1})	0.12	0.34
Bearing 2	Length (L_{b2})	98	98
	Diameter (d_{b2})	180	180
	Radial clearance (c_{r2})	0.135	0.385

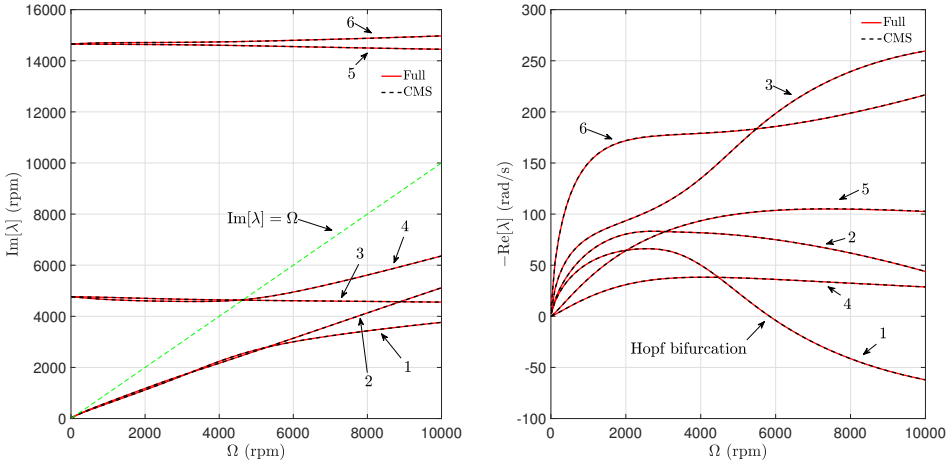

Figure 5.10: Comparison between the first six eigenvalues of the full and CMS-reduced systems using case I data: imaginary (a) and real (b) parts.

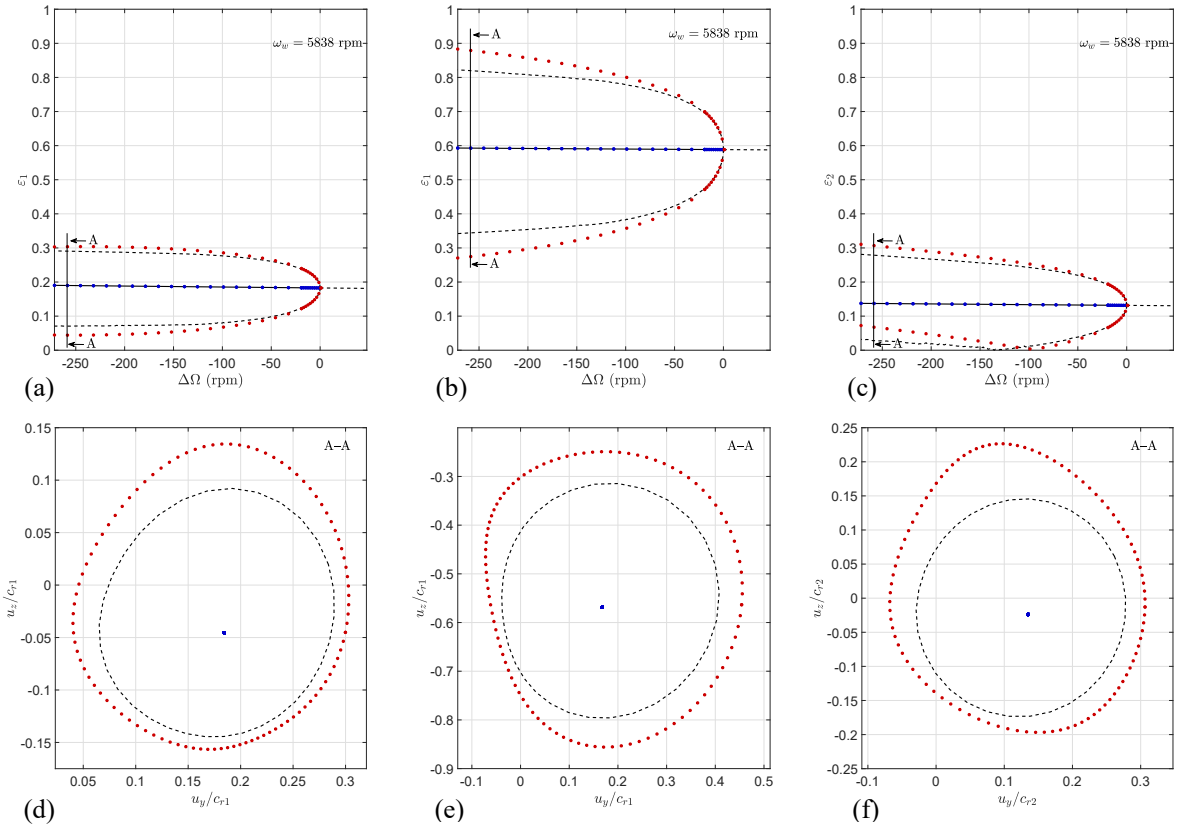

Figure 5.11: Limit cycles of the complex rotor for case I at: bearing 1 (a-d), disk 2 (b-e), and bearing 2 (c-f).

Bampton (CB) method (CRAIG; BAMPTON, 1968; ALLEN et al., 2020). This method is very well established in the literature and was used in many rotordynamic analyses

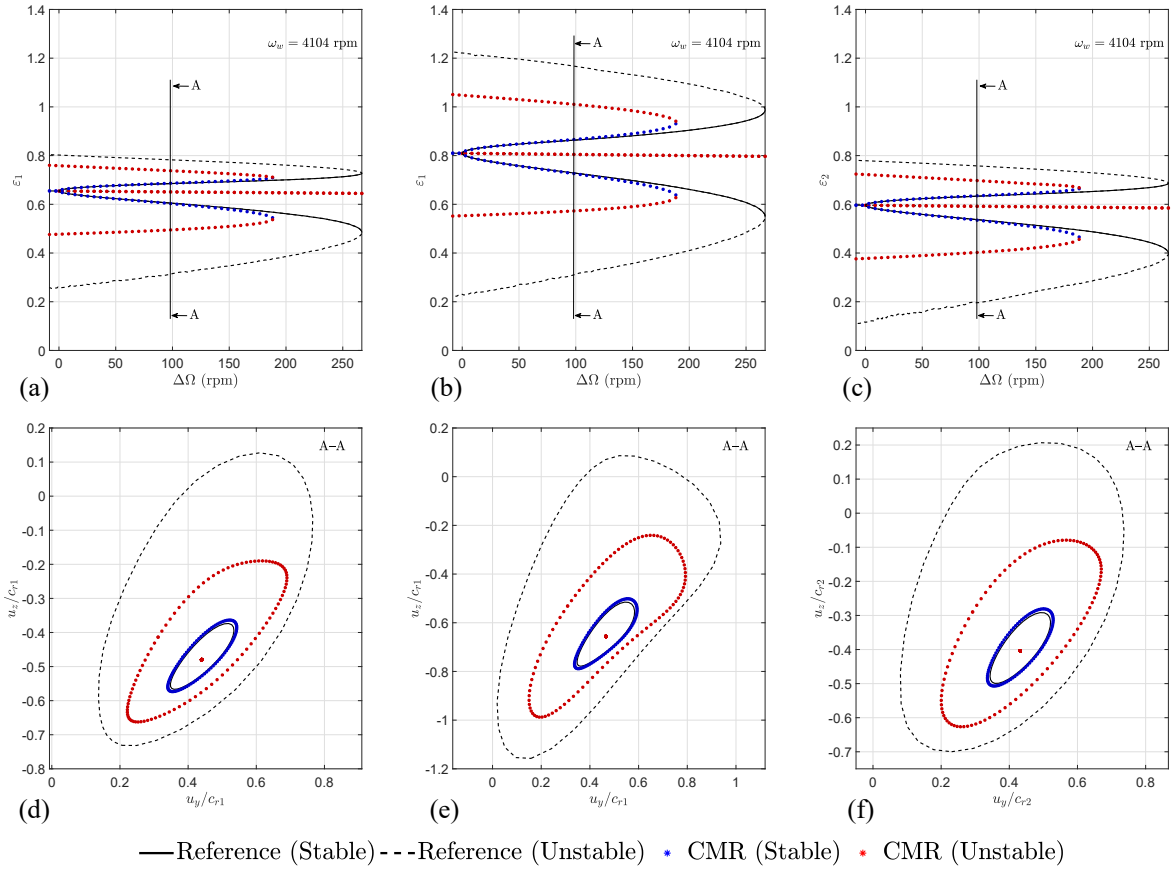

Figure 5.12: Limit cycles of the complex rotor for case II at: bearing 1 (a-d), disk 2 (b-e), and bearing 2 (c-f).

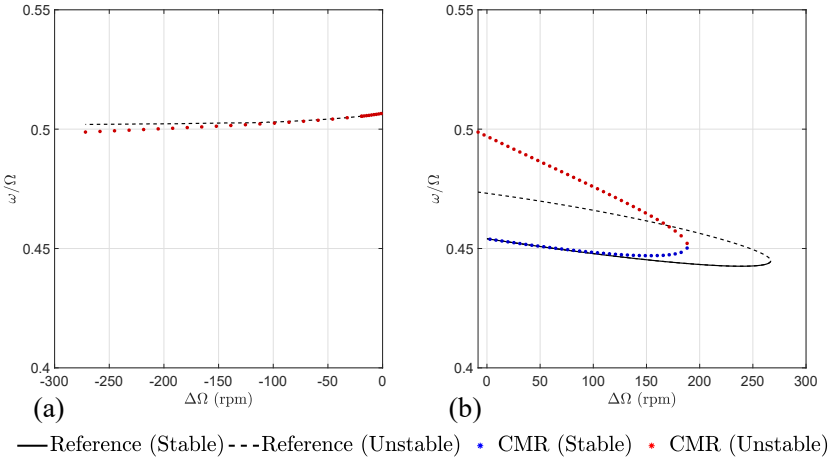

Figure 5.13: Whirl frequency ratio for case I (a) and case II (b).

(WAGNER et al., 2010). In the CB method, the system is divided into boundary DOFs, which are kept in physical form, and internal DOFs, which are reduced using fixed interface modes. In the present case, the boundary DOFs consist of the bearing DOFs (nodes 6 and 23), and the remaining DOFs are labeled as internal. A total of 8 fixed interface modes are used in the system. Hence, the rotor is reduced from 108 to 16 DOFs, which allows

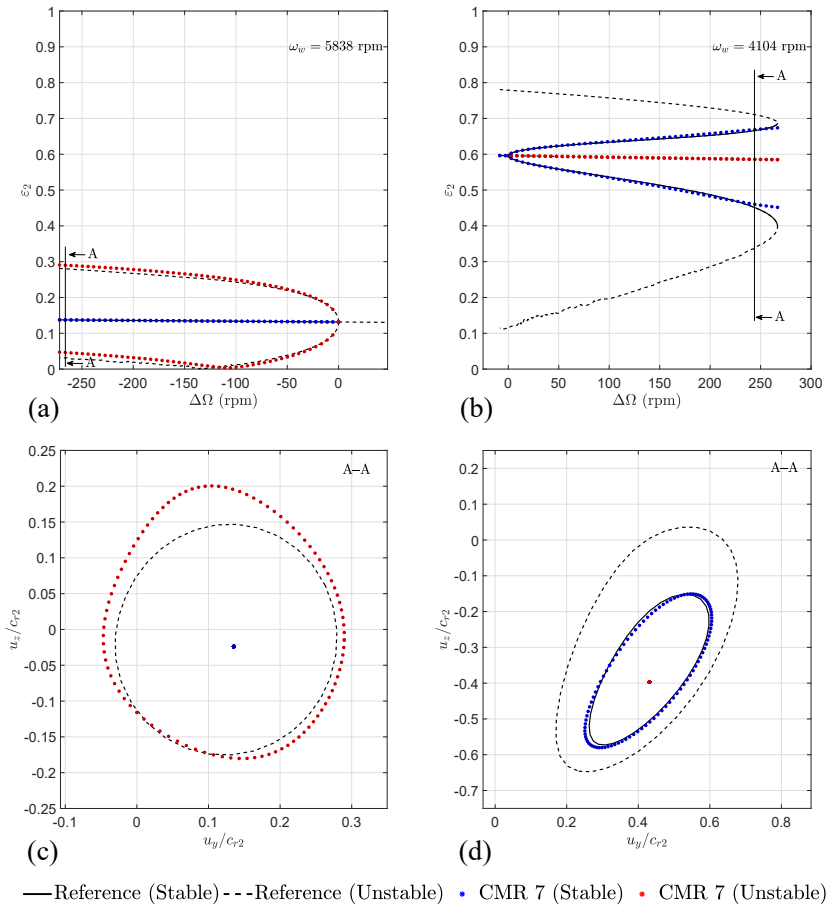

Figure 5.14: Limit cycles of the complex rotor for bearing 2 considering a higher order polynomial: case I (a-c), and case II (b-d).

the use of numerical continuation methods. It is worth mentioning that this reduction is optional in the CMR method, as the approach can handle high-dimensional systems with a reasonable computational time. However, to make the comparison between MATCONT and the CMR, the system reduced by the CMS was used. This means that the modes used in Eq. (3.24) were obtained using the matrices reduced by the CMS, instead of the full finite element matrices. Figure 5.10 shows a comparison between the eigenvalues of the full and the CMS reduced systems using data from case I. As one notes, the reduction is very effective in reducing the numerical cost and maintaining accuracy.

Figure 5.11 shows the limit cycles of the complex rotor near the instability speed ω_w for case I at three different points of the rotor: bearing 1 (node 6), disk 2 (node 15), and bearing 2 (node 23). In these figures, $\varepsilon_1 = |u|/c_{r1}$ and $\varepsilon_2 = |u|/c_{r2}$, where $|u|$ is the maximum/minimum radial displacement at the indicated axial position. One can note that, for these bearing parameters, the bifurcation is sub-critical, with an unstable limit cycle reaching as far as 250 rpm from the instability speed. The CMR gives very accurate results near the bifurcation, but it exhibits larger errors for higher speeds when compared with numerical continuation. For this reason, the analysis was stopped at around 275 rpm.

This error can be diminished by considering a higher polynomial order for the CMR, as shown in Fig. 5.14.

Figure 5.12 shows the limit cycles at the same points of the rotor but using the data of case II. Here, one has a super-critical bifurcation followed by a second bifurcation at an LPC, which turns the stable limit cycle into an unstable one. Similarly to the previous example, the CMR agrees very well with MATCONT in the stable limit cycles but shows large errors for the unstable ones. The results of the CMR can be understood as a conservative estimate of the unstable limit cycles after the LPC. The whirl frequency ratio for cases I and II are shown in Fig. 5.13. One notes that the frequencies stay very close to $0.5\times\Omega$, similar to the previous study. One should note, however, that the unstable frequencies are not actually reachable; only the stable ones are.

Figure 5.14 shows the limit cycles at bearing 2 for both cases considering a seventh-order expansion in the CMR. As one can note by comparing with the previous cases, the accuracy of the limit cycles given by the CMR is greatly improved further from the bifurcation point. It is worth noting, however, that the LPC was not predicted by the seventh-order CMR, as Fig. 5.14b shows. Therefore, the CMR can be used reliably to study the limit cycles from the Hopf bifurcation, but not the subsequent bifurcation of the limit cycles.

5.2 Non-autonomous system

In this section, the effect of unbalance in the simple system studied in the autonomous case (Fig. 5.1) is established. The CMR approach presented in Section 3.3.2 is employed. A fifth-order polynomial is used and is evaluated by comparing it with numerical integration, which was performed using the `ode45` integrator of the software MATLAB$^{\text{TM}}$. Figures 5.15-5.17 show this evaluation for $L_b/d_b = 0.4$, where the displacements are measured at bearing 1. The autonomous result of this case is shown in Figs. 5.2a-d. In addition, the speed is set to $\Delta\Omega = 50$ rpm, and three levels of unbalance are considered, namely, $m_{un} = 1$, 10 and 20 g·mm. These values of unbalance correspond approximately to the ISO grades G 1, G 2.5 and G 6.3, respectively. As unbalance is added to the system, the periodic limit cycles turn to quasi-periodic solutions. By analyzing the figures, one notes that the results of the CMR are very close to the numerical integration in both the time and frequency domains. The latter results are obtained by applying the Fast Fourier Transform (FFT) on the complex vibration signal, in order to obtain the full spectrum. However, it is worth noting that the CMR results do not require any numerical integration, only the solution of a polynomial equation, as shown in Section 3.3.2. Additionally, the CMR gives all solutions, including the $1\times$ harmonic response, which turns unstable at the bifurcating point. The transient simulation can

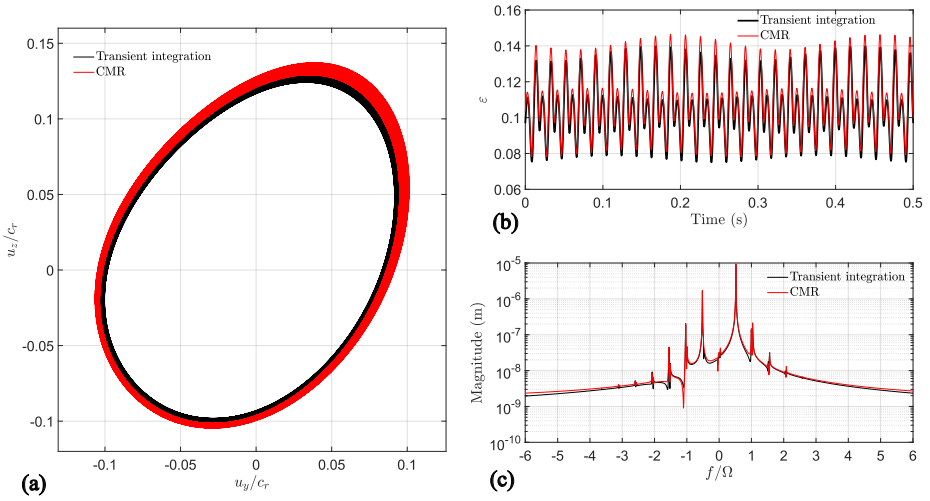

Figure 5.15: Comparison between CMR and transient integration for the non-autonomous rotor with $\Delta\Omega = 50$ rpm, $L_b/d_b = 0.4$ and $m_{un} = 1$ g·mm: orbit (a), radial displacement (b) and frequency spectrum (c).

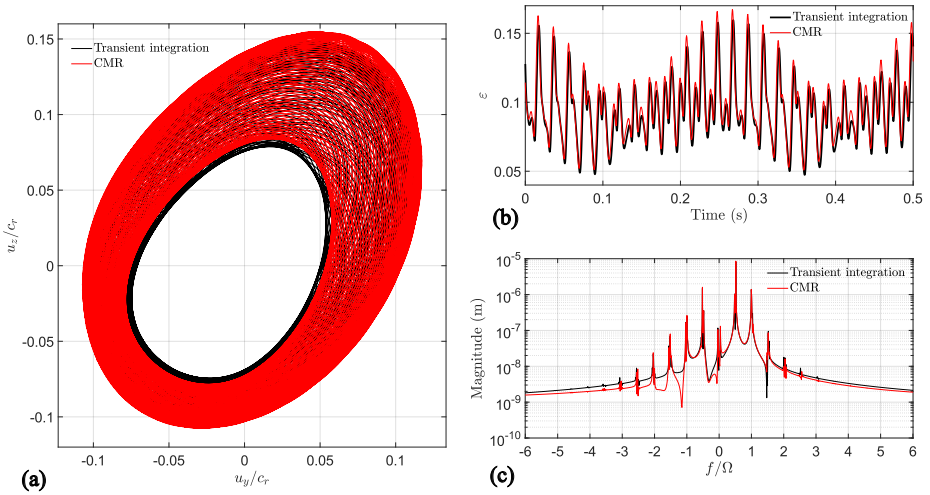

Figure 5.16: Comparison between CMR and transient integration for the non-autonomous rotor with $\Delta\Omega = 50$ rpm, $L_b/d_b = 0.4$ and $m_{un} = 10$ g·mm: orbit (a), radial displacement (b) and frequency spectrum (c).

only give stable solutions.

Figure 5.18 shows the effect of unbalance in the emerging limit cycles close to the Hopf bifurcation. These figures show the maxima and minima of the vertical displacement of the rotor. Thus, multiple dots indicate a quasi-periodic solution, while a fixed number indicates a periodic one. Figure 5.18a shows that when unbalance is small, in this case $m_{un} = 1$ g·mm, the autonomous and non-autonomous systems are very similar, as one may note by comparing Figs.5.2a and 5.18a. As Figs. 5.18b-c show, the postponement of the instability point is the main effect of increasing unbalance, which happens when the $1\times$ solution turns unstable. This means that, if the external excitation is strong enough,

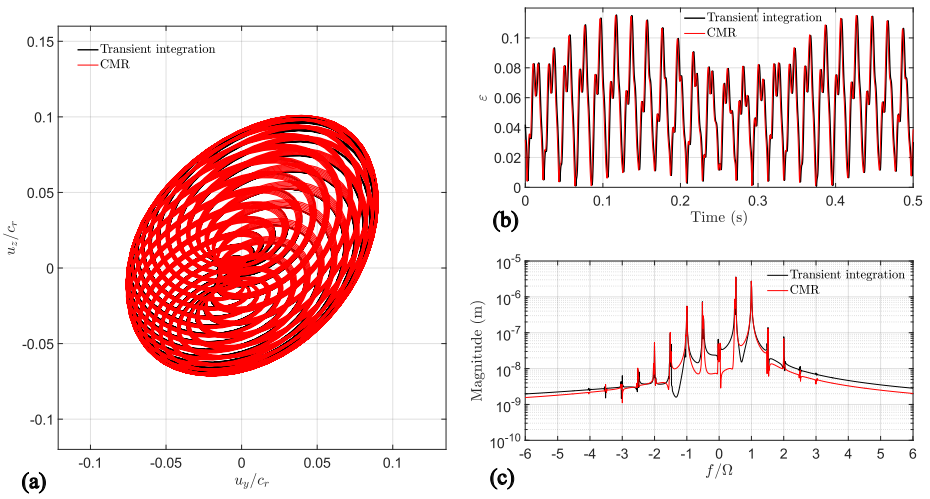

Figure 5.17: Comparison between CMR and transient integration for the non-autonomous rotor with $\Delta\Omega = 50$ rpm, $L_b/d_b = 0.4$ and $m_{un} = 20$ g·mm: orbit (a), radial displacement (b) and frequency spectrum (c).

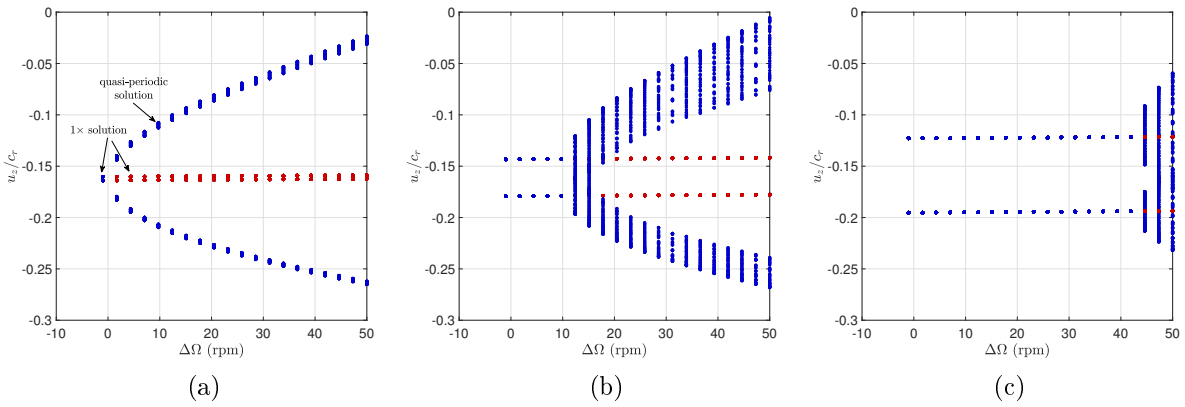

Figure 5.18: Effect of unbalance on the limit cycles near the instability speed at bearing 1 with $L_b/d_b = 0.4$: $m_{un} = 1$ g·mm (a), $m_{un} = 10$ g·mm (b) and $m_{un} = 20$ g·mm (c).

the effect of unbalance cannot be neglected in order to obtain the instability point.

Figure 5.19 shows the effect of unbalance when the bifurcation of the autonomous system is sub-critical, while the previous response corresponded to a super-critical case. It is interesting to note that the effect of unbalance in the instability point has now the opposite outcome, that is, when unbalance is increased, the instability now occurs at an earlier speed. This highlights the importance of knowing the type of bifurcation the system presents. It is also worth noting that the sub-critical case is much more dangerous, as the instability can occur prior to the threshold speed predicted by the autonomous system.

It was shown that the unbalance can affect the speed at which the rotor 1× solution becomes unstable. In addition to this, the non-autonomous system can also change the type of bifurcation the autonomous system displays, as Fig. 5.20 shows. As unbalance is

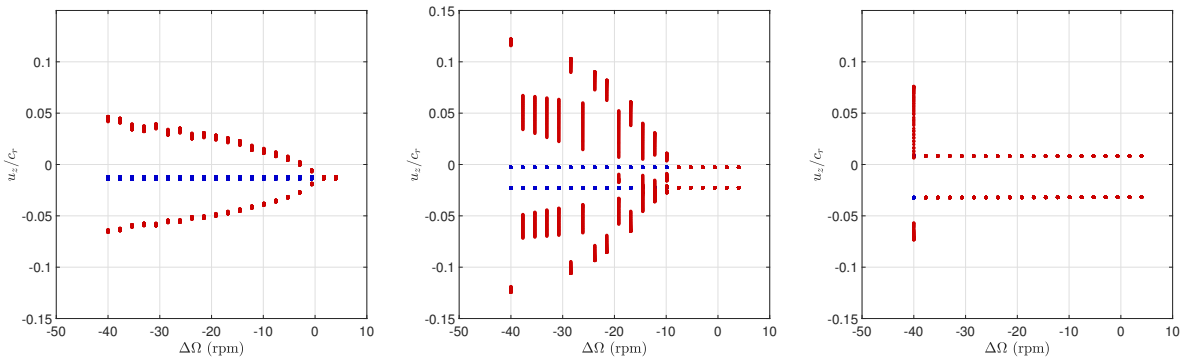

(a) (b) (c)

Figure 5.19: Effect of unbalance on the limit cycles near the instability speed at bearing 1 with $L_b/d_b = 0.65$: $m_{un} = 1$ g·mm (a), $m_{un} = 10$ g·mm (b) and $m_{un} = 20$ g·mm (c).

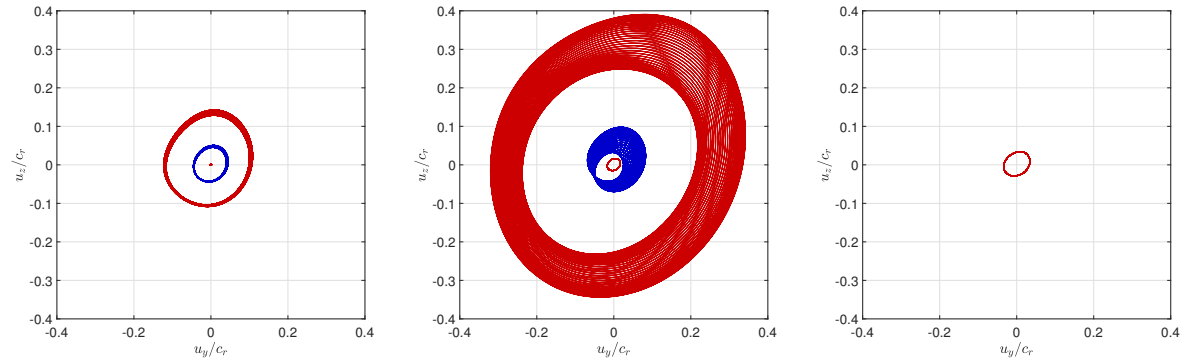

(a) (b) (c)

Figure 5.20: Change of bifurcation when unbalance is added for $\Delta\Omega = 1.2$ rpm and $L_b/d_b = 0.5$: $m_{un} = 1$ g·mm (a), $m_{un} = 10$ g·mm (b) and $m_{un} = 20$ g·mm (c). Here, the red orbits denote unstable solutions, while the blue orbits denote stable ones.

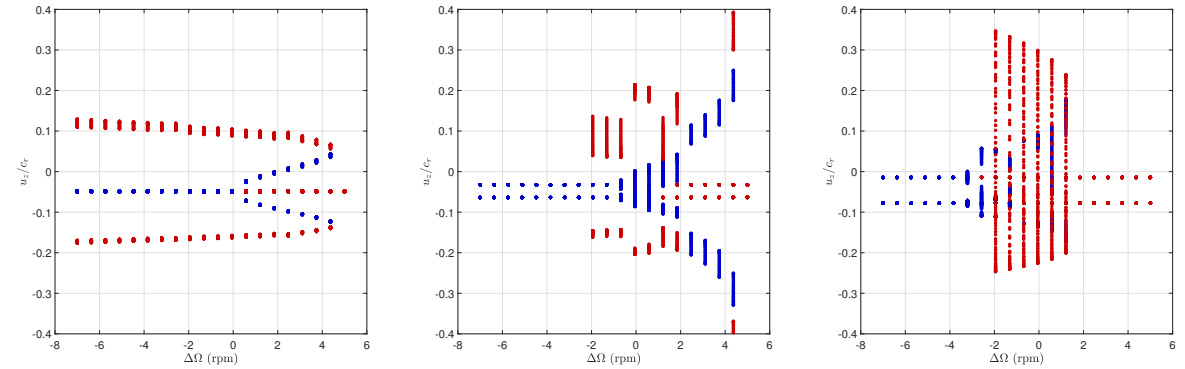

(a) (b) (c)

Figure 5.21: Effect of unbalance on the limit cycles near the instability speed at bearing 1 with $L_b/d_b = 0.5$: $m_{un} = 1$ g·mm (a), $m_{un} = 10$ g·mm (b) and $m_{un} = 20$ g·mm (c).

increased, the stable and unstable quasi-periodic solutions annihilate each other, leaving only the unstable 1× solution. This means that the stable solution that existed before the unbalance was added cannot be reached anymore. Figure 5.21 presents the same case of Fig. 5.20 but for different rotational speeds. The autonomous counterpart of this result is shown in Fig. 5.2b. Here it is possible to see that the change of bifurcation type occurs because the unstable solutions become superimposed with the stable ones.

This section showed how the CMR can be used to obtain quasi-periodic solutions of rotors under both fluid instability and unbalance. From the results, one notes that the inclusion of the external excitation is very important if one is trying to estimate precisely the speed at which oil-whip/whirl occurs. These outcomes agree with the ones obtained by Rendl et al. (2023) using numerical continuation.

6 EXPERIMENTAL STUDY

This chapter presents an experimental validation of the approach proposed to detect whether the system will present oil-whirl or oil-whip. The test rig was described in detail in Chapter 4. Measurements were conducted at fixed motor speeds, with a sampling frequency of 4096 Hz over a period of five seconds. Prior to each measurement, a five-second pause was implemented to ensure that the response reached a stationary state.

The numerical studies revealed that variations in the bearing parameters can influence the type of bifurcation exhibited by the system. To validate the model predictions, certain parameters were intentionally adjusted in the real system, and the resulting bifurcation type was analyzed. The objective is to evaluate the model's ability to accurately anticipate changes in bifurcation within the real system. Specifically, two parameters, namely the bearing clearance and disk position, were selected for manipulation. This study involves modifying these parameters in both the experimental setup and the model, followed by a comparison of the results obtained.

As shown in Section 5.2, the amount of unbalance may affect the onset of instability or even change the type of bifurcation displayed by the autonomous system. In view of this, the rotor was well-balanced before each set of measurements to ensure a low unbalanced moment. Measurements with the rotor balanced and with a known unbalance were then performed. When the rotor reaches the oil-whip state, the measurements are immediately aborted, so no damage is caused to the bearings and sensors. Hence, the rotor does not develop the full circular motion characteristic of oil-whip, which was depicted in Fig. 2.3a.

6.1 Rotor with one disk

Figure 6.1 depicts the dimensions and finite element mesh of the rotor with one disk, while Table 6.1 lists the properties of the system. The domain is subdivided into 16 Timoshenko beam elements. The journals and disk are considered rigid masses with moments of inertia and are placed at nodes 4, 9, and 14. In order to reduce the number of

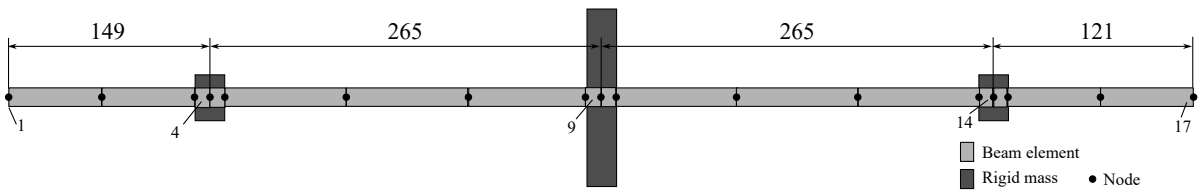

Figure 6.1: Finite element model of the rotor with one disk (dimensions in mm).

Table 6.1: Properties of the rotor system.

Description	Value
Young's modulus (E)	207 GPa
Poisson's ratio (ν)	0.3
Density of the material (ρ)	7850 kg·m^3
Mass of shaft	0.71 kg
Mass of disk(s)	1.71 kg
Mass of journal(s)	0.96 kg
Diametral moment of inertia of disk(s)	1.61 kg·mm^2
Polar moment of inertia of disk(s)	3.10 kg·mm^2
Diametral moment of inertia of journal(s)	0.010 kg·mm^2
Polar moment of inertia of journal(s)	0.013 kg·mm^2
Bearing length	18 mm
Bearing radial clearance	90 and 130 μm
Oil dynamic viscosity	0.045 Pa·s[1]

[1]ISO VG at 25 C°

DOFs of the system, a Component Mode Synthesis (CMS) approach was used, namely the Craig-Bampton (CB) technique. The master nodes were chosen to be the bearing nodes (nodes 4 and 14). The CB method is widely used in the literature, and one is referred to Mereles et al. (2023) on how to implement it in a rotor system. Additionally, an isotropic constant stiffness of 28 kN/m is placed at node 1 of the model to mimic the effect of the flexible coupling. The value of this stiffness was adjusted to match the critical speeds of the model with the measured ones.

In this study, the radial clearance of the system was changed in both the real and modeled rotors. The values were 90 and 130 μm. As mentioned above, the idea of the study is to see the effect of this change in the type of instability, either oil-whirl or oil-whip, displayed by the system. However, the simulated and measured synchronous

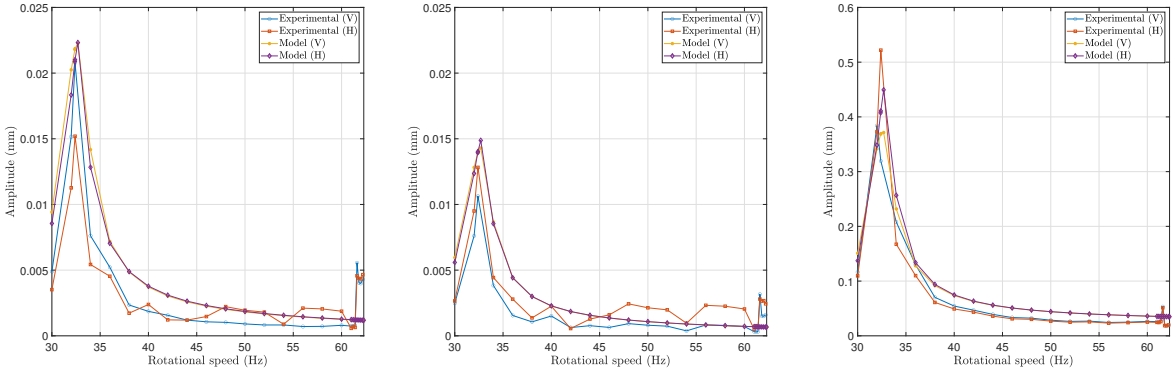

(a) (b) (c)

Figure 6.2: Comparison between measured and simulated 1× response with 90 μm clearance: bearing 1 (a), bearing 2 (b) and disk (c).

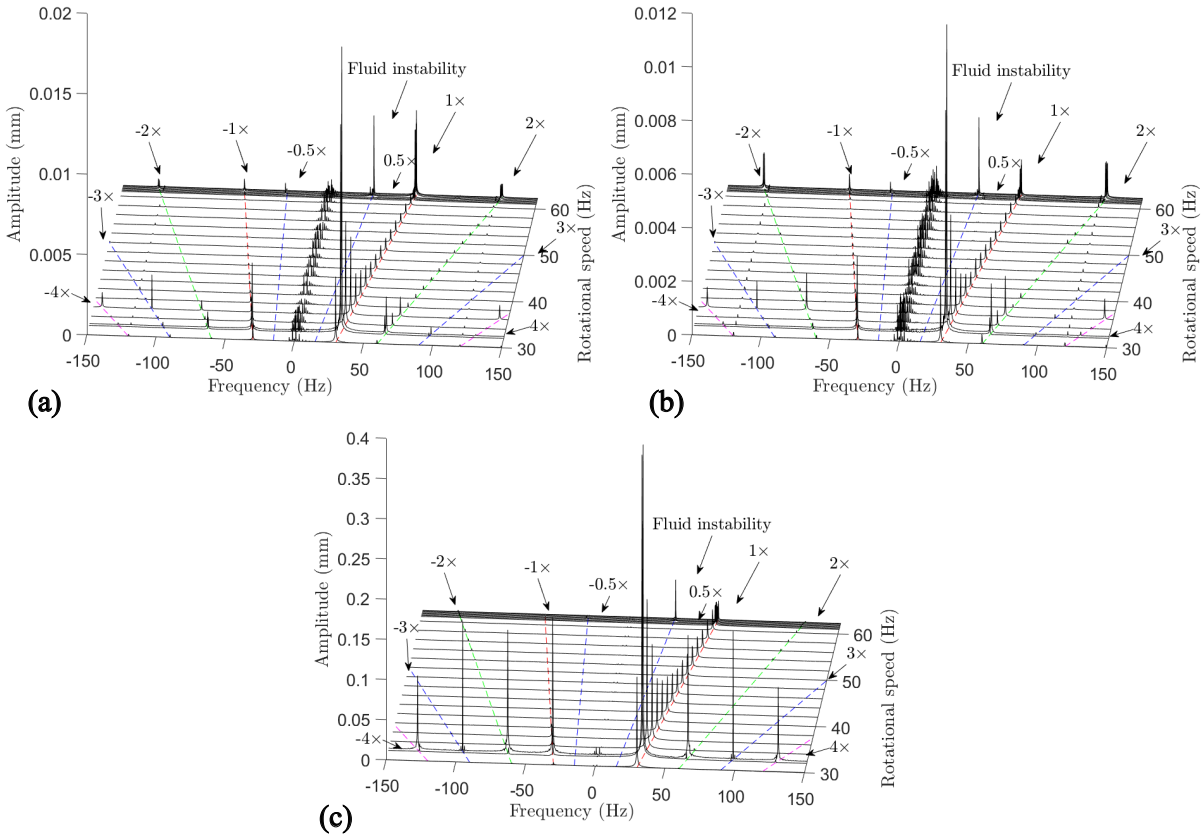

Figure 6.3: Measured waterfall diagrams with 90 μm clearance: bearing 1 (a), bearing 2 (b) and disk (c).

responses are compared prior to the assessment of the bifurcation. This result is shown in Fig. 6.2 for the rotor with 90 μm of radial clearance. To obtain these figures, the Fast Fourier Transform (FFT) is applied in the measured signal and only the 1× component is extracted. In order to obtain the full spectrum, the FFT is applied to a complex signal, in which the real part is the horizontal measurement while the imaginary part is the vertical one. The response of the model is obtained by applying the Harmonic Balance Method (HBM) (KRACK; GROSS, 2019), using three harmonics, and subsequently the FFT. Note that this approach considers nonlinearities of the bearing force. In addition, the experimental signal was obtained by a subtraction between the balanced and unbalanced systems (with a known unbalance of 1 g at a 50 mm radius). Note that, the difference of signals is used in order to reduce the impact of other effects not considered in the model, such as shaft bow, misalignment, and others. As one may note from Fig. 6.2, there is a good agreement between the experiment and the model.

With the model and experiment in agreement with respect to the unbalanced synchronous response, the next step is to evaluate the fluid instability. Figure 6.3 shows the experimental waterfall plots, which are obtained using the difference between the balanced and unbalanced signals. In addition to the critical speed on the 1× line, one also notes the emergence of a peak on the 0.5× line, which is the fluid-induced instability.

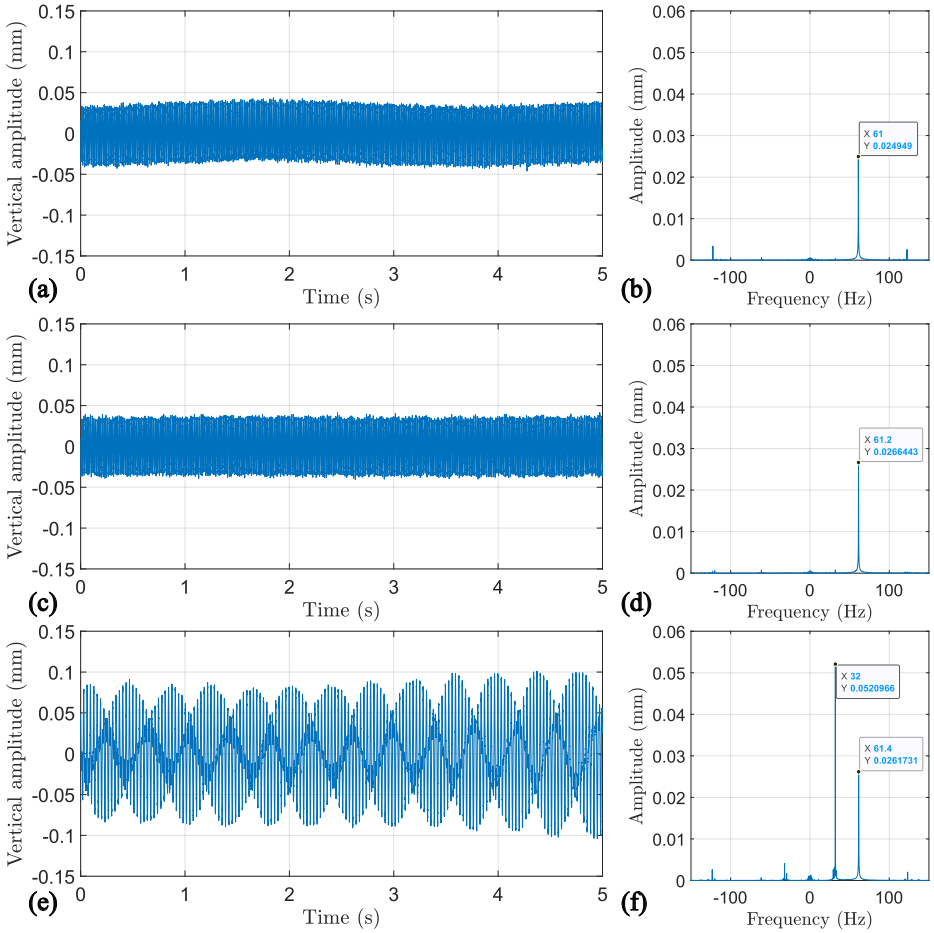

Figure 6.4: Measured time signals and frequency spectrum of the disk during the transition to fluid instability at: 61 Hz (a-b), 61.2 Hz (c-d) and 61.4 Hz (e-f). Rotor with 90 μm of radial clearance.

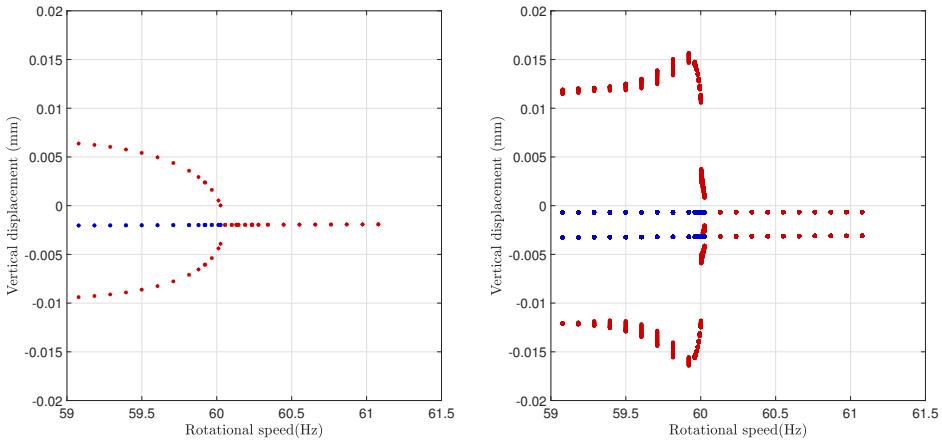

(a) (b)

Figure 6.5: CMR predictions for the rotor with 90 μm clearance and one disk near fluid instability: autonomous (a) and non-autonomous (b).

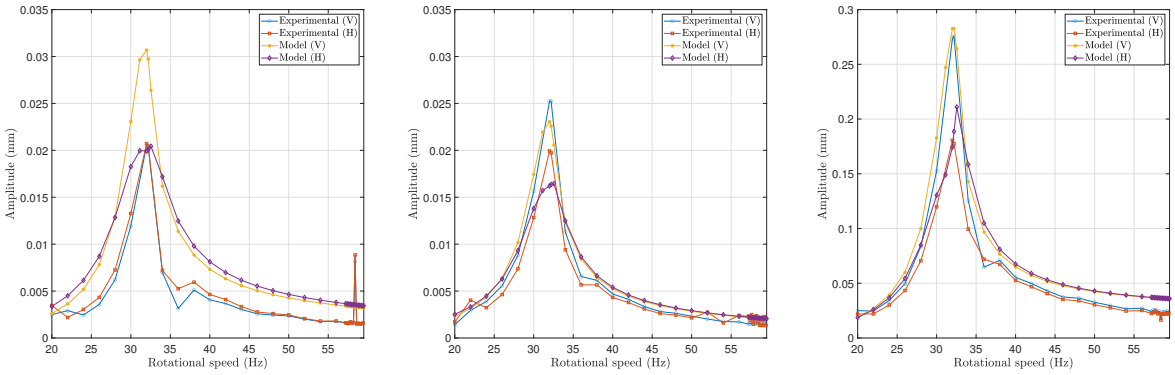

Figure 6.6: Comparison between measured and simulated 1× response with 130 μm clearance: bearing 1 (a), bearing 2 (b) and disk (c). Here V - vertical and H - horizontal.

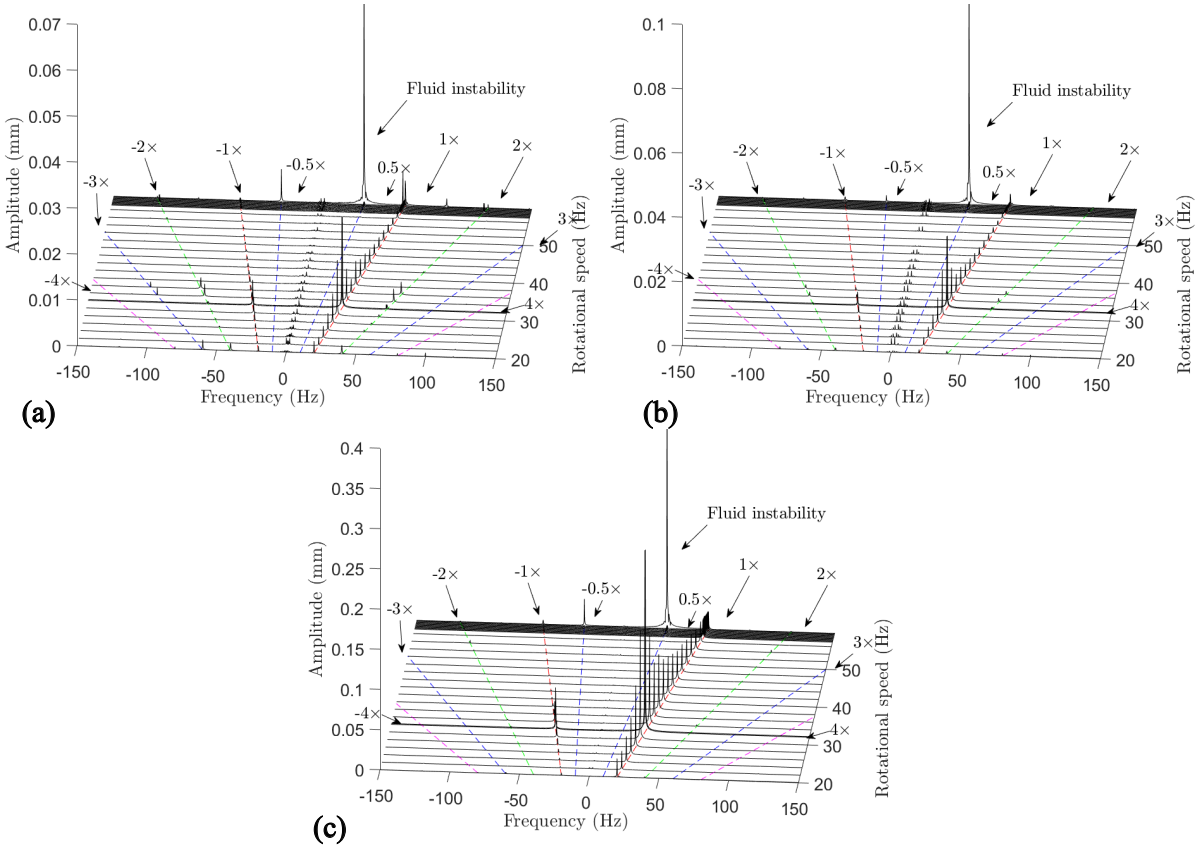

Figure 6.7: Measured waterfall diagrams with 130 μm clearance: bearing 1 (a), bearing 2 (b) and disk (c).

However, it is not clear from these results whether the instability was oil-whirl or oil-whip. Figure 6.4 shows the last three measurements of the displacement of the disk right before the rotor becomes unstable. As one may see from the frequency spectrum, there is no 0.5× component up until the rotor enters oil-whip. Therefore, this case corresponds to a sub-critical bifurcation, in which no stable solutions exist after to oil-whip. This

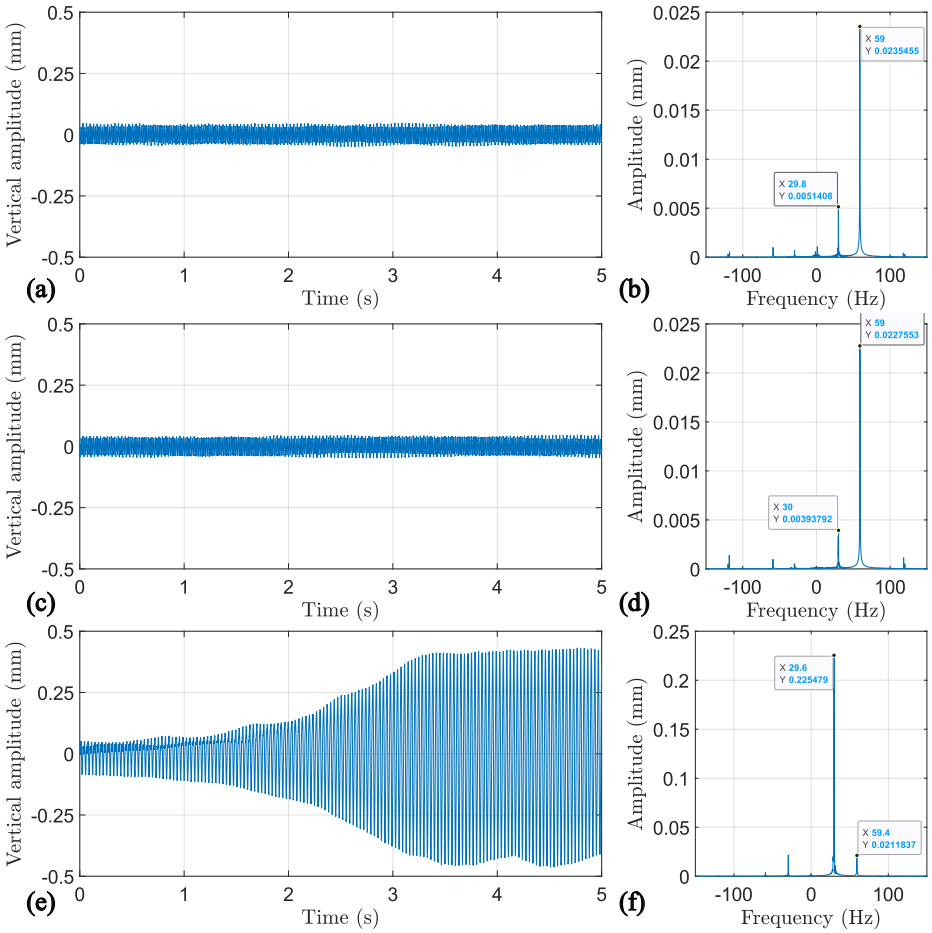

Figure 6.8: Measured time signals and frequency spectrum of the disk during the transition to fluid instability at: 59 Hz (a-b), 59.2 Hz (c-d) and 59.4 Hz (e-f). Rotor with 130 μm of radial clearance.

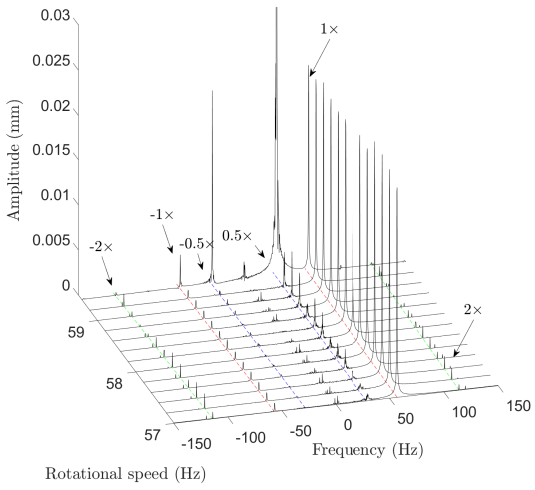

Figure 6.9: Expanded view of the waterfall diagram of the disk near fluid instability for the rotor with 130 μm of radial clearance.

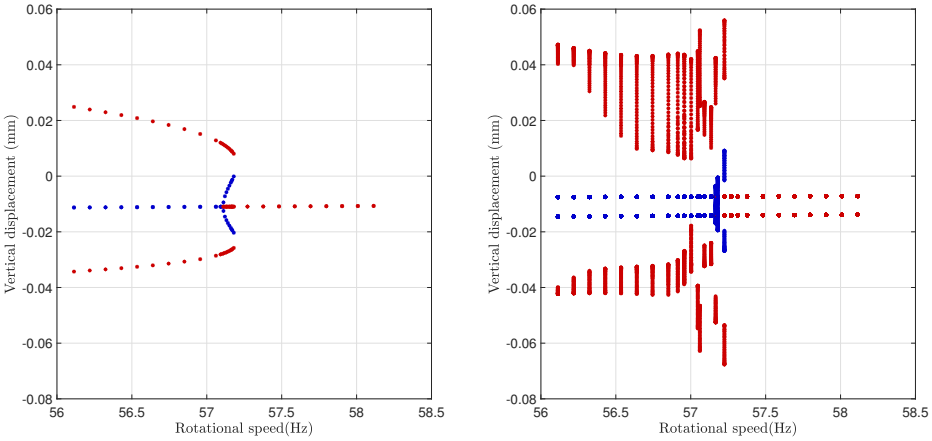

(a) (b)

Figure 6.10: CMR predictions for the rotor with 90 μm clearance and one disk near fluid instability: autonomous (a) and non-autonomous (b).

result also highlights how the sub-critical bifurcation is very sudden: for 61.2 Hz the system appears stable with no indication of any problem, but at 61.4 Hz, the operation is no longer possible. In addition, Figure 6.5 shows the predictions of the model with and without unbalance. As one may note, the model correctly predicted the sub-critical bifurcation, but the speed was lower, at 60.1 Hz, which, again, works as a conservative estimative of the phenomenon.

After the previously reported results were obtained, the 90 μm bearing bush was substituted by a now one with a radial clearance of 130 μm. According to the numerical studies presented in Chapter 5, the increase of the radial clearance may change the type of bifurcation. Firstly, Figure 6.6 shows a comparison between the measured and simulated 1$\times$ responses. As in the previous case, the signal consists of the difference between the balanced and the unbalanced rotor with a mass of 1 g at 50 mm. As seen in the figures, the agreement is very good between the model and experimental measurements.

Next, the rotor is driven to the fluid instability in order to evaluate the type of bifurcation at hand. Figure 6.7 shows the measured waterfall diagrams, where the occurrence of the instability is clear on the 0.5$\times$ line. To investigate the type of bifurcation at hand, Figure 6.8 shows the last three measurements of the disk. Differently from the previous case, one can note the appearance of a 0.5$\times$ component already at 59 Hz. This indicates that the rotor reached a stable oil-whirl solution prior to the oil-whip, meaning that the type of bifurcation is super-critical. By comparing this case with the one shown in Fig. 6.4, it is arguably that the former is much more favorable, as there is a clear indication in the frequency spectrum that oil-whip is nearby.

Figure 6.8 showed that at 59 Hz the rotor already appears to be in oil-whirl. To

Table 6.2: Experimental frequencies against model (Rotor with one disk).

Case		Critical speed (Hz)	Instability speed (Hz)
90 μm	Experiment	32.4	61.4
	Model	32.7	60.1
	Error (%)	0.93	2.12
130 μm	Experiment	32.2	57-57.6*
	Model	32.5	57.1
	Error (%)	0.92	0.17-0.87

*The speed is considered a range due to the difficulty in precisely defining it.

point out the speed in which this regime started, Figure 6.9 shows an expanded view of the waterfall diagram of the disk at the last measured speeds. One may note that the 0.5× component is already present at 57 Hz, but it is weaker. The component appears to increase at 57.6 Hz, so the experimental onset speed for the oil-whirl phenomenon is considered to be in the range 57-57.6 Hz in this case. The prediction of the model using the CMR is shown in Fig. 6.10, for both the autonomous and non-autonomous case. As can be seen, the model correctly predicts a super-critical bifurcation. However, the range of oil-whirl predicted, 57.1-57.2 Hz, is seemingly smaller than the observed. Nonetheless, the model correctly predicted that by increasing the radial clearance, the rotor would display a super-critical bifurcation. In addition, Table 6.2 lists the results measured against the ones predicted by the model.

6.2 Rotor with two disks

The dimensions of the rotor with two disks are shown in Fig. 6.11. The same parameters listed in Table 6.1 were considered for this system. The two disks have the same properties and are positioned at three different positions: position 1 (P1), position 2 (P2) and position 3 (P3). These are highlighted in the figure. The idea here is to analyze how the position of the disks affects the type of instability present in the real system. In addition, the bearing clearance was considered to be 90 μm. Similar to the previous case, a model reduction technique is applied to reduce the number of DOFs of the system. Here, the CB is used again, with the master nodes consisting of the bearings nodes (nodes

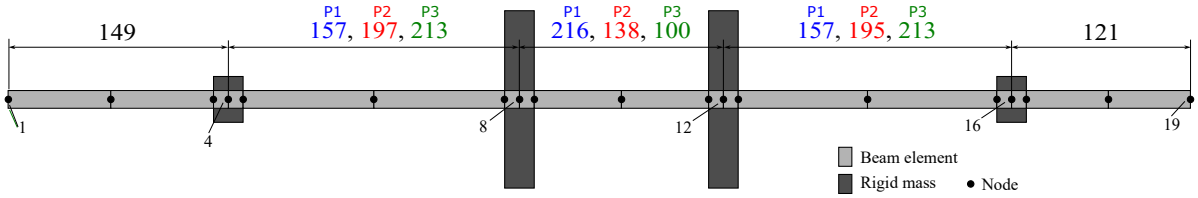

Figure 6.11: Finite element model of the rotor with two disks indicating the three positions considered (dimensions in mm).

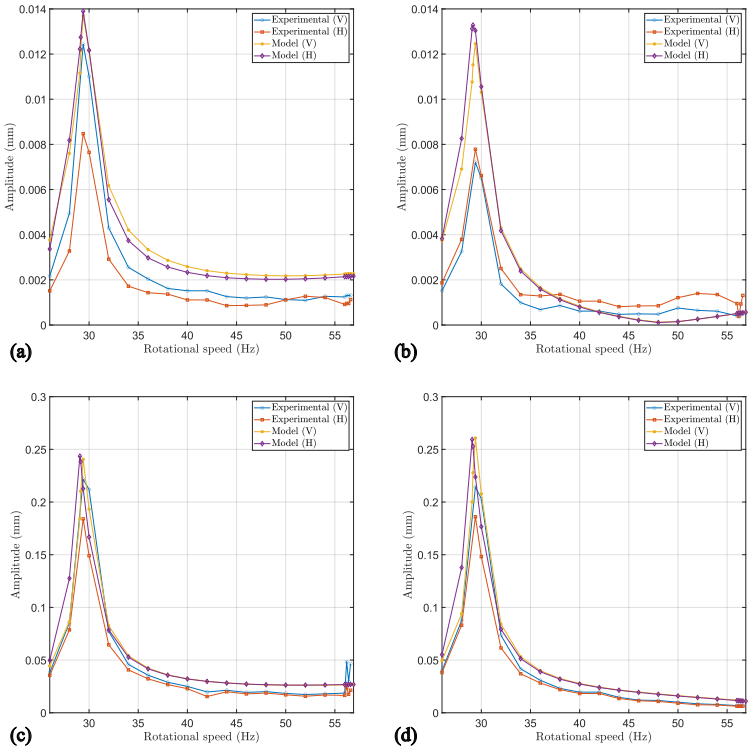

Figure 6.12: Comparison between measured and simulated 1× response with disks at P1: bearing 1 (a), bearing 2 (b), disk 1 (c) and disk 2 (d).

4 and 16). Lastly, a constant stiffness of 28 kN/m is placed at node 1 to mimic the effect of the flexible coupling. This value was obtained to match the model critical speed with the measured value.

Following the same approach as before, the first step is to compare the numerical and experimental synchronous responses. Figures 6.12-6.14 show such comparison. The experimental signals are obtained from the difference between the balanced and unbalanced (1 g mass at 50 mm at disk 2 only) rotors. The same value of unbalance is also used in the model for the evaluation.

The model showed good agreements in some cases, such as Figs. 6.12c-6.12d, and disagreements in others, such as Figs 6.12b, 6.13b and 6.14b. Note that the major differences occurred mainly in the measurements of bearing 2. Nonetheless, one may conclude that the model reasonably represents the real system.

The measured waterfall diagrams of the three positions are displayed in Figs. 6.15-6.16. Only the results of bearing 1 and disk 1 are shown for brevity. One may see the rise of the 0.5× component, indicating the occurrence of fluid instability. It is also noticeable the different strengths of this component for the different disk positions. This occurs because of the transient nature of the measurements when the rotor enters oil-whip, that is, in some cases the whip motion developed a bit further than in others. As mentioned

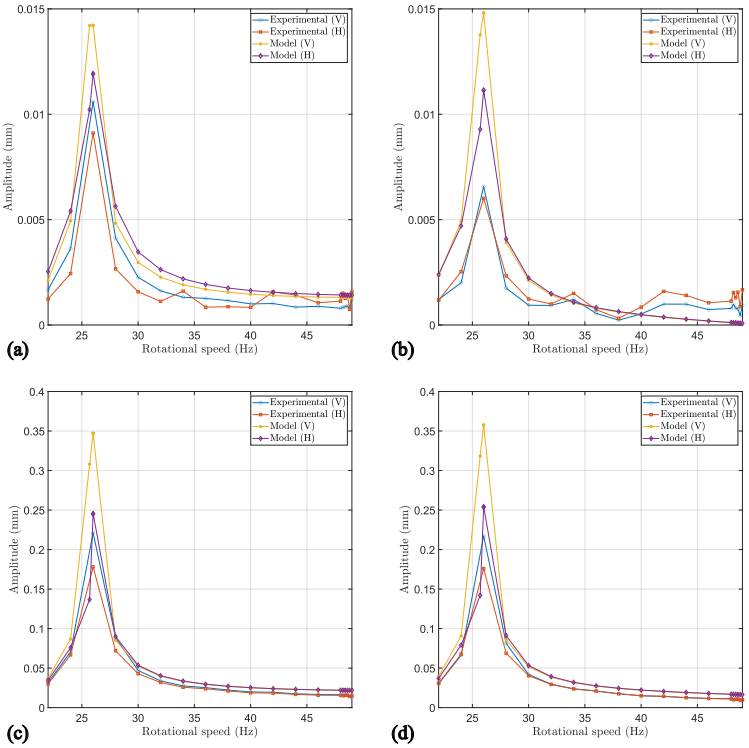

Figure 6.13: Comparison between measured and simulated 1× response with disks at P2: bearing 1 (a), bearing 2 (b), disk 1 (c) and disk 2 (d).

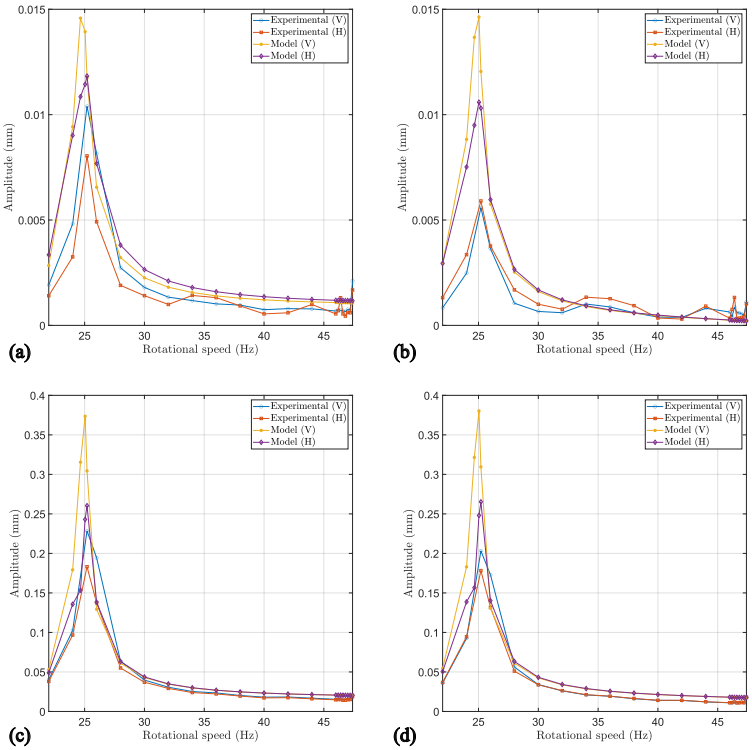

Figure 6.14: Comparison between measured and simulated 1× response with disks at P3: bearing 1 (a), bearing 2 (b), disk 1 (c) and disk 2 (d).

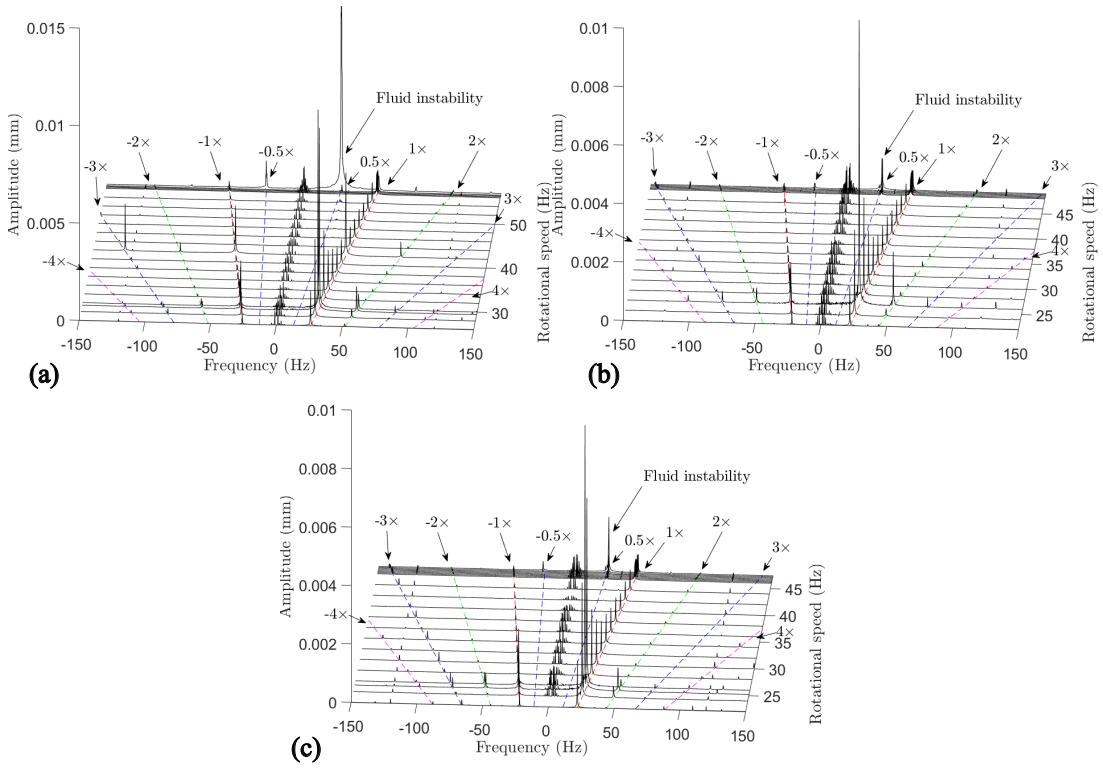

Figure 6.15: Measured waterfall diagrams with disks at positions: P1 (a), P2 (b) and P3 (c). Signals from bearing 1.

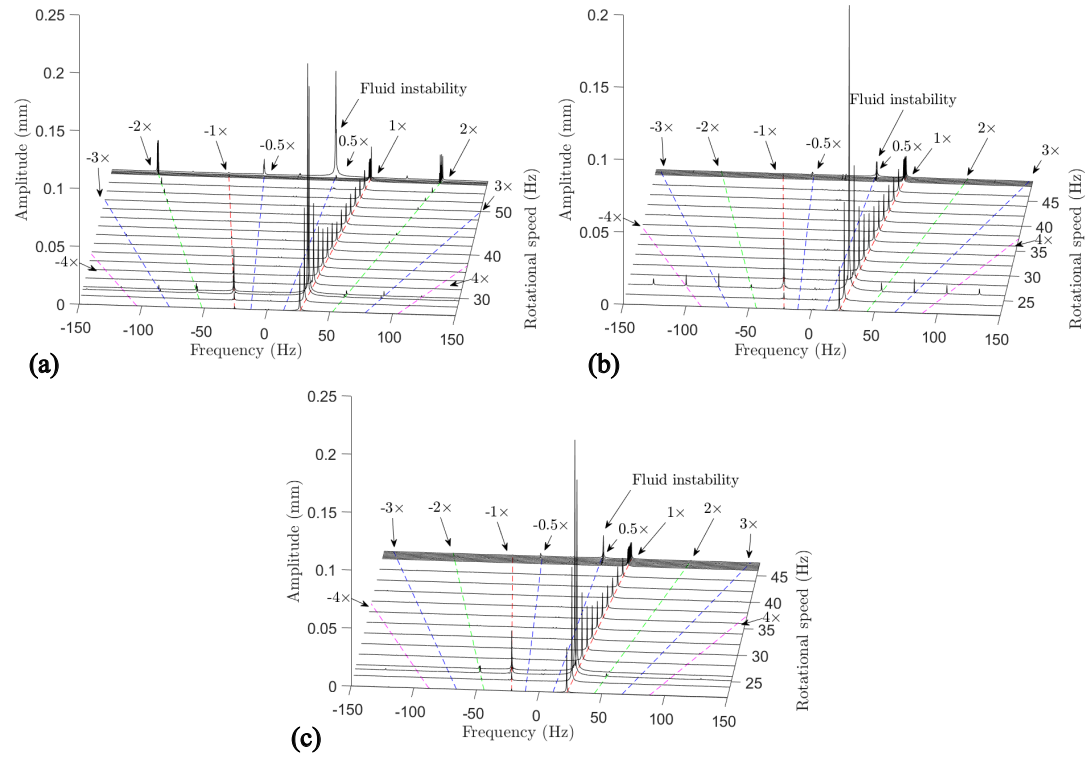

Figure 6.16: Measured waterfall diagrams with disks at positions: P1 (a), P2 (b) and P3 (c). Signals from disk 1.

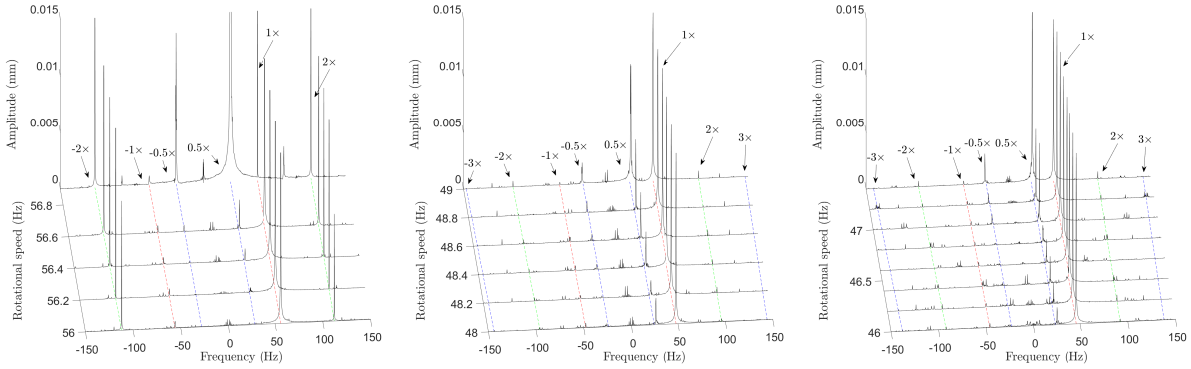

Figure 6.17: Expanded view of waterfall diagrams with disks at positions: P1 (a), P2 (b) and P3 (c). Signals from disk 1.

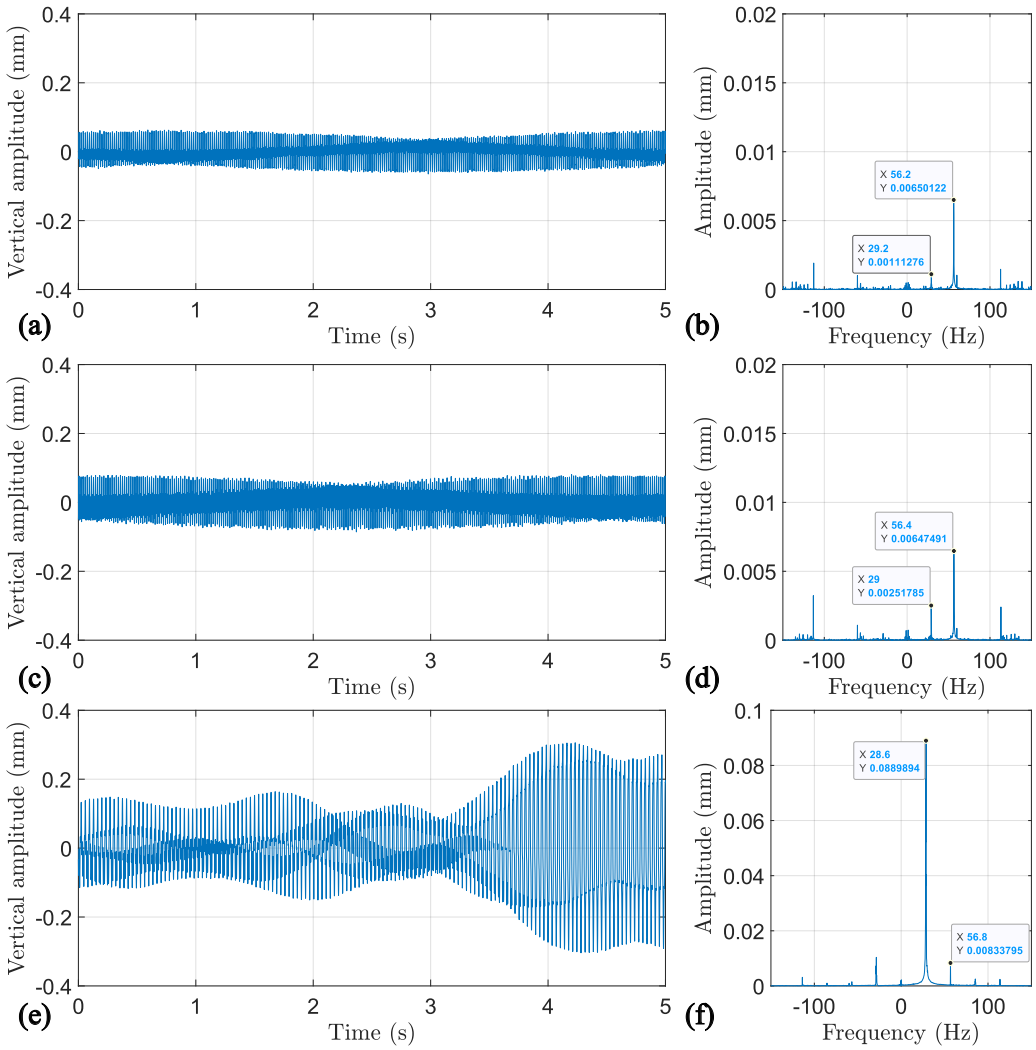

Figure 6.18: Measured time signals and frequency spectrum of disk 1 with disks at P1 during the transition to fluid instability at: 56.8 Hz (a-b), 56.4 Hz (c-d) and 56.2 Hz (e-f).

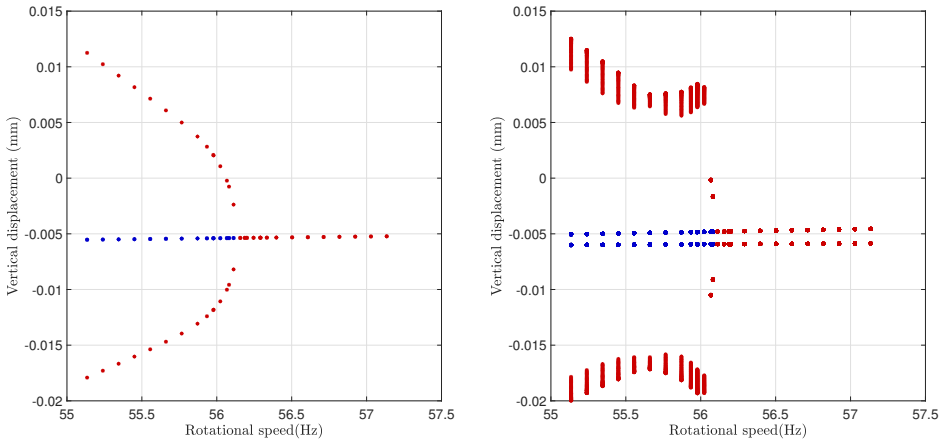

(a) (b)

Figure 6.19: CMR predictions for the rotor with disks at P1 near fluid instability: autonomous (a) and non-autonomous (b).

in the beginning of the chapter, no full whip motion was allowed due to safety concerns.

It is hard to say whether the rotor displayed oil-whirl prior to oil-whip from the results of Fig. 6.16. Figure 6.17 shows an expanded view of the waterfall diagrams. Here one may note that, as the disks are placed far apart at P1, the rotor tends to display oil-whip directly, as the 0.5× component is very low until oil-whip occurs. Conversely, as the disks are placed closed together at P3, the amplitude of the 0.5× component is noticeably higher, indicating oil-whirl prior to oil-whip, and hence, a super-critical bifurcation. The reason for this change in behavior is the effect of the disks on the onset speed of instability. The higher the onset speed is, the closer the rotor equilibrium will be to the center of the bearing, making the occurrence of oil-whip more likely (See Fig. 2.2 and discussion therein).

Figure 6.18 shows the transition to fluid instability when the disks are positioned at P1 (farther apart). The behavior is very similar to the rotor with one disk, Figure 6.4, where the bifurcation was sub-critical. However, a small 0.5× component still appeared in the frequency spectrum, indicating that the rotor entered a small oil-whirl prior to oil-whip. It is worth noting that this warning was very sudden, as one observes when comparing Figs. 6.17a with 6.17b or 6.17c. Thus, the rotor was very close to display oil-whip only.

The predictions of the CMR are shown in Fig. 6.19 for both autonomous and non-autonomous case. As one may note, the CMR predicted a sub-critical bifurcation, that is, oil-whip directly. Although the prediction did not match exactly the measured response, it still serves as a warning that with disks at P1, oil-whirl may not appear before oil-whip. Also, the response shown in Figure 6.18 is very close to being a sub-critical bifurcation,

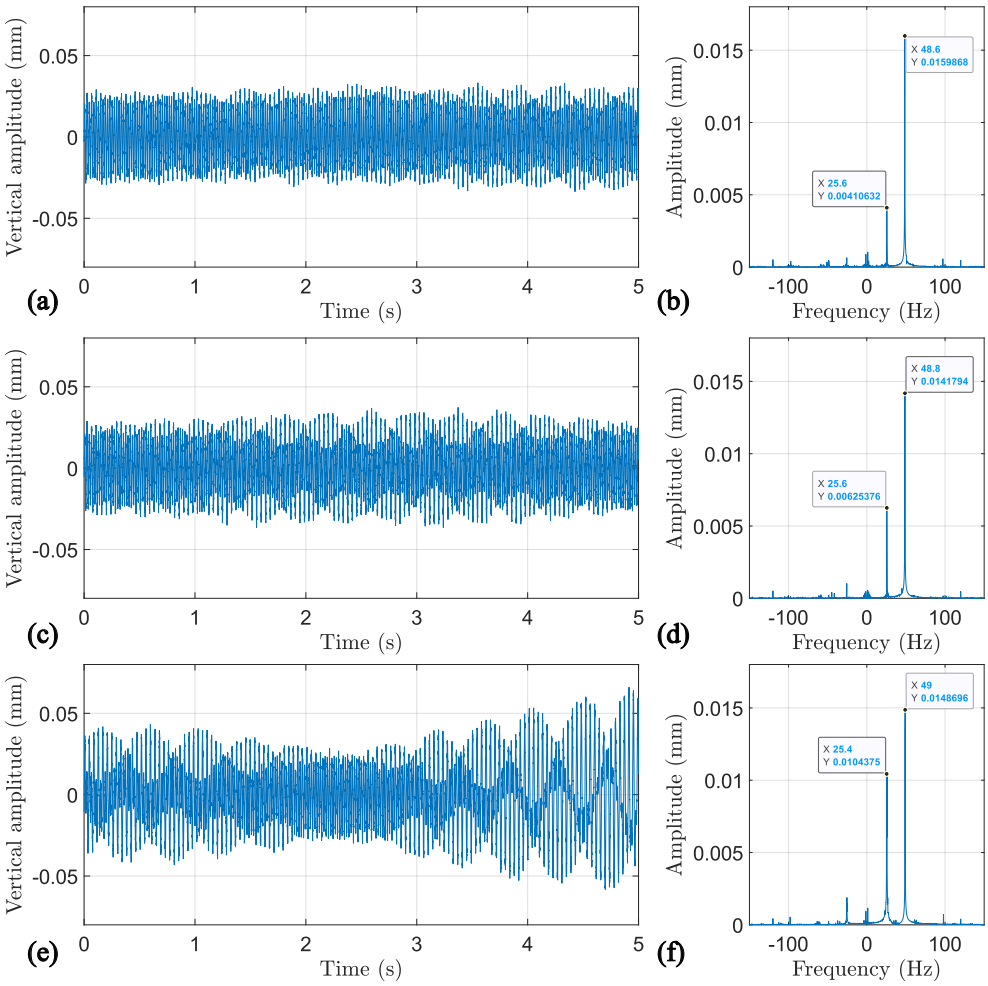

Figure 6.20: Measured time signals and frequency spectrum of disk 1 with disks at P2 during the transition to fluid instability at: 48.6 Hz (a-b), 48.8 Hz (c-d) and 49 Hz (e-f).

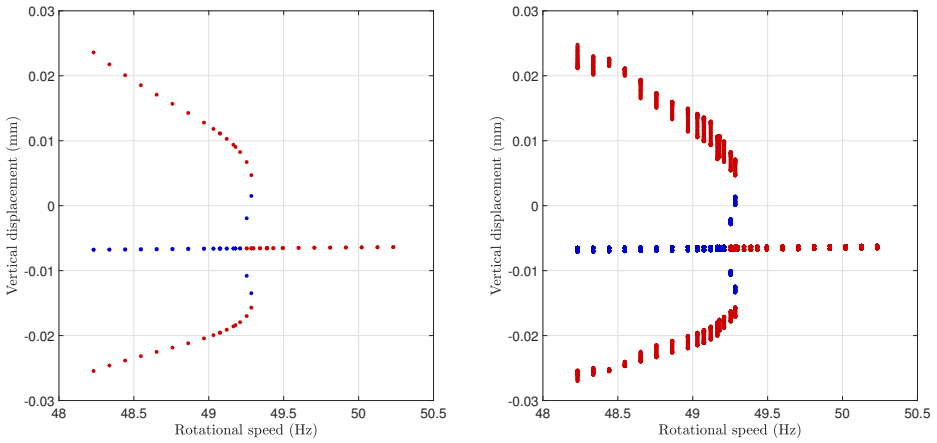

Figure 6.21: CMR predictions for the rotor with disks at P2 near fluid instability: autonomous (a) and non-autonomous (b).

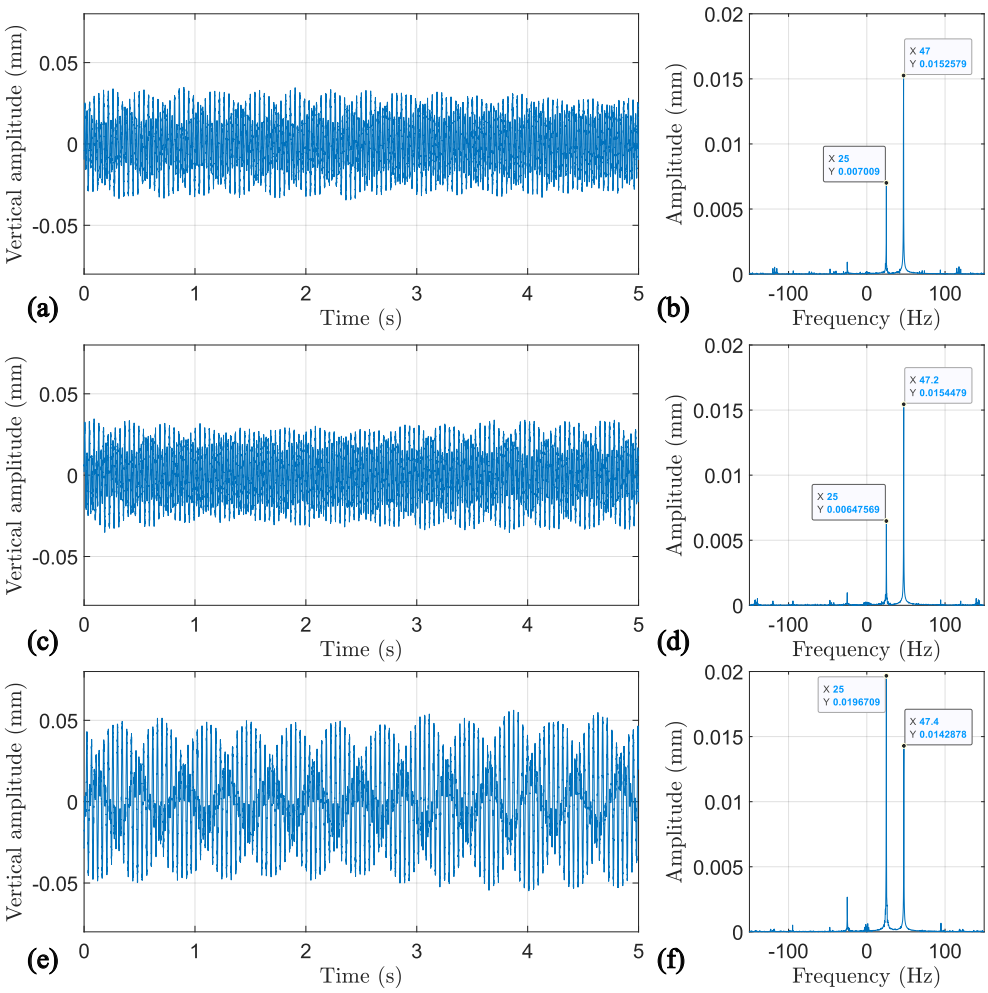

Figure 6.22: Measured time signals and frequency spectrum of disk 1 with disks at P3 during the transition to fluid instability at: 47 Hz (a-b), 47.2 Hz (c-d) and 47.4 Hz (e-f).

Table 6.3: Experimental frequencies against model (Rotor with two disks).

Case		Critical speed (Hz)	Instability speed (Hz)
Position 1	Experiment	29.4	56.2-56.6*
	Model	29.2	56.1
	Error (%)	0.68	0.18-0.8
Position 2	Experiment	26.0	48.6-49*
	Model	26.0	49.2
	Error (%)	0.01	1.23-0.41
Position 3	Experiment	25.2	47-47.4*
	Model	25.0	47.2
	Error (%)	0.79	0.38-0.46

*The speed is considered a range due to the difficulty in precisely defining it.

as the oil-whirl is very small.

The transition to fluid instability with disks at P2 is shown in Fig 6.20. Here, the 0.5× component is already very visible in the frequency spectrum and time series, indicating the appearance of oil-whirl. The predictions of the CMR are presented in Fig. 6.21,

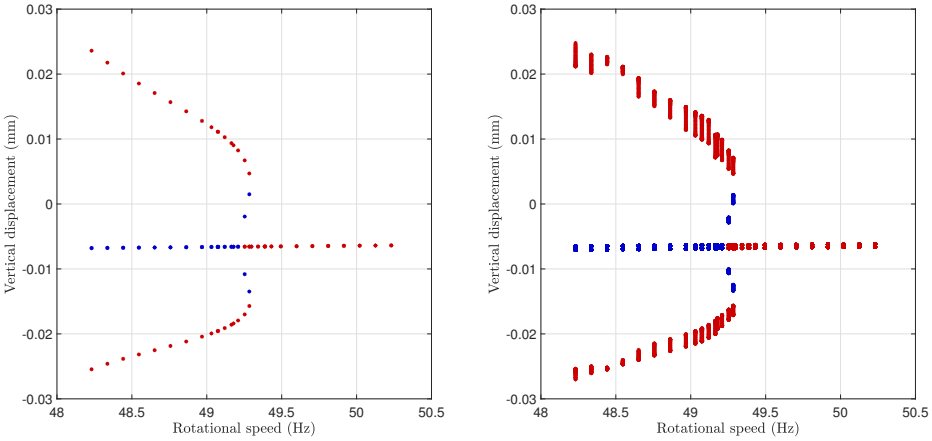

(a) (b)

Figure 6.23: CMR predictions for the rotor with disks at P3 near fluid instability: autonomous (a) and non-autonomous (b).

which showed that the system would present a super-critical bifurcation. Therefore, the prediction was in agreement with the observed response of the real system for this case.

The last result is shown in Fig. 6.22, where the disks were at P3 (farther apart). These results are very similar to the ones given by P2, with the difference that the oil-whirl is much more noticeable, indicating once more a super-critical bifurcation. The predictions of the CMR are shown in Fig. 6.23, and they are in agreement with the experimental results, as the model also presented a super-critical bifurcation. Table 6.3 lists the frequencies obtained by the model against the measured ones, indicating good agreement.

7 CONCLUSIONS

Journal or hydrodynamic bearings find common applications in several rotating machines mainly due to their many advantages such as simplicity in construction, ability to sustain high loads, and others. However, these types of bearings are known to display unwanted behavior, denoted as fluid-induced instability. For plain journal bearings, there are basically two types of instabilities, namely oil-whirl and oil-whip, the latter being more dangerous to the operation of the machine. One can also look at these phenomena as occurring due to a Hopf bifurcation, where the type of bifurcation tells whether oil-whirl or oil-whip will occur. This work presented an approach to predict the type of Hopf bifurcation that will manifest in a given system, which can be important information in the design of rotating machines.

The approach proposed is based on the Center Manifold Reduction (CMR) method, which estimates the center manifold of a nonlinear system, and allows one to find the limit cycles that emerge in Hopf bifurcations. The main contribution of this work lies in the use of the parameterization method for invariant manifolds (HARO et al., 2016) to estimate the center manifold, extending both the range in with the limit cycles can be obtained and their accuracy when compared with purely numerical approaches. Compared with previous applications of the CMR, e. g. Boyaci et al. (2009) or Kano et al. (2019), which were limited to around $\Delta\Omega = \pm 10$ rpm from the bifurcation point, the present method extents tenfold the range in which the limit cycles extending from Hopf bifurcations can be obtained (See for example Figs. 5.2).

In Chapter 5 the CMR was validated against numerical continuation, where the open-source numerical package MATCONT was used. Several parameters of the bearing were varied and the limit cycles were obtained. It was shown that the CMR is very accurate in the region close to the instability point, and starts to show greater errors the farther from said point. With the results, one can conclude that the CMR can be used reliably to detect the type of Hopf bifurcation, to perform parametric studies and to predict the amplitudes of the limit cycles. In addition, one major advantage of the CMR is its seamless application to high-dimensional rotor systems, which allows it to be used in the study and design of real rotating machines.

The CMR approach can also be used to study the effect of unbalance forcing in the fluid instability as presented in Section 5.2. Here the method was compared with transient numerical integration due to the inability of the numerical continuation software to handle quasi-periodic responses. Here the analytical nature of the CMR shows great advantages when compared with transient integration, which generally takes much longer and is only suited to the obtention of stable solutions. With the CMR, one is also able to study the effect of unbalance in the limit cycles of the autonomous system. Here, the onset speed

of instability and the type of bifurcation were shown to be dependent on the amount of unbalance present in the system.

Some experiments were also performed and were reported in Chapter 6. Two systems were studied: a rotor with one and two disks. The studies focused on changing some parameters of the system, namely the position of the disks and the radial clearance of the bearings, and assessing whether oil-whirl or oil-whip occurred. The experimental observations were in agreement with the numerical studies in which the higher the radial clearance, the higher the chance of the rotor displaying oil-whirl. With regard to the disks' positions, it was found that the closer together they are placed, the chance of oil-whirl also increases. In addition to this, the predictions of the CMR were also shown, where good agreements between the model and experiment were found, as one may note from Tables 6.2 and 6.3.

References

ALLEN, M. S. et al. *Substructuring in Engineering Dynamics: Emerging Numerical and Experimental Techniques*. Cham: Springer International Publishing, 2020. v. 594. (CISM International Centre for Mechanical Sciences, v. 594). ISBN 978-3-030-25531-2 978-3-030-25532-9.

AMAMOU, A. Nonlinear stability analysis and numerical continuation of bifurcations of a rotor supported by floating ring bearings. *Proceedings of the Institution of Mechanical Engineers, Part C: Journal of Mechanical Engineering Science*, IMECHE, v. 236, n. 5, p. 2172–2184, mar. 2022. ISSN 0954-4062.

ANASTASOPOULOS, L.; CHASALEVRIS, A. Bifurcations of Limit Cycles in Rotating Shafts Mounted on Partial Arc and Lemon Bore Journal Bearings in Elastic Pedestals. *Journal of Computational and Nonlinear Dynamics*, v. 17, n. 6, mar. 2022. ISSN 1555-1415.

ASTM D2270-10. *Practice for Calculating Viscosity Index from Kinematic Viscosity at 40 and 100C*. [S.l.]: ASTM International, 2016.

BOYACI, A. Numerical Continuation Applied to Nonlinear Rotor Dynamics. *Procedia IUTAM*, v. 19, p. 255–265, jan. 2016. ISSN 2210-9838.

BOYACI, A. et al. Analytical bifurcation analysis of a rotor supported by floating ring bearings. *Nonlinear Dynamics*, v. 57, n. 4, p. 497–507, set. 2009. ISSN 1573-269X.

CHASALEVRIS, A. Stability and Hopf bifurcations in rotor-bearing-foundation systems of turbines and generators. *Tribology International*, v. 145, p. 106154, maio 2020. ISSN 0301-679X.

CHAUVIN JR., D. *An Experimental Investigation of Whirl Instability Including Effects of Lubricant Temperature in Plain Circular Journal Bearings*. Tese (Master of Science in Mechanical Engineering) — Louisiana State University and Agricultural and Mechanical College, abr. 2003.

CHOUCHANE, M.; AMAMOU, A. Bifurcation of limit cycles in fluid film bearings. *International Journal of Non-Linear Mechanics*, v. 46, n. 9, p. 1258–1264, nov. 2011. ISSN 0020-7462.

CRAIG, R. R.; BAMPTON, M. C. C. Coupling of substructures for dynamic analyses. *AIAA Journal*, v. 6, n. 7, p. 1313–1319, jul. 1968. ISSN 0001-1452, 1533-385X.

de Castro, H. F.; CAVALCA, K. L.; NORDMANN, R. Whirl and whip instabilities in rotor-bearing system considering a nonlinear force model. *Journal of Sound and Vibration*, v. 317, n. 1-2, p. 273–293, out. 2008. ISSN 0022460X.

DEDINI, F. G. *Identificazione dei Cuscinetti e della Fondazione di Rotori: Metodologie e Risultati Sperimentali*. Tese (Doutorado) — Politecnico Di Milano, 1993.

DEEPAK, J. C.; NOAH, S. T. Experimental Verification of Subcritical Whirl Bifurcation of a Rotor Supported on a Fluid Film Bearing. *Journal of Tribology*, v. 120, n. 3, p. 605–609, jul. 1998. ISSN 0742-4787.

DHOOGE, A. et al. Cl_matcont: A continuation toolbox in Matlab. In: *Proceedings of the 2003 ACM Symposium on Applied Computing - SAC '03*. Melbourne, Florida: ACM Press, 2003. p. 161. ISBN 978-1-58113-624-1.

El-Shafei, A. et al. Some Experiments on Oil Whirl and Oil Whip. *Journal of Engineering for Gas Turbines and Power*, v. 129, n. 1, p. 144–153, mar. 2004. ISSN 0742-4795.

ELROD, H. G.; VIJAYARAGHAVAN, D. A Stability Analysis for Liquid-Lubricated Bearings Incorporating the Effects of Cavity Flow: Part I: Classical One-Dimensional Journal Bearing. *Journal of Tribology*, v. 116, n. 2, p. 330–335, abr. 1994. ISSN 0742-4787.

ELROD, H. G.; VIJAYARAGHAVAN, D. A Stability Analysis for Liquid-Lubricated Bearings Incorporating the Effects of Cavity Flow: Part II—Journal Bearing With Central Groove. *Journal of Tribology*, v. 117, n. 2, p. 365–367, abr. 1995. ISSN 0742-4787.

FAN, C.-C. et al. Study of start-up vibration response for oil whirl, oil whip and dry whip. *Mechanical Systems and Signal Processing*, v. 25, n. 8, p. 3102–3115, nov. 2011. ISSN 0888-3270.

FRISWELL, M. I. et al. *Dynamics of Rotating Machines*. New York: Cambridge University Press, 2010.

GUO, Z.; KIRK, R. G. Instability Boundary for Rotor-Hydrodynamic Bearing Systems, Part 1: Jeffcott Rotor With External Damping. *Journal of Vibration and Acoustics*, v. 125, n. 4, p. 417–422, out. 2003. ISSN 1048-9002.

GUO, Z.; KIRK, R. G. Instability Boundary for Rotor-Hydrodynamic Bearing Systems, Part 2: Rotor With External Flexible Damped Support. *Journal of Vibration and Acoustics*, v. 125, n. 4, p. 423–426, out. 2003. ISSN 1048-9002.

HALLER, G.; PONSIOEN, S. Exact model reduction by a slow–fast decomposition of nonlinear mechanical systems. *Nonlinear Dynamics*, v. 90, n. 1, p. 617–647, out. 2017. ISSN 1573-269X.

HAMROCK, B. J.; SCHMID, S. R.; JACOBSON, B. O. *Fundamentals of Fluid Film Lubrication*. 0. ed. [S.l.]: CRC Press, 2004. ISBN 978-1-135-53776-0.

HARO, À. et al. *The Parameterization Method for Invariant Manifolds: From Rigorous Results to Effective Computations*. Cham: Springer International Publishing, 2016. v. 195. (Applied Mathematical Sciences, v. 195). ISBN 978-3-319-29660-9 978-3-319-29662-3.

HASSARD, B. D.; KAZARINOFF, N. D.; WAN, Y.-H. *Theory and Applications of Hopf Bifurcation*. Cambridge: [s.n.], 1981. (London Mathematical Society Lecture Note Series, 41). ISBN 978-0-521-23158-9.

HOLLIS, P.; TAYLOR, D. L. Hopf Bifurcation to Limit Cycles in Fluid Film Bearings. *Journal of Tribology*, v. 108, n. 2, p. 184–189, abr. 1986. ISSN 0742-4787.

HORI, Y. A Theory of Oil Whip. *Journal of Applied Mechanics*, v. 26, n. 2, p. 189–198, 1959. ISSN 0021-8936.

ISHIDA, Y.; YAMAMOTO, T. *Linear and Nonlinear Rotordynamics: A Modern Treatment with Applications*. 2nd enlarged and improved ed. ed. Weinheim: Wiley-VCH, 2012. ISBN 978-3-527-40942-6.

JAIN, S.; HALLER, G. How to compute invariant manifolds and their reduced dynamics in high-dimensional finite element models. *Nonlinear Dynamics*, v. 107, n. 2, p. 1417–1450, jan. 2022. ISSN 0924-090X, 1573-269X.

KANO, H.; ITO, M.; INOUE, T. Order reduction and bifurcation analysis of a flexible rotor system supported by a full circular journal bearing. *Nonlinear Dynamics*, v. 95, n. 4, p. 3275–3294, mar. 2019. ISSN 1573-269X.

KIMBALL, AL. Internal friction as a cause of shaft whirling. *The London, Edinburgh, and Dublin Philosophical Magazine and Journal of Science*, Taylor & Francis, v. 49, n. 292, p. 724–727, 1925. ISSN 1941-5982.

KRACK, M.; GROSS, J. *Harmonic Balance for Nonlinear Vibration Problems*. Cham: Springer International Publishing, 2019. (Mathematical Engineering). ISBN 978-3-030-14022-9 978-3-030-14023-6.

LEE, C. W. *Vibration Analysis of Rotors*. 1st. ed. Dordrecht, Netherlands: Springer Science & Business Media, 1993.

LI, K. et al. Identification of oil-film coefficients for a rotor-journal bearing system based on equivalent load reconstruction. *Tribology International*, v. 104, p. 285–293, dez. 2016. ISSN 0301-679X.

LIU, W.; NOVAK, M. Dynamic behaviour of turbine-generator-foundation systems. *Earthquake Engineering & Structural Dynamics*, v. 24, n. 3, p. 339–360, 1995. ISSN 1096-9845.

LUND, J. W. Review of the Concept of Dynamic Coefficients for Fluid Film Journal Bearings. *Journal of Tribology*, v. 109, n. 1, p. 37–41, jan. 1987. ISSN 0742-4787.

MACHADO, T. H.; ALVES, D. S.; CAVALCA, K. L. Discussion about nonlinear boundaries for hydrodynamic forces in journal bearing. *Nonlinear Dynamics*, Springer Netherlands, v. 92, n. 4, p. 2005–2022, 2018. ISSN 1573269X.

MEIROVITCH, L. *Computational Methods in Structural Dynamics*. Rockville, USA: Sjithoff & Noordhoff International Publishers, 1980. v. 5.

MERELES, A.; ALVES, D. S.; CAVALCA, K. L. Continuous model applied to multi-disk and multi-bearing rotors. *Journal of Sound and Vibration*, v. 537, p. 117203, out. 2022. ISSN 0022-460X.

MERELES, A.; ALVES, D. S.; CAVALCA, K. L. Model reduction of rotor-foundation systems using the approximate invariant manifold method. *Nonlinear Dynamics*, mar. 2023. ISSN 1573-269X.

MERELES, A.; CAVALCA, K. L. Modeling of Multi-stepped Rotor-bearing Systems by the Continuous Segment Method. *Applied Mathematical Modelling*, v. 96, p. 402–430, 2021. ISSN 0307-904X.

MIRASKARI, M.; HEMMATI, F.; GADALA, M. S. Nonlinear Dynamics of Flexible Rotors Supported on Journal Bearings—Part I: Analytical Bearing Model. *Journal of Tribology*, v. 140, n. 2, out. 2017. ISSN 0742-4787.

MIRASKARI, M.; HEMMATI, F.; GADALA, M. S. Nonlinear Dynamics of Flexible Rotors Supported on Journal Bearings—Part II: Numerical Bearing Model. *Journal of Tribology*, v. 140, n. 2, out. 2017. ISSN 0742-4787.

MIURA, T.; INOUE, T.; KANO, H. Nonlinear Analysis of Bifurcation Phenomenon for a Simple Flexible Rotor System Supported by a Full-Circular Journal Bearing. *Journal of Vibration and Acoustics*, v. 139, n. 3, abr. 2017. ISSN 1048-9002.

MUSZYNSKA, A. Whirl and whip—Rotor/bearing stability problems. *Journal of Sound and Vibration*, v. 110, n. 3, p. 443–462, nov. 1986. ISSN 0022-460X.

MUSZYNSKA, A. Stability of whirl and whip in rotor/bearing systems. *Journal of Sound and Vibration*, v. 127, n. 1, p. 49–64, nov. 1988. ISSN 0022-460X.

MUSZYNSKA, A. *Rotordynamics*. Boca Raton: Taylor & Francis, 2005. ISBN 978-1-4200-2779-2.

MYERS, C. J. Bifurcation Theory Applied to Oil Whirl in Plain Cylindrical Journal Bearings. *Journal of Applied Mechanics*, v. 51, n. 2, p. 244–250, jun. 1984. ISSN 0021-8936.

NAYFEH, A. H.; BALACHANDRAN, B. *Applied Nonlinear Dynamics: Analytical, Computational, and Experimental Methods*. New York: Wiley, 1995. (Wiley Series in Nonlinear Science). ISBN 978-0-471-59348-5.

NEWKIRK, B. L. Varieties of Shaft Disturbances Due to Fluid Films in Journal Bearings. *Transactions of the American Society of Mechanical Engineers*, v. 78, n. 5, p. 985–987, 1956. ISSN 0097-6822.

NEWKIRK, B. L.; LEWIS, J. F. Oil-Film Whirl—An Investigation of Disturbances Due to Oil Films in Journal Bearings. *Transactions of the American Society of Mechanical Engineers*, v. 78, n. 1, p. 21–26, 1956. ISSN 0097-6822.

NEWKIRK, BL. Shaft whipping. *General Electric Review*, v. 27, p. 169, 1924.

NEWKIRK, BL.; TAYLOR, HD. Shaft whipping due to oil action in journal bearings. *General Electric Review*, v. 28, n. 8, 1925.

NONATO, F. *Modelo dinâmico para mancais de elementos rolantes radiais de esferas considerando os efeitos da lubrificação elastohidrodinâmica*. Tese (Doutor em Engenharia Mecânica) — Universidade Estadual de Campinas, Campinas, jul. 2013.

OPRENI, A. et al. Model order reduction based on direct normal form: Application to large finite element MEMS structures featuring internal resonance. *Nonlinear Dynamics*, v. 105, n. 2, p. 1237–1272, jul. 2021. ISSN 1573-269X.

OPRENI, A. et al. High-order direct parametrisation of invariant manifolds for model order reduction of finite element structures: Application to generic forcing terms and parametrically excited systems. *Nonlinear Dynamics*, v. 111, n. 6, p. 5401–5447, mar. 2023. ISSN 1573-269X.

PINKUS, O. Experimental Investigation of Resonant Whip. *Transactions of the American Society of Mechanical Engineers*, v. 78, n. 5, p. 975–983, 1956. ISSN 0097-6822.

PONSIOEN, S.; JAIN, S.; HALLER, G. Model reduction to spectral submanifolds and forced-response calculation in high-dimensional mechanical systems. *Journal of Sound and Vibration*, v. 488, p. 115640, dez. 2020. ISSN 0022460X.

PONSIOEN, S.; PEDERGNANA, T.; HALLER, G. Automated computation of autonomous spectral submanifolds for nonlinear modal analysis. *Journal of Sound and Vibration*, v. 420, p. 269–295, abr. 2018. ISSN 0022-460X.

PORITSKY, H. Contribution to the Theory of Oil Whip. *Transactions of the American Society of Mechanical Engineers*, v. 75, n. 6, p. 1153–1158, 1953. ISSN 0097-6822.

RENDL, J. et al. Subcritical behaviour of short cylindrical journal bearings under periodic excitation. *Nonlinear Dynamics*, mar. 2023. ISSN 1573-269X.

RENSON, L.; KERSCHEN, G.; COCHELIN, B. Numerical computation of nonlinear normal modes in mechanical engineering. *Journal of Sound and Vibration*, v. 364, p. 177–206, mar. 2016. ISSN 0022-460X.

ROBERTSON, D. Whirling of a journal in a sleeve bearing. *The London, Edinburgh, and Dublin Philosophical Magazine and Journal of Science*, Taylor & Francis, v. 15, n. 96, p. 113–130, 1933. ISSN 1941-5982.

SAFIZADEH, M. S.; GOLMOHAMMADI, A. Prediction of oil whirl initiation in journal bearings using multi-sensors data fusion. *Measurement*, v. 151, p. 107241, fev. 2020. ISSN 0263-2241.

SHAW, J.; SHAW, S. W. The effects of unbalance on oil whirl. *Nonlinear Dynamics*, v. 1, n. 4, p. 293–311, jul. 1990. ISSN 1573-269X.

SHAW, S.; PIERRE, C. Normal Modes for Non-Linear Vibratory Systems. *Journal of Sound and Vibration*, v. 164, n. 1, p. 85–124, jun. 1993. ISSN 0022460X.

SMITH, D. M. The motion of a rotor carried by a flexible shaft in flexible bearings. *Proceedings of the Royal Society of London. Series A*, The Royal Society London, v. 142, n. 846, p. 92–118, 1933. ISSN 0950-1207.

SOMEYA, T. (Ed.). *Journal-Bearing Databook*. Berlin, Heidelberg: Springer Berlin Heidelberg, 1989. ISBN 978-3-642-52511-7 978-3-642-52509-4.

SORGE, F. Rotor whirl damping by dry friction suspension systems. *Meccanica*, v. 43, n. 6, p. 577–589, dez. 2008. ISSN 1572-9648.

STROGATZ, S. H. *Nonlinear Dynamics and Chaos*. 0. ed. [S.l.]: CRC Press, 2018. ISBN 978-0-429-96111-3.

SZERI, A. Z. *Fluid Film Lubrication: Theory and Design*. Cambridge: Cambridge University Press, 1998. ISBN 978-0-521-61945-5.

TIEU, A. K.; QIU, Z. L. Identification of sixteen dynamic coefficients of two journal bearings from experimental unbalance responses. *Wear*, v. 177, n. 1, p. 63–69, set. 1994. ISSN 0043-1648.

TIWARI, R.; CHAKRAVARTHY, V. Simultaneous estimation of the residual unbalance and bearing dynamic parameters from the experimental data in a rotor-bearing system. *Mechanism and Machine Theory*, v. 44, n. 4, p. 792–812, abr. 2009. ISSN 0094-114X.

TONNESEN, J.; LUND, J. W. Some Experiments on Instability of Rotors Supported in Fluid-Film Bearings. *Journal of Mechanical Design*, v. 100, n. 1, p. 147–155, jan. 1978. ISSN 0161-8458.

TOUZÉ, C.; VIZZACCARO, A.; THOMAS, O. Model order reduction methods for geometrically nonlinear structures: A review of nonlinear techniques. *Nonlinear Dynamics*, v. 105, n. 2, p. 1141–1190, jul. 2021. ISSN 0924-090X, 1573-269X.

TROGER, H.; STEINDL, A. *Nonlinear Stability and Bifurcation Theory*. Vienna: Springer Vienna, 1991. ISBN 978-3-211-82292-0 978-3-7091-9168-2.

VANCE, J. M.; MURPHY, B.; ZEIDAN, F. *Machinery Vibration and Rotordynamics*. Hoboken, N.J: Wiley, 2010. ISBN 978-0-471-46213-2.

VERSTEEG, H. K.; MALALASEKERA, W. *An Introduction to Computational Fluid Dynamics: The Finite Volume Method*. Essex: Longman scientific and technical, 1995. ISBN 978-0-582-21884-0.

VIZZACCARO, A. et al. High order direct parametrisation of invariant manifolds for model order reduction of finite element structures: Application to large amplitude vibrations and uncovering of a folding point. *Nonlinear Dynamics*, v. 110, n. 1, p. 525–571, set. 2022. ISSN 1573-269X.

WAGG, David. J. Normal form transformations for structural dynamics: An introduction for linear and nonlinear systems. *Journal of Structural Dynamics*, 2022. ISSN 2684-6500.

WAGNER, M. B. et al. Model reduction methods for rotor dynamic analysis: A survey and review. *International Journal of Rotating Machinery*, Hindawi, v. 2010, 2010.

WANG, J. K.; KHONSARI, M. M. Prediction of the Stability Envelope of Rotor-Bearing System. *Journal of Vibration and Acoustics*, v. 128, n. 2, p. 197–202, jun. 2005. ISSN 1048-9002.

WANG, J. K.; KHONSARI, M. M. Application of Hopf bifurcation theory to rotor-bearing systems with consideration of turbulent effects. *Tribology International*, v. 39, n. 7, p. 701–714, jul. 2006. ISSN 0301-679X.

WANG, J. K.; KHONSARI, M. M. Bifurcation Analysis of a Flexible Rotor Supported by Two Fluid-Film Journal Bearings. *Journal of Tribology*, v. 128, n. 3, p. 594–603, mar. 2006. ISSN 0742-4787.

WIGGINS, S. *Introduction to Applied Nonlinear Dynamical Systems and Chaos*. New York: Springer-Verlag, 2003. v. 2. (Texts in Applied Mathematics, v. 2). ISBN 978-0-387-00177-7.

ZHANG, Y. Y.; XIE, Y. B.; QIU, D. M. Identification of linearized oil-film coefficients in a flexible rotor-bearing system, part I: Model and simulation. *Journal of Sound and Vibration*, v. 152, n. 3, p. 531–547, fev. 1992. ISSN 0022-460X.

ZHANG, Y. Y.; XIE, Y. B.; QIU, D. M. Identification of linearized oil-film coefficients in a flexible rotor-bearing system, part II: Experiment. *Journal of Sound and Vibration*, v. 152, n. 3, p. 549–559, fev. 1992. ISSN 0022-460X.